

ISSN 1451 - 9372 (Print)
ISSN 2217 - 7434 (Online)
JULY-SEPTEMBER 2023
Vol.29, Number 3, 169-252

Chemical Industry & Chemical Engineering Quarterly



The AChE Journal for Chemical Engineering,
Biochemical Engineering, Chemical Technology,
New Materials, Renewable Energy and Chemistry
www.ache.org.rs/ciceq



Journal of the
Association of Chemical Engineers of
Serbia, Belgrade, Serbia

**Chemical Industry &
Chemical Engineering
CI&CE Quarterly**

EDITOR-IN-CHIEF

Vlada B. Veljković

*Faculty of Technology, University of Niš, Leskovac, Serbia
E-mail: veljkovicvb@yahoo.com*

ASSOCIATE EDITORS

Jonjaua Ranogajec

*Faculty of Technology, University of
Novi Sad, Novi Sad, Serbia*

Srdan Pejanović

*Department of Chemical Engineering,
Faculty of Technology and Metallurgy,
University of Belgrade, Belgrade, Serbia*

Milan Jakšić

*ICEHT/FORTH, University of Patras,
Patras, Greece*

EDITORIAL BOARD (Serbia)

Dorđe Janačković, Sanja Podunavac-Kuzmanović, Viktor Nedović, Sandra Konstantinović, Ivanka Popović, Siniša Dodić, Zoran Todorović, Olivera Stamenković, Marija Tasić, Jelena Avramović, Goran Nikolić, Dunja Sokolović

ADVISORY BOARD (International)

Dragomir Bukur

Texas A&M University,

College Station, TX, USA

Milorad Dudukovic

*Washington University,
St. Luis, MO, USA*

Jiri Hanika

*Institute of Chemical Process Fundamentals, Academy of Sciences
of the Czech Republic, Prague, Czech Republic*

Maria Jose Cocero

*University of Valladolid,
Valladolid, Spain*

Tajalli Keshavarz

*University of Westminster,
London, UK*

Zeljko Knez

*University of Maribor,
Maribor, Slovenia*

Igor Lacik

*Polymer Institute of the Slovak Academy of Sciences,
Bratislava, Slovakia*

Denis Poncelet

ENITIAA, Nantes, France

Ljubisa Radovic

Pen State University,

PA, USA

Peter Raspor

*University of Ljubljana,
Ljubljana, Slovenia*

Constantinos Vayenas

*University of Patras,
Patras, Greece*

Xenophon Verykios

*University of Patras,
Patras, Greece*

Ronnie Willaert

*Vrije Universiteit,
Brussel, Belgium*

Gordana Vunjak Novakovic

*Columbia University,
New York, USA*

Dimitrios P. Tassios

*National Technical University of Athens,
Athens, Greece*

Hui Liu

China University of Geosciences, Wuhan, China

FORMER EDITOR (2005-2007)

Professor Dejan Skala

University of Belgrade, Faculty of Technology and Metallurgy, Belgrade, Serbia



Journal of the
Association of Chemical Engineers of
Serbia, Belgrade, Serbia

**Chemical Industry &
Chemical Engineering
CI&CE Quarterly**

Vol. 29

Belgrade, July-September 2023

No. 3

Chemical Industry & Chemical Engineering
Quarterly (ISSN 1451-9372) is published
quarterly by the Association of Chemical
Engineers of Serbia, Kneza Miloša 9/1,
11000 Belgrade, Serbia

Editor:
Vlada B. Veljković
veljkovic@yahoo.com

Editorial Office:
Kneza Miloša 9/1, 11000 Belgrade, Serbia
Phone/Fax: +381 (0)11 3240 018
E-mail: shi@ache.org.rs
www.ache.org.rs

For publisher:
Ivana T. Drvenica

Secretary of the Editorial Office:
Slavica Desnica

Marketing and advertising:
AChE Marketing Office
Kneza Miloša 9/1, 11000 Belgrade, Serbia
Phone/Fax: +381 (0)11 3240 018

Publication of this Journal is supported by the
Ministry of Education, Science and
Technological Development of the Republic of
Serbia

Subscription and advertisements make payable
to the account of the Association of Chemical
Engineers of Serbia, Belgrade, No. 205-2172-
71, Komercijalna banka a.d., Beograd

Computer typeface and paging:
Marija B. Tasić

Journal manager:
Aleksandar B. Dekanski

Printed by:
Faculty of Technology and Metallurgy,
Research and Development Centre of Printing
Technology, Karnegijeva 4, P.O. Box 3503,
11120 Belgrade, Serbia

Abstracting/Indexing:
Articles published in this Journal are indexed in
Thompson Reuters products: *Science Citation
Index - Expanded*TM - access via *Web of
Science*[®], part of *ISI Web of Knowledge*SM

CONTENTS

- Pavel Shcherban, Alexander Gapchich, Aleksey Zhdanov, Olga Letunovskaya, **Optimization of excess brines disposal methods at potash mining and processing plants** 169
- Nataša Milićević, Marijana Sakač, Bojana Šarić, Dubravka Škrobot, Bojana Filipčev, Olivera Šimurina, Pavle Jovanov, Mladenka Pestorić, Aleksandar Marić, **Soybean bran as the fat replacer in gluten-free cookie formulation: physicochemical properties and sensory profiles** 179
- Amarílís Severino E Souza, Thiago César De Souza Pinto, Alfredo Moisés Sarkis, Thiago Faggion De Pádua, Rodrigo Béttega, **Energy analysis of the convective drying of iron ore fines** . 189
- Venugopal Palaniswamy, Kaliappan Seeniappan, Thanigaivelan Rajasekaran, Natrayan Lakshmaiya, **Enhancing MRR and accuracy with magnetized graphite tool in electrochemical micromachining of copper**201
- Lucas Oliveira Cardoso, Bruno Santos Conceição, Márcio Luis Lyra Paredes, Silvana Mattedi, **Thermodynamic modeling of gas solubility in ionic liquids using equations of state**209
- Periasamy Manikandan Srinivasan, Nesakumar Dharmakkan, Maha Devaa Sri Vishnu, Hari Prasath, Ramaraj Gokul, Ganeshan Thiyagarajan, Govindasamy Sivasubramani, Balachandran Moulidharan, **Heat transfer studies in a plate heat exchanger using Fe₂O₃-water-engine oil nanofluid**.....225
- Selma Kayacan-Cakmakoglu, Ilker Atik, Perihan Kubra Akman, Ibrahim Doymaz, Osman Sagdic, Salih Karasu, **Effect of the different infrared levels on some properties of sage leaves**235
- Alanna Silveira De Moraes, Gabriela Oliveira Castro Poncinelli, Aron Seixas Terra Rodrigues, Laise Fazol Do Couto, Silvia Luciana Fávaro, Rita De Cássia Colman, **Study of catalytic oxidation of toluene using Cu-Mn, Co-Mn, and Ni-Mn mixed oxides catalysts**243

**The activities of the Association of Chemical Engineers of Serbia
are supported by:**



**MINISTRY OF SCIENCE,
TECHNOLOGICAL DEVELOPMENT
AND INNOVATION
OF REPUBLIC OF SERBIA**



Faculty of Technology and
Metallurgy, University of Belgrade



Faculty of Science, University of Novi Sad



Institute for Technology of Nuclear
and Other Mineral Raw Materials,
Belgrade



Faculty of Technology,
University of Novi Sad



Institute of Chemistry, Technology and Metallurgy,
University of Belgrade



Faculty of Technical Sciences
University of Novi Sad



Faculty of Technology,
University of Niš, Leskovac



Faculty of Technical Sciences,
University of Priština, Kosovska Mitrovica



IMS Institute, Belgrade



DCP HEMIGAL
Leskovac



Elixir Prahovo

PAVEL SHCHERBAN¹
ALEXANDER GAPCHICH²
ALEKSEY ZHDANOV³
OLGA LETUNOVSKAYA⁴

¹I. Kant BFU, Engineering and
Technical Institute, Kaliningrad,
Russia

²ICEMR RAS, Institute of
Comprehensive Exploitation of
Mineral Resources Russian
Academy of Sciences, Moscow,
Russia

³RSGU named after Sergo
Ordzhonikidze, Moscow, Russia

⁴Saint Petersburg Mining
University, St. Petersburg,
Russia

SCIENTIFIC PAPER

UDC 622:66:54

OPTIMIZATION OF EXCESS BRINES DISPOSAL METHODS AT POTASH MINING AND PROCESSING PLANTS

Article Highlights

- Problem of optimization of potash ores processing
- Preparation and utilization of excess brines
- Backfilling of excess brines, implementation of technology
- Combining different utilization technologies
- Economic and organizational aspects of excess brine utilization

Abstract

The paper analyzes the positive and negative aspects of various technological solutions for the liquid brines used during the development of polymineral potash ore deposits and considers the problem of determining the choice of the optimal approach by considering geological, technical, environmental, and financial factors. The study of the issues of utilization and reduction of the liquid brines components of discharges in the production of potash fertilizers, the simultaneous reduction of valuable components loss with liquid discharges, and, due to this, increasing the production of potash fertilizers, and the usage in the technology of mine brines, are an urgent and important scientific and engineering challenge of the potash industry. Technologically, several alternative solutions can reduce the number of liquid by-products placed in sludge storage. The work used analytical methods, including statistical data processing, modeling, pre-design studies of technological solutions, and assessment of economic costs. Excess brines of potash mining and processing plants are liquid waste obtained during the production of potash fertilizers - MOP и SOP. The accumulation of excess brines in sludge storage facilities is estimated at millions of cubic meters per year. However, the expansion of the sludge storage facilities area and the construction of dams are only temporary solutions. They are associated with risks in the design, construction, and operation of hydraulic structures, increasing the risks of brine leakage into open and underground water basins. Therefore, it makes it necessary to use other methods of brine disposal. Depending on the nature of the processed polymineral potash ores, several methods can be combined to dispose of excess brines at once: backfilling, osmosis, injection into deep horizons, and multistage evaporation. The most optimal combination of brine reduction technologies for potassium-magnesium processing plant's raw materials is the following: 60% is disposed of by usage of vacuum evaporation units, 20 % by injecting excessive brines into deep absorbing horizons, and 10%–20% should be used for backfilling or additional products production.

Keywords: backfilling, cogeneration, excess brines, potash ore processing, vacuum evaporation.

Among the main industrial methods of excess

brines disposal, the following can be distinguished: vacuum-evaporation of brines with subsequent salt, crystallization, injection into deep absorbing horizons (IIDA), backfilling of exhausted space in the mine (hydro-backfilling, hardening backfilling) [1]. Also, in some cases and technological processes, reverse osmosis and thermohydrolysis of bischofite liquor with the magnesium oxide and hydrochloric acid productions are. The content of the main technologies

Correspondence: P.Shcherban, Immanuel Kant Baltic Federal University, Engineering and Technical Institute, Kaliningrad, 57 Ozerova St.236006, Russia.

E-mail: ursa-maior@yandex.ru

Paper received: 28 December, 2021

Paper revised: 16 June, 2022

Paper accepted: 1 September, 2022

<https://doi.org/10.2298/CICEQ211228024S>

that solve potash production by-product placement will be briefly explained.

Thus, the excess brine evaporation is carried out in a multiple-effect evaporation system. Evaporators consist of a heating chamber, in the center of which there is a boiling pipe and a separator. This device separates the solution steam from the boiling solution [2]. The circulation of the evaporated solution through the heating chamber tubes is carried out using a pump; the heating steam enters the inter-tube space. The solution is heated in the heating chamber tubes to a temperature exceeding the boiling point; boiling the solution occurs in the boiling pipe above the heating chamber. The evaporated solution and the crystallizing solid phase are removed from the separator's lower part. Considering the accumulation of atmospheric precipitation and other production factors in brine storage facilities, the brines with a low-temperature depression make it technically possible to use vacuum evaporation units with a heat pump.

On the other hand, backfilling technology is a hydraulic transport or hardening mixture transport system of the processing plant wastes into the exhausted space of the mine. Thus, these by-products are placed in the exhausted spaces of the mine, reducing the areas alienated for placing these volumes on the surface and reducing the environmental load on the area near the production. Besides, in the case of the hardening backfilling mixture usage (i.e., material gaining the strength comparable to the surrounding mining mass), it's possible to increase the extraction of useful components without significantly disrupting the geomechanical stability of the overlying layers [3].

Excess brine pumping technologies are based on returning raw oil water and are currently a fairly well-developed method. The main requirements are the maximum compliance of the chemical water composition with the initial composition of the fluid. In addition, it is preferable to observe the temperature regime to prevent increased salt deposition on the equipment and in the bottom-hole zone of the well. As for potash plants, deciding on injection requires a fairly detailed, costly, and time-consuming study, which includes: the search for a suitable reservoir formation, the justification of the reservoir closure and its tightness, reservoir protection from tectonic and other geological factors, the study of the reservoir capacitance properties, investigation of pressure parameters, permeability and effective porosity of rocks, the material composition of the reservoir, its inertia in relation to the injected brines. Therefore, a mandatory stage is full-scale tests on pilot wells for 1.5 to 2 years (the analysis of seasonal change influence), which allows us to obtain specific parameters of the good pick-up rate and to perform calculations of the

injection complex. The minimum number of wells can be defined as - working, observation/backup, and monitoring [4].

An additional way of brine utilization is membrane technologies. Many foreign and domestic publications, both fundamental and applied, are devoted to describing membrane technologies [5], describing in detail the nuances of the membrane behavior in various processes.

The membrane is a porous partition having pores similar in size. During the filtration process, particles with sizes larger than the pore size are retained. In contrast, the filtrate (permeate) containing smaller particles, including solvent molecules, can pass through the pores [6].

According to this approach, the following division of membrane technologies has historically been established based on the size and nature of the separated impurities. Microfiltration detains particles larger than $0.1\ \mu\text{m}$ – $1\ \mu\text{m}$ (large colloids, suspensions, bacteria). The working pressure is usually up to 1 atm–2 atm. Ultrafiltration separates much smaller particles - in the range of $0.01\ \mu\text{m}$ – $0.1\ \mu\text{m}$, including colloids and large organic molecules that are retained (with a molecular weight of over 1000 Da). Nanofiltration effectively detains components of substances with a size of $0.001\ \mu\text{m}$ – $0.01\ \mu\text{m}$, an organic matter with a molecular weight starting from 500 Da. The working pressure of the process is from 3 atm to 20 atm. Nanofiltration removes chromaticity, organic matter, pesticides, hardness salts, and microbiological contamination. Reverse osmosis removes dissolved salts (filtration rating at $0.0001\ \mu\text{m}$ – $0.001\ \mu\text{m}$) and organic matter (with a molecular weight of less than 500 Da). The working pressure is up to 150 atm.

Despite the apparent simplicity of membrane processes, their practical use became possible only after developing the necessary materials, membrane manufacturing technologies, special pumps and valves, automation systems, etc.

All membranes for nanofiltration, reverse osmosis, and most micro- and ultrafiltration membranes are made of organic polymers. Porous membranes are used for micro- and ultrafiltration, and non-porous membranes are used for nanofiltration and reverse osmosis. The main advantage of polymer membranes is high processability and great possibilities for controlling the properties and structure of the membrane by small chemical and/or technological variations of the manufacturing process.

Achieving acceptable performance with low membrane permeability requires using elements with a high specific membrane area per unit volume of the apparatus. These can include semi-fiber and roll

elements (Fig. 1).

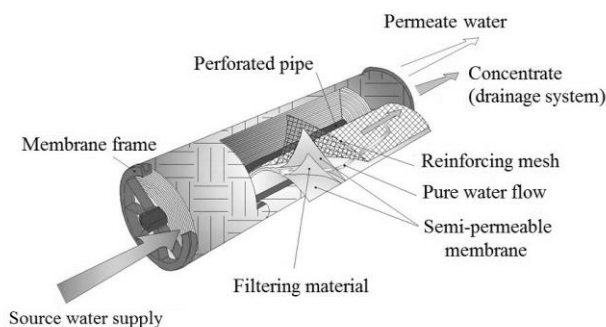


Figure 1. Structure of the nanofiltration roll element.

Special attention should be paid to the works of scientists [7], which describe promising technologies for the utilization of brines using a stimulating membrane [membrane-promoted crystallization (MPC)]. The resulting "needle-like" KCl crystals have a relatively small contact area with the membrane, which ensures easy removal of KCl from the membrane surface for its regeneration and further use. The MPC process demonstrates high KCl performance (up to 134.3 g/m²). The MPC process provides a new and promising approach to the sustainable production of KCl from KCl brine; thereby, in addition to the problem of brine utilization, the task of increasing the KCl extraction and reducing irretrievable losses of a valuable component with waste is solved, which determines the integrated use of mineral raw materials.

Nanofiltration and reverse osmosis membranes impose stricter requirements on the quality of the treated medium. Usually, a preliminary cleaning is required, which removes suspended particles, dissolved iron, aluminum, and manganese and neutralizes oxidants [7]. During operation, a large amount of dirt gradually accumulates on the surface and in the membrane's pores. This sediment reduces the productivity of the equipment. The equipment operation can be improved by conducting a membrane regeneration cycle. Despite the industrial type of such equipment, reverse osmosis has not found a wide practical application in potash plants.

Problems of technological process optimization

Next, we will analyze several materials on the excess brine disposal methods at enterprises that enrich potassium-magnesium ores for the effectiveness of their use in the disposal of excess brines. Recent studies show a particular prospect of modernization of flotation technology during ore enrichment (including polymineral ones) that reduces the concentration and volume of by-product brines remaining after production [8]. At the same time, along with the search for a new reagent that provides a more efficient flotation

process, the search for reducing the operating costs of evaporation equipment is continuing since this would also reduce the volume of excess brines obtained in the main technological process[9]. In industrial practice, there are two main energy recovery: multiple-effect evaporator systems and heating compressors [10,11].

Multiple Effect Evaporation (MEE). The energy balance of a single-step evaporation unit indicates that the heat content of the secondary steam is approximately equal to the heat supplied from the heating side of the heat exchanger. If the secondary steam under the action of the primary energy source (steam from the boiler facility) is used as a heating element in the second step of the unit, the energy consumption will be reduced by approximately 50%. The same principle can be used in subsequent steps and, thus, saves thermal energy. The maximum heating temperature at the first stage and the lowest boiling point at the last stage form a common temperature difference distributed across all the stages in the device. Accordingly, the temperature difference in each step decreases with an increased number of steps.

The minimum temperature difference between the multiple-effect evaporation unit is determined by the sum of the temperature difference required for effective heat transfer from the heating steam to the evaporated medium (6 °C–11 °C) and the temperature difference at the boiling point of the brine and the solvent (temperature depression). Due to the distribution of the total temperature difference between the boilers into several ones, it becomes necessary to increase the heating surface of each boiler to ensure the required performance for evaporated water at a smaller temperature difference. During the first approximation, it can be assumed that the area of the heat exchange surfaces in all boilers increases in proportion to the number of boilers. Consequently, the capital cost of the installation increases linearly, while the increase in energy efficiency during the transition to each subsequent boiler increases at a slower rate. The main advantage of MEE is the repeated use of the heat content of the primary heating steam. However, these units are characterized by significant disadvantages: high cost and significant dimensions of the units, which occupy a significant part of the industrial area (Fig. 2) [12].

Mechanical vapor recompression (MVR). Iterative use of the heat of the primary heating steam can be achieved in a single-stage unit at any desired boiling point of the solution by applying mechanical vapor recompression (MVR). The evaporation unit with MVR operates based on the principle of the Carnot cycle of a high-speed centrifugal compressor, in which the secondary steam is partially or wholly sucked in by a steam jet injector or a turbocharger and recompressed

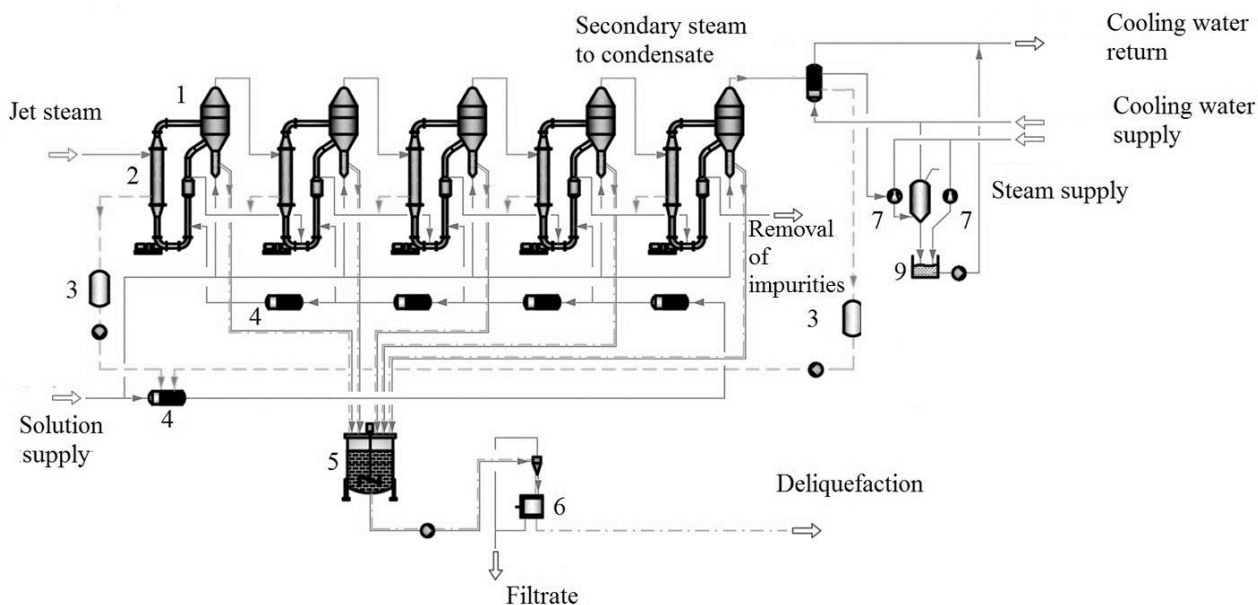


Figure 2. Multiple Effect Evaporation (MEE): 1 - Vacuum Crystallization Unit (VCU); 2 - Heat Exchanger unit; 3 - Process Condensate Tank ; 4 - Heater; 5 - Agitation Tank; 6 - Centrifuge; 7 - Steam ejector; 8 - Condenser; 9 - Hotwell.

to the level of a defined heating steam pressure. Then, this stream is used to heat the same unit. The energy of vaporization is generated due to an isentropic increase in the steam enthalpy. Secondary steam condensate is also used to heat brine to a preset incoming temperature. Due to such intensive heat

recovery, the consumption of additional heating steam is not required in most cases, except for steam ejectors in the final step (Fig.3) [13]. The steam consumption for steam ejectors is insignificant and amounts to (2–3) tons per hour.

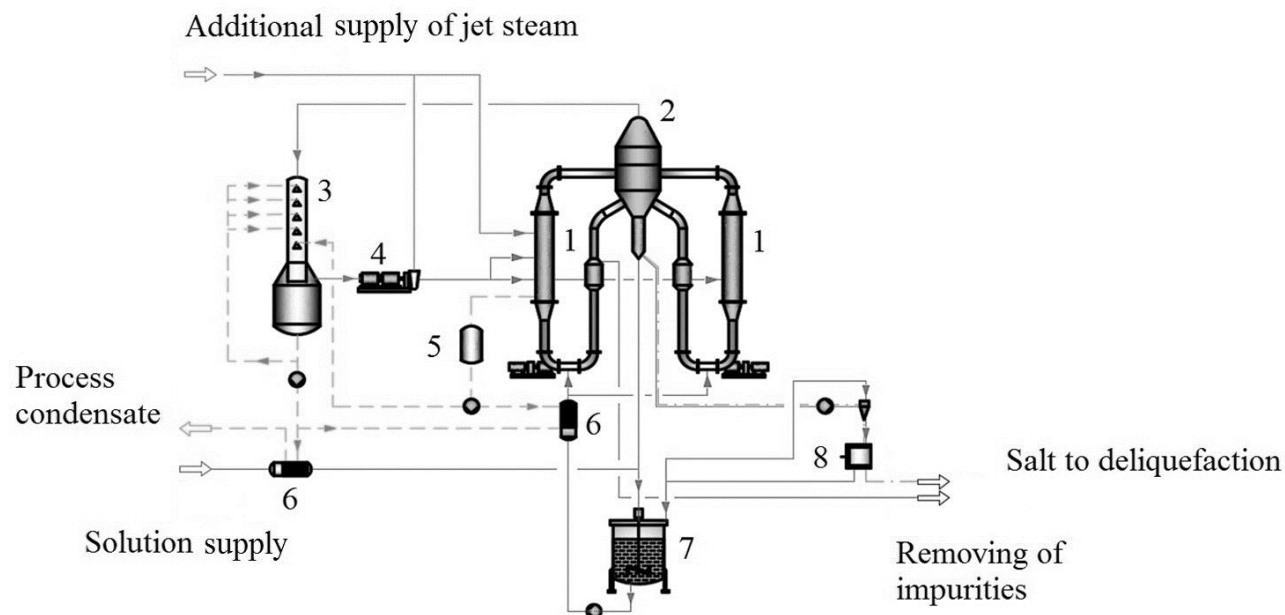


Figure 3. Mechanical Vapor Recompression: 1 - Heat Exchanger; 2 - Evaporative Crystallizer; 3 - Scrubber; 4 - Compressor; 5 - Condensate collector; 6 - Heater; 7 - Equalizing Tank; 8 - Centrifuge.

The advantage of MVR is the possibility of repeated use of secondary heating steam in a closed cycle, which allows evaporation to be carried out in a single-stage boiler, thereby reducing the metal

consumption of the equipment and operating costs. Nevertheless, the volume of investment in capital expenses during the installation of compresses increases by 20%–30%. In addition, the energy

consumption of the vacuum evaporation unit with MVR increases significantly.

Thus, one compressor has 4.2 MW–6.3 MW of installed capacity. The practice of Greenfield projects approves the number of investments for MVR capital expenditures that can be paid back within 5 years to 6 years, depending on electricity tariffs in a particular region [14]. Table 1 shows a comparative analysis of the energy consumption and MVR unit based on the calculation at the designed plant for the disposal of excess brines with a capacity of 1 million m³ per year, located in the Perm Region of the Russian Federation. Energy costs in this region are estimated at 0.016 US dollars per Giga calories for steam heating and 0.035 US dollar per kilowatt.

Table 1. Technical characteristics and cost of MEE and MVR for the disposal of 1 million cubic meters of brines per year.

OPEX	MEE	MVR
Heating steam consumption from the boiler room, t/h	230	11
Installation capacity, kW	3 500	27 100
Cooling water consumption, m ³ /h	6500	850
Specific cost of steam, rub/kg	0,6	0,6
Specific cost of electricity, rub/kWh	2,43	2,43
Working Time Fund, hours/year	8000	8000
Steam cost (per year), million rubles	1 104	53
The cost of electricity (per year), million rubles	64,04	526,82
Total, rub	1 172 040 000	579 620 000
Total, Euro	15 026 154	7 431 077

MVR saves the consumption of conventional fuel, which can be converted to natural gas or fuel oil, for generating heating steam about 20 times, which causes a significant reduction in greenhouse gas CO₂ emissions, thereby reducing the need for a quota for CO₂ emissions into the atmosphere. This factor is gaining relevance yearly, considering the agreement under the UN Framework Convention on Climate Change (the Paris Agreement). It is important to note that in the above OPEX calculation, it is necessary to clarify the tariffs for energy resources in a particular region.

Fluctuations in the cost of steam production may differ by 10%–15%. In this case, the calculation mentioned above shows a decrease in OPEX for MVR in the amount of 8–10 million euros per year, and the return on investment of CAPEX for MVR is reduced to 5 years. However, this calculation does not consider the specific costs of producing cooling water from cooling towers, which is 7.6 times higher at MEE compared to

MVR, and does not consider the costs of CO₂ emission quotas into the atmosphere [15]. If these costs are considered, the investment return period will be reduced from 5 years to 4 years.

It is reasonable to consider cogeneration by installing a turbine in a boiler room to reduce the purchase of electricity. Electricity is generated as a co-product in the cogeneration cycle using a turbine. As a result, additional electrical energy is generated from each normal cubic meter of natural gas with a total heat utilization coefficient of 82%–95%. In steam turbine installations, its share is about 28%–39%, in gas turbine installations was 30%–37%, in gas piston installations was 38%–48%, and in combined-cycle gas installations was 53%–62%. Therefore, CAPEX and OPEX should be considered when developing a feasibility study of technical solutions. International experience shows that electric energy costs 2.5 to 6 times greater than thermal energy. It is greater by 4 to 6 times in the central part of the Russian Federation, while in other regions of the Russian Federation is up to 6 to 7 times. That is why it is worth considering the operating costs of greenfield projects cogeneration. So, if one unit of heat costs one standard unit, then one unit of electricity will cost four standard units. Given that the efficiency of modern boilers reaches up to 95%, it can generate income in the amount of 95 standard units. Therefore, the formula of one installation will determine the total cost of generated energy resources:

$$F = F_{el} + F_{th, en} [\text{stand. unit}] \quad (1)$$

Thus, it is possible to estimate cogeneration units' cost and economic potential. If we consider an installation with one boiler and four turbines, we'll get the following: In a steam turbine (ST), an average of 34 units of electric energy and 53 units of thermal energy are obtained, then;

$$F_{st} = 34 \times 4 + 53 \times 1 = 189 \text{ standart units } (\$) \quad (2)$$

For a gas turbine (GT), this indicator will be:

$$F_{gt} = 33 \times 4 + 52 \times 1 = 184 \text{ standart units } (\$) \quad (3)$$

For gas piston (GPT), this indicator will be:

$$F_{gpt} = 43 \times 4 + 46 \times 1 = 218 \text{ standart units } (\$) \quad (4)$$

For combined-cycle gas (CCG):

$$F_{ccg} = 55 \times 4 + 33 \times 1 = 253 \text{ standart units } (\$) \quad (5)$$

Concerning a conventional boiler facility, the

economic effect will reach 199%, 194%, 229%, and 266%, accordingly. Thus, the technical solution for cogeneration in the process of brine evaporation is, on average, 200%–270% more profitable than using a boiler facility.

The disposal of exhausted gases from a combined heat and power plant should be considered with an absorption refrigeration unit (trigeneration) for cooling water production. The cogeneration-trigeneration cycle allows the use of resource-saving technologies and makes potash production energetically effective and should be one of the subjects of detailed analysis at the Pre-FEED and FEED stages. To develop optimal technology and make rational technical decisions on the disposal of excess brines, it is necessary to carry out a consistent study and analysis of technological solutions, infrastructure, and environmental risks at all project stages. For example, at the Pre-FEED stage, it is necessary to conceptually work out all possible industrial disposal methods with the determination of recycling volumes, feasibility studies of technical solutions, and environmental aspects.

Further development of the project will require implementing an integrated technical and economic assessment (PEA) with the introduction of additional factors - analysis of CO₂ emissions and social risks [15].

Problems of applying excess brine subsoil injection technology

In general, considering the global trends in the upgrading of industrial plants to "green production" and the implementation of such tools as carbon taxes and quota trading systems (STC, emissions trading system, ETS), the authors believe that it is reasonable to consider a combined approach with a ranking of the entire volume of processed brines [16]. For example, a possible solution for the disposal of excess brines from large brine storage facilities (with a volume of more than 3 million m³ per year) is a simultaneous use of an evaporation unit to obtain technical salt and unit of excess brines injection with a ratio of 60% to 40%. This proportion is determined by absorbing horizons and their porosity, as well as by a comparative analysis of the capital costs of evaporation and excess brine injection. Nowadays, the regulatory framework justifying the use of excess brines injection technology in Russia is in the formation process [17]. For example, the document regulating the procedure for considering applications for obtaining the right to use subsurface resources for placing liquid waste generated by mining enterprises engaged in exploration and production, as well as primary processing of potassium and magnesium salts in rock formations, was adopted only in November 2019.

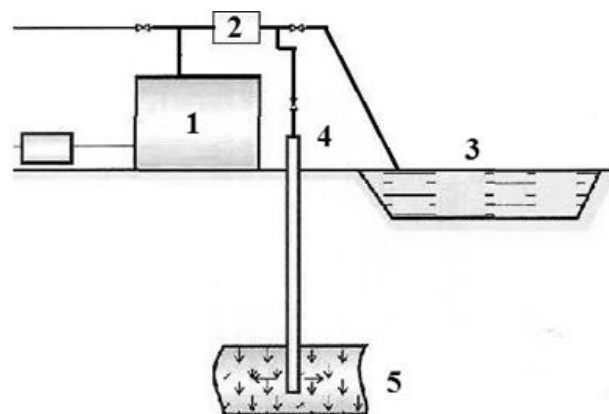


Figure 4. Enlarged system of excess brine disposal. 1 - Storage tanks for the accumulation of by-products at the processing plant; 2 - Pumping fleet; 3 - Surface brine storage; 4 - Injection well system; 5 - Receiving subsoil layer.

The sequence of work is not clearly structured because to apply for a geological study (in Greenfield form), "the conclusion of the state expert examination of geological information on the subsurface area" should be provided, and "information regarding the subsurface area planned for construction, as well as water generated by subsurface users, engaged in exploration and production, and primary processing of potassium and magnesium salts" is also required. In addition, the subsurface user must perform a pre-project study (including a seismic survey of the territory and drilling wells with collecting information about reservoirs) [18].

Further, after obtaining a license, developing a geological exploration project following the requirements is necessary. At the same time, it should be noted that nowadays, there are requirements for reservoir waters in Russia's oil and gas industry, and there are no special requirements for excess brine production.

The problem of environmental assessment with these approaches remains open - whether the geological exploration project is the object of such an examination [19]. Further, after passing the examination of geological information, it is required to develop a project of a complex for pumping. Thus, the issue of assessing the economic efficiency of the injection complex should be solved by the subsurface user already at the initial stage - since the implementation of the entire complex of studies will require large capital expenditures in the absence of a sufficient amount of information. Figure 4 shows an enlarged scheme of pumping excess brines into absorbing horizons. It follows from the above that it is possible to speak about the prospects of studying excess brine injection with a certain degree of confidence if the following factors are observed, in order of their significance:

1. The presence of a detailed geological study of the potash plant area by geophysical methods and the presence of geotectonic schemes;

2. The location of the potash plant in the oil/gas producing region or potentially oil and gas bearing region where the study of reservoirs was carried out.

3. Detailed study of infrastructure and environmental risks.

When analyzing environmental risks and preparing an environmental monitoring program, it is mandatory to use remote and high-precision methods for monitoring neotectonic movements and processes on the Earth's surface, which will allow to not only prevent risks related to the operation of the complex on time but also to level up the impact on the subsurface and the environment.

Problems of backfilling technology implementation

The existing technologies of backfilling waste have several features, especially in mining enterprises. Firstly, the limiting factor could be the volume of free subsurface space. As a result, the work schedule on the deposit becomes critical for waste backfilling [20]. The second limiting factor is the geomechanical stability of the filled chambers. Therefore, before carrying out the laying measures, it is necessary to determine the minimum required strength, which the laying mass should gain over time. Based on this, the management of the enterprise decides on the use of binding components in the backfilling mixture. Finally, the devices that are part of the backfilling pipelines and the pipes themselves are subjected to a complex hydroabrasive effect of the flow; this is primarily due to the peculiarities of their functioning, changes in the parameters of the conducted (pumped) medium, the specifics of the geometry of the joints, and has many limitations of either technical or natural and economic nature. Indeed, the operation of such systems and the maintenance of their operable condition and reliability generally are non-trivial problems [21].

It is important to consider the current processes and factors arising during the operation phase itself and the parameters that form its technical and technological characteristics when speaking about the reliability of pipelines as a system operating under conditions of waterjet wear. Thus, at the stage of pipeline design, the subsequent operational reliability is influenced by the rationality of design decisions (the sequence of system elements and their correspondence to each other and technological parameters), the choice of materials and components, and the choice of operating modes [22]. As a result, the backfilling method is a complex task faced by subsoil users. It requires a unified order of steps and investigations, considering all the abovementioned problems (Fig.5).

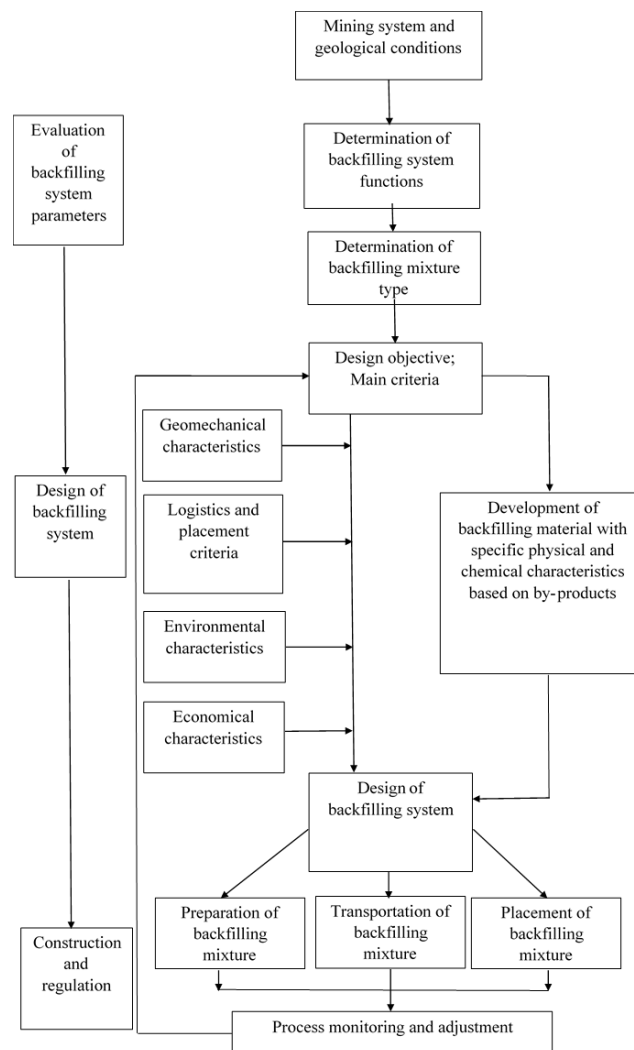


Figure 5. The procedure of development and implementation of a backfilling system at the processing of polymineral salts.

Thus, the use of each of the methods of polymineral production of by-products has several limitations, either technical, natural, or economic. In addition, it leads to the necessity of different method combinations to ensure both production volumes and environmental safety.

Combining disposal technologies in the extraction and processing of potash ores

A whole range of factors should be considered when investigating the optimization of technological choices for excess brine disposal at potash plants. Thus, the efficiency of the useful component recovery from spent liquor, the problem of maintaining the environmental safety of production, and ensuring the stability of the mountain massif with a hardening backfilling are not the only ones of great importance, but also the economic costs of implementing these measures [23].

First, it should be mentioned that the costs for each designated scheme can be capital and variable.

For example, capital expenditures may include the creation of a surface-laying complex, installing a cogeneration and trigeneration system at plants, purchasing a license to pump into deep horizons, etc. (Figure 6).

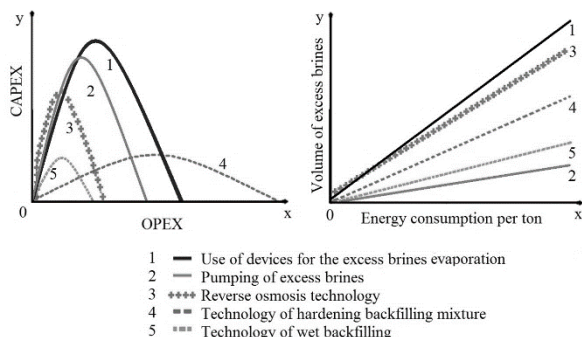


Figure 6. Generalized dependencies and modeling results typical for Eastern Europe: a - the volume of capital and operating costs by use of various technologies for the disposal of excess brines; b - the volume of disposal of excess brines from energy consumption per ton of the disposed of substance 1 - the use of devices for the evaporation of excess brines; 2 - the injection of excess brines; 3 - reverse osmosis technology; 4 - the technology of hardening reverse backfilling; 5 - the technology of hydro-backfilling.

Variable costs include the purchase of additional reagents and binders, consumables, and tax and fee payments. In part, these costs can be compensated by the additional product volumes for sale or by reducing deductions for unrealized by-products (rational use of subsurface resources).

Therefore, from a mathematical point of view, the problem under consideration can be represented as a series of functional dependencies (Fig. 6). On the one hand, the search for the minimum area value from the functions (in a simplified scheme, this is a two-dimensional model, the resulting of which is capital and operating costs for technological processes), and on the other hand, as the most effective volume ratio of recyclable material to energy costs [24].

As a result, a system of equations will be obtained. Its solution $R = (S_n, F_n)$ will allow us to find the optimal ratio of the technologies used to dispose of excess brines in specific project conditions [25]. It should be noted that in both equations, the minimum value of indicators will be optimal (both in terms of capital and current costs for the lye disposal (S_{opt}) and in terms of energy consumption per 1 ton of recycled lye (F_{opt})).

$$R = \left\{ \begin{array}{l} S_{opt} \rightarrow \min = \frac{\partial S}{\partial S_n}; \text{ where } S_n = \int_0^2 ax - x^2 dx; \\ F_{opt} \rightarrow \min = \frac{\partial F}{\partial F_n}; \text{ where } F_n = \frac{1}{2} ab \end{array} \right\} \quad (6)$$

CONCLUSION

Indeed, there may be one technological solution for disposing of excess liquor/lye at the plant, which will be determined by the method described above. However, as a rule, the company solves not only the tasks of minimizing financial costs for disposal but also several technical and technological tasks (ensuring the geomechanical stability of the minefield, ensuring the environmental friendliness of disposal processes, rational development of the subsoil) [26].

These factors can significantly influence the choice of a particular technology for excess lye disposal. As a rule, several technologies can be used simultaneously at the plant for various reasons.

Geocological security and stability of the territory development where such production is located require comprehensive studies on the possibility of using above mentioned methods. Sustainable development of the region adjacent to the enterprise with extraction and processing of polymineral raw materials will be possible only if the possibilities and safety of the natural environment for the by-products acceptance will be considered and accepted as the priority goal.

Modeling shows that for enterprises producing potash fertilizers based on mine extraction, the most optimal combination of technologies in terms of excess liquor disposal volume is: 60% disposed of by using vacuum evaporation plants while obtaining additional products, 20% by pumping excess brines through wells, 10%–20% by backfilling or membrane technologies with the additional recovery of potash salts. This ratio is obtained based on the result analysis of technical and economic calculations and practical experience of mining enterprises (the technological processes of enrichment used for the Khartsals of the Central European Tsekhstein salt basin are taken as the basis of modeling). A detailed description of the mathematical model that determines the cost and efficiency ratio of various by-product brine disposal methods is not given since it is company know-how and is currently undergoing the patenting procedure. At the same time, for various polymineral ores, such a model can be significantly changed (an important role is played not only by the physicochemical characteristics of the initial ore and the final products obtained but also by energy costs, capital investments, and environmental charges, which vary from country to country). The above calculations and modeling results will be closest to the conditions of Poland, Russia, Belarus, and Ukraine. The structure of the model will undergo much greater changes if the calculations are transferred to the examples of Germany and the UK (due to the changed energy and environmental costs) and significantly greater when applied to deposits in Canada or Australia. The final decision on the brine

disposal or a combination of various technical solutions is made at the technical and economic assessment (PEA), considering all technical, geological, economic, and environmental aspects, including potential CO₂ emissions. It is worth pointing out that the evaporation of lye by the MEE method is a direct source of CO₂ due to the significant consumption of coolant (steam). Therefore, it is promising to consider evaporation by the MVR method with the recycling of coolant, which can reduce steam consumption and make the technology resource-saving.

The life cycle of technologies for excess brine disposal is determined at the detailed engineering stage of evaporation and crystallization plants or filtration membranes. Therefore, it must correspond to the entire life cycle of the mining enterprise. The life cycle of IIDA is determined based on the presence of underground reservoirs and the pick-up of injection wells and is limited by these factors.

REFERENCES

- [1] N. Afrasiabi, E. Shahbazali, *Desalin. Water Treat.* 35 (2011) 39–53. <https://doi.org/10.5004/dwt.2011.3128>.
- [2] L. Shengo, *Water, Air, Soil Pollut.* 232 (2021) 273. <https://doi.org/10.1007/s11270-021-05198-w>.
- [3] C. Bilibio, C. Schellert, S. Retz, O. Hensel, H. Schmeisky, D. Uteau, S. Peth, *J. Environ. Manage.* 196 (2017) 633–643. <https://doi.org/10.1016/j.jenvman.2017.01.024>.
- [4] J. Shanxue, L. Yuening, P. Bradley, *Sci. Total Environ.* 59 (2017) 567–583. <https://doi.org/10.1016/j.scitotenv.2017.03.235>.
- [5] S. Shenvi, A. Isloor, A. Ismail, *Desalination* 368 (2015) 10–26. <https://doi.org/10.1016/j.desal.2014.12.042>.
- [6] C. Buckley, A. Simpson, C. Kerr, C. Schutte, *Desalination* 67 (1987) 431–438. [https://doi.org/10.1016/0011-9164\(87\)90260-8](https://doi.org/10.1016/0011-9164(87)90260-8).
- [7] J. Guozhao, W. Wang, C. Huihuang, Y. Siyuan, J. Sun, W. Fu, B. Yang, Z. Huang, *Desalination* 521 (2022) 115389. <https://doi.org/10.1016/j.desal.2021.115389>.
- [8] Z. Shiyong, Z. Huang, H. Wang, R. Liu, C. Cheng, S. Shuai, Y. Hu, Z. Guo, X. Yu, G. He, W. Fu, *Int. J. Min. Sci. Technol.* 31(6) (2021) 1145–1152. <https://doi.org/10.1016/j.ijmst.2021.09.001>.
- [9] Z. Huang, S. Shuai, H. Wang, R. Liu, S. Zhang, C. Cheng, Y. Hu, X. Yu, G. He, W. Fu, *Sep. Purif. Technol. Part B* 282 (2022) 119122. <https://doi.org/10.1016/j.seppur.2021.119122>.
- [10] Z. Huang, S. Zhang, F. Zhang, H. Wang, J. Zhou, X. Yu, R. Liu, C. Cheng, Z. Liu, Z. Guo, G. He, G. Ai, W. Fu, *J. Mol. Liq.* 313 (2020) 113506. <https://doi.org/10.1016/j.molliq.2020.113506>.
- [11] M. Scott, Å. Jernqvist, J. Olsson, G. Aly, *Appl. Therm. Eng.* 19(3) (1999) 279–298. [https://doi.org/10.1016/S1359-4311\(98\)00050-7](https://doi.org/10.1016/S1359-4311(98)00050-7).
- [12] P. Donnellan, K. Cronin, E. Byrne, *Renew. Sustain. Energy Rev.* 42 (2015) 1290–1304. <https://doi.org/10.1016/j.rser.2014.11.002>.
- [13] L. Urbanucci, D. Testi, *Energy Convers. Manage.* 200 (2019) 112062. <https://doi.org/10.1016/j.enconman.2019.112062>.
- [14] B.R. Sridevi, P.A. Hoskeri, C.M. Joseph, *Thin Solid Films* 723 (2021) 138584. <https://doi.org/10.1016/j.tsf.2021.138584>.
- [15] D. Dmitrieva, A. Ilinova, A. Kraslawski, *Resour. Policy* 52 (2017) 81–89. <https://doi.org/10.1016/j.resourpol.2016.11.004>.
- [16] G. Wenzhong, Q. Jiaye, J. Zhang, C. Guangming, D. Wu, *Int. J. Heat Mass Transfer* 144 (2019) 118552. <https://doi.org/10.1016/j.ijheatmasstransfer.2019.118552>.
- [17] I. Chaikovskiy, O. Korotchenkova, D. Trapeznikov, *Lithol. Miner. Resour.* 54 (2019) 308–319. <https://doi.org/10.1134/S0024490219040023>.
- [18] Q. Sun, J. Zhang, Q. Zhang, *Environ. Earth Sci.* 77 (2018) 234. <https://doi.org/10.1007/s12665-018-7414-6>.
- [19] B. Deng, Z. Jia, W. Liu, X. Liu, J. Gu, W. Ye, H. Wen, Z. Qu, *Energies* 14(4) (2021) 791. <https://doi.org/10.3390/en14040791>.
- [20] G. Ali, M. Fall, I. Alainchi, *J. Mater. Civ. Eng.* 33(3) (2021) 04020498. [https://doi.org/10.1061/\(ASCE\)MT.1943-5533.0003605](https://doi.org/10.1061/(ASCE)MT.1943-5533.0003605).
- [21] K. A. Hudson-Edwards, H. E. Jamieson, B. G. Lottermoser, *Elements* 7(6) (2011) 375–380. <https://doi.org/10.2113/gselements.7.6.375>.
- [22] C. Wolkersdorfer, D.K. Nordstrom, R.D. Beckie, *Mine Water Environ* 39 (2020) 204–228. <https://doi.org/10.1007/s10230-020-00666-x>.
- [23] M. Bortz, J. Burger, N. Aspiron, S. Blagov, R. Böttcher, U. Nowak, A. Scheithauer, R. Welke, K.-H. Küfer, H. Hasse, *Comput. Chem. Eng.* 60 (2014) 354–363. <https://doi.org/10.1016/j.compchemeng.2013.09.015>.
- [24] M.K.K. Nassar, R.M. El-Damak, A.H.M. Ghanem, *Environ. Earth Sci.* 54 (2008) 445–454. <https://doi.org/10.1007/s00254-007-0849-9>.
- [25] S. P. Philbin, *Res.-Technol. Manage.* 51(2) (2008) 32–39. <https://doi.org/10.1080/08956308.2008.11657493>.
- [26] M. S.Q. Domingues, L. Adelina, F. Baptista, M. Tato Diogo, *Int. J. Min. Sci. Technol.* 27 (4) (2017), 611–616. <https://doi.org/10.1016/j.ijmst.2017.05.007>.

PAVEL SHCHERBAN¹
ALEXANDER GAPCHICH²
ALEKSEY ZHDANOV³
OLGA LETUNOVSKAYA⁴

¹I. Kant BFU, Engineering and
Technical Institute, Kaliningrad,
Russia

²ICEMR RAS, Institute of
Comprehensive Exploitation of
Mineral Resources Russian
Academy of Sciences, Moscow,
Russia

³RSGU named after Sergo
Ordzhonikidze, Moscow, Russia

⁴Saint Petersburg Mining
University, St. Petersburg,
Russia

NAUČNI RAD

OPTIMIZACIJA METODA ODLAGANJA VIŠKA SLANIH RASTVORA U RUDNIKU I POSTROJENJU ZA PRERADU POTAŠE

U radu se analiziraju pozitivni i negativni aspekti različitih tehnoloških rešenja za slane rastvore koji se koriste pri razvoju poliminerálnih nalazišta rude potaše i razmatra problem određivanja izbora optimalnog pristupa uzimajući u obzir geološke, tehničke, ekološke i finansijske faktore. Proučavanje pitanja iskorišćavanja i smanjenja komponenti ispuštanja slanih rastvora u proizvodnji potašnih đubriva, istovremenog smanjenja gubitka vrednih komponenti sa tečnim ispuštima, a zbog toga i povećanja proizvodnje potašnih đubriva, kao i upotreba u tehnologiji rudničkog slanog rastvora, hitan su i važan naučni i inženjerski izazov industrije potaše. Tehnološki, nekoliko alternativnih rešenja može smanjiti broj tečnih nusproizvoda u skladištu mulja. U radu su korišćene analitičke metode, uključujući statističku obradu podataka, modelovanje, predprojektne studije tehnoloških rešenja i procenu ekonomskih troškova. Višak slanih rastvora iz rudnika i postrojenja za preradu potaše je tečni otpad koji se dobija tokom proizvodnje kalijumovih đubriva. Akumulacija viška slanih rastvora u skladištima mulja procenjuje se na milione kubnih metara godišnje. Međutim, proširenje prostora za skladištenje mulja i izgradnja brana su samo privremena rešenja. Oni su povezani sa rizicima u projektovanju, izgradnji i radu hidrauličnih objekata, povećavajući rizik od curenja slane vode u otvorene i podzemne vode. Zbog toga je neophodno koristiti druge metode odlaganja slane vode. U zavisnosti od prirode prerađenih poliminerálnih kalijumovih ruda, može se kombinovati nekoliko metoda za uklanjanje viška slanih rastvora: zatrpavanje, osmoza, ubrizgavanje u duboke slojeve i višestepeno isparavanje. Najoptimalnija kombinacija tehnologija redukcije slanog rastvora za postrojenje za preradu kalijumovih i magnezijumovih sirovina je sledeća: 60% se odlaže korišćenjem uređaja za vakuumsko isparavanje, 20% ubrizgavanjem viška rastvora soli u duboke slojeve, a 10%–20% treba koristi se za zatrpavanje ili proizvodnju dodatnih proizvoda.

Ključne reči: zatrpavanje, kogeneracija, višak slanih rastvora, prerada rude potaše, vakuumsko isparavanje.

NATAŠA MILIĆEVIĆ
MARIJANA SAKAČ
BOJANA ŠARIĆ
DUBRAVKA ŠKROBOT
BOJANA FILIPČEV
OLIVERA ŠIMURINA
PAVLE JOVANOVIĆ
MLADENKA PESTORIĆ
ALEKSANDAR MARIĆ

Institute of Food Technology in
Novi Sad, University of Novi Sad,
Novi Sad, Serbia

SCIENTIFIC PAPER

UDC 664.664.33:664.7:66.04

SOYBEAN BRAN AS THE FAT REPLACER IN GLUTEN-FREE COOKIE FORMULATION: PHYSICO-CHEMICAL PROPERTIES AND SENSORY PROFILES

Article Highlights

- Soybean bran was used in a gluten-free cookie formulation as a fat replacer (30%–50%)
- Dough properties, physical, textural, colour and sensory parameters of cookies were examined
- 30% fat replacement resulted in the most acceptable gluten-free cookies
- The nutritional properties of gluten-free cookies were investigated
- A novel value-added product for celiac patients has been developed

Abstract

Soybean bran (SB) partially replaced fat (30%–50%) in a gluten-free cookie formulation. Dough properties, physical (cookie dimension and weight loss), textural (hardness and fracturability), colour and sensory parameters, as well as nutritional profiles were evaluated to characterize full-fat (FFC) and fat-reduced cookies (FRC). Based on the obtained results, it was concluded that the fat reduction in cookie formulation at 30% maintained the sensory properties of the FFC. Furthermore, it was revealed that the fat replacement using SB at 30% resulted in the fat-reduced value-added gluten-free cookies in terms of dietary fibre and minerals. A daily portion of the 30% FRC meets 11.87% and 18.04% of dietary reference intakes (DRIs) for dietary fibres, 26.50% of DRIs for calcium, 35.71% and 46.88% of DRIs for magnesium and 65.43% and 83.61% of DRIs for manganese, for male and female adults, respectively.

Keywords: gluten-free cookies, fat replacers, soybean bran, physicochemical properties, sensory analysis.

Celiac disease is an autoimmune enteropathy triggered by ingesting gluten-containing grains (wheat, barley, rye and possibly oats) in genetically susceptible individuals. Therefore, celiac disease patients are recommended to be on a strict long-life gluten-free diet, which usually lacks in vitamin B, dietary fibres and iron [1,2]. Moreover, an imbalance in the intake of carbohydrates, fat and protein exists in a gluten-free diet [1].

Having in mind that high fat intake has adverse

effects on human health and leads to the development of several diseases (obesity, diabetes, cancer, high cholesterol levels and coronary heart diseases), many efforts have been made to reduce fat content in foods regardless of the food category (gluten-containing or gluten-free foods) and replace it with various fat replacers [3,4,5].

Carbohydrate-based fat replacers act as fat mimetics as they form a gel in the presence of water with a flow pattern similar to one of the lipids [6]. Recently, there has been growing interest in valorizing fibre-containing by-products as potential raw materials for producing fat replacers [7]. Cereal milling fractions rich in fibre can serve as fat replacers. The studies with corn bran fibre [8,9], soluble fibre from corn and oats [10], fibre gel produced from rice bran [11] and wheat and oat bran gels [12] were conducted to investigate the possibilities of their utilization as the fat replacers.

Correspondence: A.Marić, Institute of Food Technology in Novi Sad, University of Novi Sad, Bulevar cara Lazara 1, 21000 Novi Sad, Serbia.

E-mail: aleksandar.maric@fins.uns.ac.rs

Paper received: 22 December, 2021

Paper revised: 29 August, 2022

Paper accepted: 9 September, 2022

<https://doi.org/10.2298/CICEQ211222025M>

Furthermore, the particular benefit of fibre-containing cereal by-products used as fat replacers is their fibre abundance, which can significantly contribute to the functionality of the obtained low-fat products, especially in gluten-free products, which can often have a weak nutritional and functional profile. Besides increasing the total dietary fibre content in food products, cereal brans can enrich the food with bioactive compounds [12].

Soybean is the most important source of edible plant oil and protein worldwide. To obtain flour and oil, soybean bran (SB) is obtained as a by-product during soybean processing. Thousands of tons of SB and dregs are generated as agricultural by-products and are typically discarded and wasted. Having an insight into its proximate composition and dietary fibre content, 59.9%–72.2% insoluble fibre (IDF) and 3.9%–12.7% soluble fibre (SDF) [13], it seems that SB could be used as a fibre-containing fat replacer in a cookie formulation. Furthermore, since SB is a good source of IDF, it could possess a prebiotic effect on the faecal microbiota [14]. However, no research has been conducted exploring this type of bran as the fat replacer in cookie formulation. In addition, the absence of gluten in SB classifies it as a potential fat replacer for gluten-free food production, such as cookies.

Insufficient amounts of nutrients in gluten-free cookies can be overcome by their fortification to achieve a balanced diet, i.e. to obtain value-added products. For that reason, the authors decided to produce gluten-free fat-reduced cookies (FRC) using SB, aiming to 1) investigate the effects of incorporation of SB as the fat replacer into the cookie formulation on dough characteristics, as well as physical, textural, colour and sensory properties of cookies and 2) characterize cookies in terms of nutritional profiles.

MATERIALS AND METHODS

Raw materials

SB was obtained from AD "Sojaprotein", Bečej, Serbia. SB was double ground to obtain fine granulation (mean particle size < 300 µm). As a result, SB contained 7.90% moisture, 14.8% proteins, 12.7% carbohydrates (the sum of starch and total reducing sugars content), 4.40% fat, 3.96% ash, and 55.3% total dietary fibres on a wet basis.

A gluten-free mixture consisting of corn starch, corn flour, potato starch, potato flour, rice flour, guar gum, baking powder, and salt was purchased from "Nutri Allergy Center", Zemun, Serbia. In addition, vegetable fat, glucose syrup, baking powder, salt, soy lecithin, corn grits and spices were commercially available.

Preparation of gluten-free cookies

Full-fat (FFC) and fat-reduced gluten-free cookies (FRC) were produced using the ingredients listed in Table 1.

Table 1. Ingredients of gluten-free cookie formulations.

Ingredients (%)	Full-fat cookies	30% SB cookies ^a	40% SB cookies ^b	50% SB cookies ^c
Gluten-free mix	100	100	100	100
Vegetable fat	30.18	21.12	18.10	15.09
Soybean bran	0	9.05	12.07	15.09
Glucose syrup	10.71	10.71	10.71	10.71
Spices	4.64	4.64	4.64	4.64
Corn grits	3.57	3.57	3.57	3.57
Salt	1.79	1.79	1.79	1.79
Soy lecithin	0.71	0.71	0.71	0.71
Baking powder	0.54	0.54	0.54	0.54
Water	42.86	48.67	54.00	59.33

^a cookies in which 30% of fat was replaced with SB; ^b cookies in which 40% of fat was replaced with SB; ^c cookies in which 50% of fat was replaced with SB.

The cookie dough was made in a farinograph mixing bowl (Brabender, Duisburg, Germany) at 30 °C. The dough was prepared using the following method: vegetable fat was mixed with glucose syrup for 3 min to obtain a homogenous mixture, in which the solution of salt, with the rest of distilled water, was added and mixed for 5 min. Finally, all powdery ingredients (gluten-free mixture, SB, corn grits, spices and baking powder) were mixed for 2 min. The dough was kept in a refrigerator for 24 h for better hydration of SB. Afterwards, the dough was tempered to ambient temperature and further processed. A pilot-scale dough sheeter (Mignon, Mestrino, Italy) was used for sheeting the dough to the desired thickness (4.5 mm). Cookies were shaped using a cutter (40 mm × 30 mm) and baked at 220 °C for 2 min and then at 160 °C for 14 min in a laboratory oven (MIWE gusto® CS, Berlin, Germany). The obtained gluten-free cookies were first left to cool down at ambient temperature for 2 h, and then they were packed and stored for 24 h in sealed polypropylene bags before analysis.

Textural properties of cookie dough

Textural properties of cookie dough were measured on a texture analyzer TA-XTplus (TA.XTplus, Stable Micro System, Godalming, United Kingdom). TPA analysis was performed to measure dough properties in compression. The test settings were: test speed 1 mm/s, 50% strain, pause between compressions 5 s. Dough pieces were 46 mm in diameter, and a 75 mm probe was used. Dough hardness, adhesiveness, springiness and resilience were recorded. Dough hardness was also measured in penetration mode using a dough preparation set (A/DP) with a 6 mm cylinder probe. The test settings were: test speed 3 mm/s, distance 20 mm. Each test was carried out on six replicates of each formulation.

Cookie dimensions and weight loss

Cookie dimensions were determined by measuring the length (L), width (W) and height (H) using a digital calliper. The measurements were obtained 30 min after baking in six replicates per batch at ambient temperature ($25\text{ }^{\circ}\text{C} \pm 1\text{ }^{\circ}\text{C}$).

Baking weight loss (BWL) was determined by measuring the cookie weight before and after baking. It was calculated according to the following Eq. 1:

$$BWL(\%) = \frac{m_0 - m_t}{m_0} \times 100 \quad (1)$$

where m_0 is the cookie weight before baking, and m_t is the weight after baking. Cookie weight (m_0 and m_t) was determined as the average value of six independent measurements.

Textural properties of cookies

The texture of cookie samples was determined on a TA-XT2 Texture Analyzer (Stable Micro System, Godalming, United Kingdom) equipped with a 30 kg load cell and three-point bending rig (HDP/3PB). The measurements were done in a compression mode using the crosshead speed of 3 mm/s during analysis and a travel distance of 8 mm. Cookie samples were placed on supports with a 20 mm gap length.

Maximum force and distance at break were registered and represented indicators of cookie hardness and fracturability. Measurements were performed 24 h after baking in six replicates per batch at ambient temperature ($25\text{ }^{\circ}\text{C} \pm 1\text{ }^{\circ}\text{C}$).

Colour determination

The colour of the top surface of the cookies was measured 24 h after baking using a chromameter Minolta CR-400 (Konica Minolta Co., Osaka, Japan). The results were expressed as L^* (brightness/darkness), a^* (redness/greenness) and b^* (yellowness/blueness). Browning index (BI) was calculated from Eq. 2 [15]:

$$BI = \frac{[100 \times (X - 0.31)]}{0.172} \quad (2)$$

where X is calculated according to the following Eq. 3:

$$X = a^* + 1.75L^* + a^* - 3.012b^* \quad (3)$$

The total colour difference (ΔE) between the reference (control) and cookie samples with SB was calculated according to the following Eq. 4:

$$\Delta E = \sqrt{\Delta L^{*2} + \Delta a^{*2} + \Delta b^{*2}} \quad (4)$$

where ΔL^* is the difference in L^* values between FFC and FRC; Δa^* is the difference in a^* values between FFC and FRC, and Δb^* is the difference in b^* values between FFC and FRC. Colour measurements were taken from each sample in 25 replications (five points, 1 central and 4 corner points, on 5 randomly selected samples per batch).

Hydroxymethylfurfural (HMF) in cookies

The extraction procedure was performed according to the method proposed by Rufián-Henares *et al.* [16] with the modifications done by Petisca *et al.* [17]. First, ten grams of sample were suspended in 5 mL water:methanol (70:30). The mixture was thoroughly stirred for 1 min, and then 2.0 mL of Carrez I and Carrez II solutions were added and centrifuged at 5000 rpm ($4\text{ }^{\circ}\text{C}$) for 15 min, recovering the supernatant to a 15 mL flask. Next, two more consecutive extractions were made with 2 mL of water:methanol (70:30) until collecting 10 mL of supernatant was. Finally, two millilitres of this solution were centrifuged at 8000 rpm for 15 min before being analyzed. The chromatographic separation and quantification of HMF were performed using the HPLC method described by Ariffin *et al.* [18] and Tomasini *et al.* [19] with some modifications. A liquid chromatograph (Agilent 1200 series), equipped with a DAD detector and an Eclipse XDB-C18, 1.8 μm , 4.6 mm \times 50 mm column (Agilent), was used for quantification of HMF in the obtained extracts. The injected volume was 2 μL , and the temperature was set at $30\text{ }^{\circ}\text{C}$. The mobile phase consisted of an isocratic mixture of methanol:water (0.1% formic acid), ratio 10:90 (v:v) at a constant flow of 0.75 mL/min. The DAD wavelength was set at 284 nm. The total run time of the analysis was 5 min.

All tests were performed in triplicate, and the results were averaged.

Sensory evaluation

Sensory descriptive analysis of cookies was performed 24 h after baking at the Accredited Laboratory for Sensory Analysis at the Institute of Food Technology, University of Novi Sad, Novi Sad, Serbia, respecting all protocols to avoid harm and risks to the participants. Sensory evaluation was conducted by the trained sensory panel (7 females and one male, 30–50 years of age). The panellists were recruited from a staff working at the Institute of Food Technology in Novi Sad and selected by their sensory abilities according to ISO 8586:2012 [20]. All panellists received written information about the study, and they signed informed consent to participate. The Institute of Food Technology Ethics Committee approved the study in Novi Sad, University of Novi Sad, Novi Sad, Serbia

(Ref. No. 175//10-3).

Panellists evaluated colour nuance, bran visibility, bran odour intensity, saltiness, overall flavour intensity, bran flavour intensity, fracturability, hardness and quality. The intensities of sensory properties were evaluated on a 100 mm line scale, from the lowest intensity (left side) to the highest intensity (right side of the scale). Every panellist was given two cookies per sample in closed odourless plastic containers at ambient temperature ($25\text{ }^{\circ}\text{C} \pm 1\text{ }^{\circ}\text{C}$) labelled with three randomly chosen digit numbers and drinking water for palate cleansing.

Nutritional cookie profile

Proximate composition of cookies including protein (Method No. 950.36), fat (Method No. 935.38), total dietary fibre (Method No. 958.29), reducing sugar (Method No. 975.14), ash (Method No. 930.22) and moisture content (Method No. 926.5) was determined by AOAC standard methods of analysis [21]. In addition, according to ICC Standard No. 123/1 [22], starch content was determined by hydrochloric acid dissolution.

Minerals were determined by atomic absorption spectrophotometry (Method No. 984.27) on a Varian Spectra AA 10 (Varian Techtron Pty Ltd., Mulgavre Victoria, Australia).

Statistical analysis

Results were expressed as mean \pm standard deviation of triplicate analyses for all measurements, except the colour determination performed in 25 repetitions, as well as texture measurements of dough and cookies and R, T and BWL measurements were done in 6 repetitions. Statistical differences between samples were evaluated using a one-way analysis of variance (ANOVA) followed by Tukey's minimum square difference test. The difference between groups was considered significant at $p \leq 0.05$. All data were analyzed using the software package STATISTICA 10.0 (StatSoft Inc., Tulsa, OK, USA). Sensory descriptive data were analyzed using the software package XLSTAT 2018.7 (Addinsoft, Long

Island, NY, USA).

RESULTS AND DISCUSSION

Texture analysis of cookie dough

The replacement of fat (30%–50%) in the gluten-free cookie formulation using SB affected the textural properties of the cookie dough. SB can mimic fat functionality in food systems due to the presence of a high amount of fibre (55.3%), taking into account that fibres are known to have the ability to absorb considerable amounts of water and thus express gelling properties [23]. It was the reason for initially adding higher water in the bran-containing cookie doughs than the control one (adding bran in cookie formulation increased the amount of water required to obtain workable consistency). Villemejeane *et al.* [24] also found that incorporating fibres in biscuit formulation required increasing dough hydration.

Increasing SB in the cookie formulation led to increased dough hardness and resilience (Table 2). The results agree with Sudha *et al.* [25] and Pareyt *et al.* [26], who also concluded that fat reduction resulted in increased cookie dough hardness. Since fat is the essential ingredient associated with dough processability and the baking quality of the product, increased hardness of SB-containing dough was related to a decrease in fat content. Furthermore, Sanchez *et al.* [27] also found that decreasing fat content in cookie dough formulations increased resilience.

The elastic properties of the dough are characterized by springiness, which was decreased by reducing the fat content in the formulation, and the adhesiveness decreased in the same manner. Decreasing adhesiveness could be interpreted as an improvement because stickiness is considered a common problem in the baking industry and is not desired behaviour for cookie production [28]. However, no significant ($p \leq 0.05$) differences in cookie dough springiness and adhesiveness were observed between cookies with different fat replacement levels (30%–50%).

Table 2. Dough properties of the control (full-fat) gluten-free cookie formulation and fat-reduced gluten-free cookie formulations.

	Full-fat dough	30% SB dough	40% SB dough	50% SB dough
Hardness (kg)	(13.3 \pm 1.76) ^a	(27.7 \pm 3.13) ^b	(29.7 \pm 1.56) ^{b,c}	(35.9 \pm 2.83) ^c
Adhesiveness (kg/s)	(2.85 \pm 0.35) ^b	(0.57 \pm 0.16) ^a	(0.49 \pm 0.20) ^a	(0.20 \pm 0.06) ^a
Springiness	(0.75 \pm 0.14) ^b	(0.34 \pm 0.05) ^a	(0.35 \pm 0.04) ^a	(0.40 \pm 0.04) ^a
Resilience	(0.15 \pm 0.01) ^a	(0.26 \pm 0.01) ^b	(0.28 \pm 0.02) ^b	(0.34 \pm 0.02) ^c
Hardness (kg)	(0.22 \pm 0.02) ^a	(0.52 \pm 0.03) ^b	(0.59 \pm 0.04) ^c	(0.61 \pm 0.01) ^c

Values are means ($n = 6$) \pm standard deviations; Means in the same row with different superscripts are statistically different ($p \leq 0.05$).

Cookie dimensions and weight loss

Partial replacement of vegetable fat in the cookie formulation by finely ground SB at 30%–50% level

influenced cookie dimension and weight loss during baking (Table 3). Weight loss during baking is a consequence of water evaporation, which was lower in

FRC, but there were no significant ($p \leq 0.05$) differences between the control cookies and FRC (Table 3). Although a higher level of SB might have caused better water retention in the dough, making water less available for easy evaporation [29], no significant differences between the samples were observed.

Cookie width decreased with an increasing level of fat substitution by SB, but a significant ($p \leq 0.05$) difference was observed only in the case of the highest replacement level (50%). Similarly, length gain was lower in FRC, but there were no significant ($p \leq 0.05$) differences between samples. FRC's height was higher than the control's but did not reach statistical significance ($p \leq 0.05$). Similar observations were published by Pareyt *et al.* [26], who concluded that less cookie spread was associated with a lower fat content due to impaired lubrication and decreased mobility in the dough system. The same authors noticed that increasing fat contents correlated linearly ($R^2 = 0.98$) with increasing cookie diameter and, consequently, with decreasing cookie height. Lee and Inglett [30] found that cookie diameter significantly decreased and its thickness significantly increased when shortening was replaced by oat bran in a cookie formulation.

Textural properties of cookies

The effect of fat replacement with SB on the

textural properties of gluten-free cookies is summarised in Table 3. The hardness values ($p \leq 0.05$) increased with increasing levels of fat replacer in the cookie formulation. The obtained results agree with Pareyt *et al.* [26] and Laguna *et al.* [31]. It happens because the major role of fat is lubrication by coating the matrix; less fat allows higher accessibility of flour and fibre particles to water. Higher hydration leads to the formation of harder doughs (Table 2) and, hence, harder cookies [26]. Chevallier *et al.* [32] considered that dough with reduced fat content is characterized by a smaller amount of incorporated air, leading to a more pronounced strength of the cookies. The force required to break cookies containing 50% less fat than the control sample was more than three times higher than that required to break the control ones. This finding agreed with our earlier results, where fat was replaced with oat and wheat bran gels in a cookie formulation [12].

Fat replacement using SB in the gluten-free cookie formulation resulted in a less fracturable product (as shown by an increase in the distance at break). Still, the differences were not significant ($p \leq 0.05$) (Table 3).

In general, the textural measurements indicate that using SB as the fat replacer resulted in cookies with a less tender texture, suggesting that lower amounts of SB in FRC were acceptable.

Table 3. Physical and textural characteristics, colour parameters, browning index and HMF content of the control (full-fat) gluten-free cookies and fat-reduced gluten-free cookies.

	Full-fat cookies	30% SB cookies	40% SB cookies	50% SB cookies
		Physical properties		
BWL (%)	(23.5 ± 0.19) ^a	(23.5 ± 0.56) ^a	(22.6 ± 0.31) ^a	(21.9 ± 0.48) ^a
Width change (%)	+4.41 ^b	+1.41 ^{a,b}	+0.20 ^{a,b}	-1.71 ^a
Length change (%)	-0.55 ^a	-0.39 ^a	-3.40 ^a	-1.63 ^a
Height gain (%)	+30.55 ^a	+35.26 ^a	+32.43 ^a	+30.60 ^a
		Textural properties		
Hardness (g)	(2880 ± 456) ^a	(5349 ± 829) ^b	(8974 ± 955) ^c	(9520 ± 1118) ^c
Fracturability (mm)	(0.69 ± 0.15) ^a	(0.78 ± 0.06) ^a	(0.83 ± 0.11) ^a	(0.91 ± 0.06) ^a
		Colour parameters		
L^*	83.12 ^c	74.67 ^b	71.41 ^a	71.10 ^a
a^*	-0.47 ^a	1.30 ^b	1.89 ^c	2.05 ^d
b^*	23.98 ^c	22.70 ^b	22.30 ^{ab}	22.13 ^a
BI	32.36 ^c	36.24 ^b	38.08 ^a	38.12 ^a
ΔE		8.72 ^a	12.00 ^b	12.42 ^b
HMF (mg/kg)	0.11 ^a	0.11 ^a	0.11 ^a	0.11 ^a

BWL - baking weight loss; L^* - lightness; a^* - a colour coordinate (red tone); b^* - b colour coordinate (yellow tone); BI - browning index; ΔE - colour differences; HMF - hydroxymethylfurfural. Values are means ($n = 6$ for physical and textural properties; $n = 25$ for colour parameters; $n = 3$ for HMF content) ± standard deviations. Means in the same row with different superscripts are statistically different ($p \leq 0.05$).

Colour parameters and HMF content of cookies

Colour is essential in the consumer's acceptance of a food product. Fat replacement with SB caused significant ($p \leq 0.05$) changes in L^* , a^* and b^* values (Table 3). In addition, cookies with SB were significantly darker, redder and less yellow than the control sample. Sudha *et al.* [25] also reported that the colour of wheat cookies became darker when bran from different sources (wheat, rice, oat, and barley) was incorporated

into the formulation.

There was a significant ($p \leq 0.05$) increase in the browning index in cookies containing SB. The browning index (BI) represents the purity of brown colour and is reported as an important parameter in processes where enzymatic or non-enzymatic browning occurs [15]. The production of brown pigments in baked goods is mainly caused by the Maillard reaction and caramelization [33]. These reactions are influenced by many factors, such as pH, high temperature, low moisture content, sugar,

protein, fat, amino acid and dietary fibre content [34]. However, the obtained BI results in Table 3 indicated that cookies were darker due to the increasing amount of SB in the cookie formulation, i.e. they could not be addressed to the development of Maillard reaction products. Namely, HMF, the Maillard reaction product formed during baking, was under the limit of quantification in all examined cookie samples (Table 3). Therefore, it suggests that the non-enzymatic browning reaction was not intensely expressed in the production of gluten-free cookies.

Calculated CIELAB colour difference (ΔE) between the FFC and FRC exceeds the limit for sensory perceptibility ($\Delta E > 0.5$) [35] (Table 3), thus indicating that cookies exhibited different colours from a sensory point of view, as well.

Sensory evaluation

The sensory properties of cookies evaluated by the panel were correlated with the instrumentally measured textural and colour properties. The PCA graph (Fig. 1) shows the sensory space characterized by four cookie samples considering nine evaluated attributes. The parameters measured instrumentally were over-imposed into the map as supplementary variables. Samples were well discriminated against

based on the evaluated attributes. The control FFC sample was associated with positive attributes for this type of product (saltiness, fracturability and overall flavour intensity) and with significantly ($p \leq 0.05$) higher overall quality in comparison to other analyzed cookie samples. Using SB as the fat replacer led to statistically significant ($p \leq 0.05$) changes in the sensory profile of gluten-free cookies. Samples 40% SB and 50% SB became darker with highly visible bran particles, the bran odour and flavour, were more pronounced, and the hardness increased. At the same time, fracturability decreased, and these samples were scored with a lower overall quality. It was observed that overall quality significantly ($p \leq 0.05$) declined when fat was replaced with SB at levels higher than 30%. On the other hand, replacing 30% of fat with SB did not appreciably impair colour nuance, savoury taste, overall flavour intensity, fracturability, hardness and overall quality compared to the control FFC. Textural parameters measured instrumentally (hardness and firmness) were highly correlated to sensory-evaluated hardness ($R = 0.979$, $p \leq 0.05$) and firmness ($R = -0.939$, $p \leq 0.05$). Colour parameters (L^* , a^* and b^*) were well correlated with bran visibility ($RL^* = -0.980$, $Ra^* = 0.986$, $Lb^* = -0.989$, $p \leq 0.05$) and flavour intensity ($RL^* = -0.976$, $Ra^* = 0.975$, $Lb^* = -0.975$, $p \leq 0.05$).

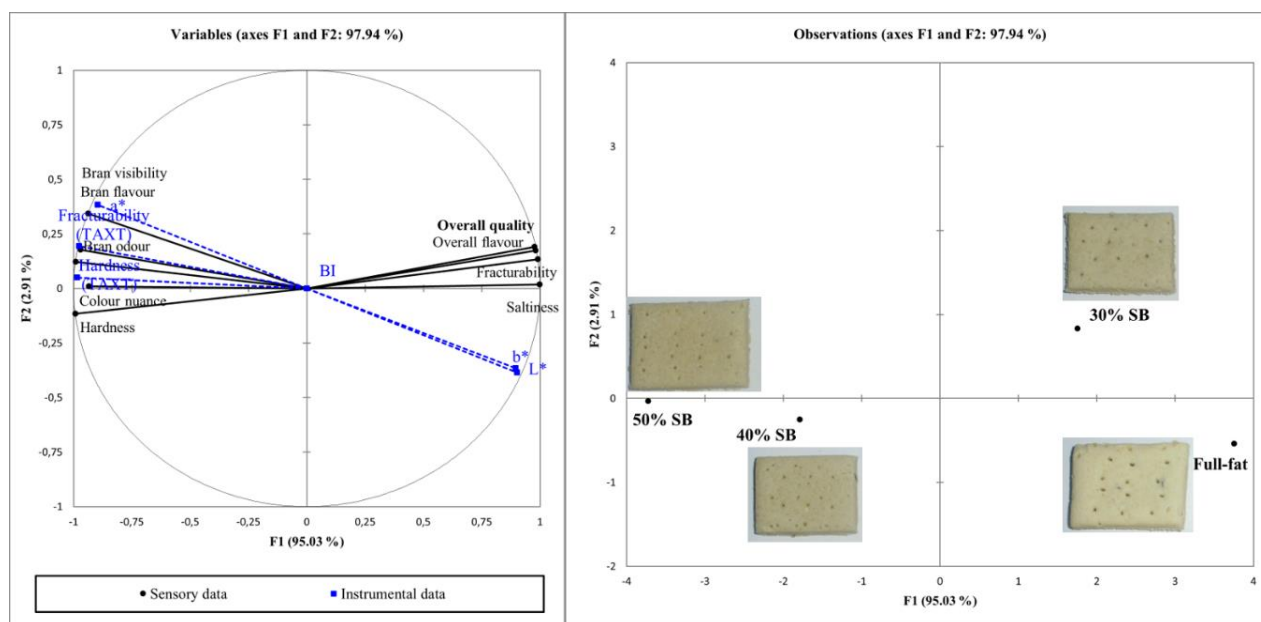


Figure 1. PCA plot performed with the scores of sensory attributes (left side) evaluated for gluten-free cookies (right side) together with instrumentally measured parameters of texture and colour as supplementary quantitative variables.

Nutritional cookie profile

The content of macronutrients (proteins, carbohydrates, fats, and dietary fibres) and minerals (Na, K, Ca, Mg, Fe, Zn, Cu and Mn) were determined in the control and FR gluten-free cookies to demonstrate the effect of the fat replacement with SB on the nutritional profile of gluten-free cookies (Table 4). The

results indicated significant ($p \leq 0.05$) increases in protein, ash and dietary fibre content in FRC. Carbohydrates decreased in comparison to the control cookies. However, no significant ($p \leq 0.05$) differences in FRC concerning the fat replacement level were observed. Compared to the control, fat content decreased significantly ($p \leq 0.05$) by 14.01%, 28.68%

and 37.58% in samples with 30%, 40%, and 50% fat replacement using SB. Furthermore, gluten-free cookies with 30% of SB could be considered a high-fibre product [36] (Table 5). Moreover, an average daily portion of gluten-free cookies with 30% of SB (50 g) would meet 11.87% and 18.04% of DRIs for dietary fibres for male and female adults, respectively [37] (Table 5). It is important due to its possible contribution to enhancing the dietary fibre status of celiac patients. As is known, the consumption of an adequate amount of dietary fibres is related to important health benefits such as the prevention of colon cancer, diabetes and cardiovascular disease [38]. Gluten-containing cookies used as representatives of commercially available products had dietary fibre content to meet 12% to 20% of DRIs [33] with a portion of 50 g (data obtained by analyzing their nutrition labels). Therefore, it can be

concluded that gluten-free cookies with 30% of SB were comparable with gluten-containing counterparts.

Gluten-free products are often low in micronutrients, contributing to the risk of deficiencies [39]. Increasing substitution levels increased the mineral content of gluten-free cookies. Marked increases were recorded for all observed macro and microelements (K, Ca, Mg, Fe, Zn and Mn) except for sodium and copper, which was less pronounced (Table 4). By substituting fat with SB at 30%, a significant increase in the contribution of minerals intake to the recommended DRIs was achieved (Table 5). FR gluten-free cookies meet 26.50% of DRIs (for adults) for calcium, 35.71% and 46.88% of DRIs (for males and females) for magnesium and 65.43% and 83.61% of DRIs (for males and females) for manganese (Table 5).

Table 4. Proximate composition and mineral contents of the control (full-fat) gluten-free cookies and fat-reduced gluten-free cookies.

Proximate composition	Full-fat dough	30% SB dough	40% SB dough	50% SB dough
Proteins (g/100 g d.m.)	(2.73 ± 0.01) ^a	(3.42 ± 0.04) ^b	(3.61 ± 0.03) ^c	(4.35 ± 0.04) ^d
Carbohydrates (g/100 g d.m.)	(77.6 ± 0.18) ^b	(75.1 ± 0.09) ^a	(75.4 ± 0.19) ^a	(75.4 ± 0.16) ^a
Fat(g/100 g d.m.)	(18.4 ± 0.30) ^d	(15.8 ± 0.36) ^c	(13.1 ± 0.08) ^b	(11.5 ± 0.11) ^a
Dietary fibre(g/100 g d.m.)	(4.10 ± 0.21) ^a	(9.02 ± 0.34) ^b	(10.3 ± 0.20) ^c	(11.4 ± 0.18) ^d
Ash (g/100 g d.m.)	(1.00 ± 0.01) ^a	(1.04 ± 0.01) ^b	(1.10 ± 0.02) ^c	(1.24 ± 0.01) ^d
Minerals				
Na (g/100 g d.m.)	(6.54 ± 0.01) ^b	(6.59 ± 0.01) ^c	(6.58 ± 0.01) ^{b,c}	(6.44 ± 0.00) ^a
K (g/100 g d.m.)	(0.72 ± 0.00) ^a	(1.62 ± 0.03) ^b	(1.93 ± 0.02) ^c	(2.55 ± 0.01) ^d
Ca (g/100 g d.m.)	(0.17 ± 0.00) ^a	(0.53 ± 0.001) ^b	(0.64 ± 0.02) ^c	(0.81 ± 0.00) ^d
Mg (g/100 g d.m.)	(0.17 ± 0.01) ^a	(0.30 ± 0.00) ^b	(0.34 ± 0.00) ^c	(0.37 ± 0.01) ^d
Fe (mg/100 g d.m.)	(8.21 ± 0.07) ^a	(36.5 ± 0.46) ^b	(47.6 ± 0.47) ^c	(49.6 ± 0.76) ^d
Zn (mg/100 g d.m.)	(3.86 ± 0.01) ^a	(14.1 ± 0.44) ^b	(14.5 ± 0.29) ^{b,c}	(14.9 ± 0.04) ^c
Cu (mg/100 g d.m.)	(1.71 ± 0.28) ^a	(1.80 ± 0.15) ^a	(1.66 ± 0.24) ^a	(2.02 ± 0.09) ^a
Mn (mg/100 g d.m.)	(1.48 ± 0.04) ^a	(3.01 ± 0.04) ^b	(3.32 ± 0.03) ^c	(3.98 ± 0.09) ^d

Carbohydrate content represents the sum of starch and total reducing sugars content. Values are means ($n = 3$) ± standard deviations. Means in the same row with different superscripts are statistically different ($p \leq 0.05$).

Table 5. Contribution of macronutrients and micronutrients intake to the recommended DRIs based on the average portion (50 g) of cookies consumption.

	Gender	DRIs	Contribution to DRIs (%)	
			Full-fat cookies	30% SB cookies
Macronutrient (g/day)				
Protein (g/day)*	Male	56	2.44	3.05
	Female	46	2.97	3.72
Carbohydrate	Adults	130	29.84	28.87
Fat	Adults	nd	/	/
Dietary fibre	Male	38	5.39	11.87
	Female	25	8.02	18.04
Micronutrients (mg/day)				
Ca	Adults	1000	8.50	26.50
Mg	Male	420	20.24	35.71
	Female	320	26.56	46.88
Mn	Male	2.3	32.17	65.43
	Female	1.8	41.11	83.61

nd - not determined. DRIs - Dietary Reference Intake set by the Food and Nutrition Board of the National Research Council for male and female adults (30–50 years of age); *Based on g protein per kg of body weight for the reference body weight, e.g., for adults, 0.8 g/kg body weight for the reference body weight [37].

CONCLUSION

FR gluten-free cookies were produced using SB at 30%–50%. FRC was compared with the FFC evaluating their textural dough properties, physical (cookie dimension and weight loss), textural (hardness and fracturability), colour and sensory parameters, and nutritional profile. Based on the investigated characteristics, it was evident that fat substitution at the level of 30% did not distinctly affect the cookie profile. Furthermore, the value-added cookies containing 30% of SB instead of fat were superior in dietary fibre and minerals to the control cookies. So, it is possible to obtain highly acceptable gluten-free cookies with fat content reduced by 30%, whereas fibre content was more than 2 times higher than in the control sample. These cookies represent a novel value-added product for celiac patients as a valuable source of essential nutrients.

ACKNOWLEDGEMENT

This work was financially supported by the Ministry of Education, Science and Technological Development, Republic of Serbia (Contract No. 451-03-68/2022-14/200222).

REFERENCES

- [1] L. Alvarez-Jubete, E.K. Arendt, E. Gallagher, *Trends Food Sci. Technol.* 21 (2010) 106–113. <https://doi.org/10.1016/j.tifs.2009.10.014>.
- [2] V. Talarico, L. Giancotti, G.A. Mazza, R. Miniero, M. Bertini, *Nutrients* 13 (2021) 1695. <https://doi.org/10.3390/nu13051695>.
- [3] O.E. Shaltout, M.M. Youssef, *Alexandria J. Food Sci. Technol.* 4 (2007) 29–44. <https://doi.org/10.21608/AJFS.2007.19631>.
- [4] K. Gutiérrez-Luna, I. Astiasarán, D. Ansorena, *Crit. Rev. Food Sci. Nutr.* 62 (2022) 3768–3781. <https://doi.org/10.1080/10408398.2020.1869693>.
- [5] G. Yazar, C. M. Rosell, *Crit. Rev. Food Sci. Nutr.* (2022) 1–24. <https://doi.org/10.1080/10408398.2022.2048353>.
- [6] D. Kalinga, V. K. Mishra, *J. Food Process. Preserv.* 33 (2009) 384–400. <https://doi.org/10.1111/j.1745-4549.2008.00260.x>.
- [7] S. Martínez-Cervera, A. Salvador, M. Muguerza, L. Moulay, S.M. Fiszman, *LWT-Food Sci. Technol.* 44 (2011) 729–736. <https://doi.org/10.1016/j.lwt.2010.06.035>.
- [8] J.Y. Jung, S.A. Kim, H.J. Chung, *J. Korean Soc. Food Sci. Nutr.* 34 (2005) 694–699. <https://doi.org/10.3746/jkfn.2005.34.5.694>.
- [9] J. Parkash, D. P Sharma, S. Yadav, *Pharma Innov. J.* 10 (2021) 13–17. <https://www.thepharmajournal.com/archives/2021/vol10issue6S/PartA/S-10-5-103-225.pdf>.
- [10] K. Warner, G.E. Inglett, *Cereal Foods World* 42 (1997) 821–825. <https://pubag.nal.usda.gov/download/25056/pdf>.
- [11] G.E. Inglett, C.J. Carriere, S. Maneepun, P. Tungtrakul, *Int. J. Food Sci. Technol.* 39 (2003) 1–10. <https://doi.org/10.1111/j.1365-2621.2004.00739.x>.
- [12] N. Milićević, M. Sakač, M. Hadnađev, D. Škrobot, B. Šarić, T. Hadnađev Dapčević T.P. Jovanov, L. Pezo, *J. Cereal Sci.* 95 (2020) e103056. <https://doi.org/10.1016/j.jcs.2020.103056>.
- [13] J.T. Cole, G.C. Fahey Jr, N.R. Merchen, A.R. Patil, S.M. Murray, H.S. Hussein, J.L. Brent Jr, *J. Anim. Sci.* 77 (1999) 917–924. <https://doi.org/10.2527/1999.774917x>.
- [14] L. Yang, Y. Zhao, J. Huang, H. Zhang, Q. Lin, L. Han, J. Liu, J. Wang, H. Liu, *J. Food Sci. Technol.* 57 (2020) 152–162. <https://doi.org/10.1007/s13197-019-04041-9>.
- [15] X. Castañón, A. Argai, A. Lopez-Malo, *Food Sci. Technol. Int.* 5 (1999) 51–58. <https://doi.org/10.1177/108201329900500105>.
- [16] J.A. Rufián-Henares, C.D. Andrade, F.J. Morales, *J. AOAC Int.* 89 (2006) 161–165. <https://doi.org/10.1093/jaoac/89.1.161>.
- [17] C. Petisca, A.R. Henriques, T. Pérez-Palacios, O. Pinho, I.M.P.L.V.O. Ferreira, *J. Food Compos. Anal.* 33 (2014) 20–25. <https://doi.org/10.1016/j.jfca.2013.10.004>.
- [18] A.A. Ariffin, H.M. Ghazali, P. Kavousi, *Food Chem.* 154 (2014) 102–107. <https://doi.org/10.1016/j.foodchem.2013.12.082>.
- [19] D. Tomasini, M.R. Sampaio, S.S. Caldas, J.G. Buffon, F.A. Duarte, E.G. Primel, *Talanta* 99 (2012) 380–386. <https://doi.org/10.1016/j.talanta.2012.05.068>.
- [20] ISO 8586:2012, *Sensory Analysis - General guidelines for the selection, training and monitoring of selected assessors and expert sensory assessors*, International Organization for Standardization, Geneva, Switzerland, 2012. <https://www.iso.org/standard/45352.html>.
- [21] AOAC, *Official Methods of Analysis* (17th ed.), AOAC International, Maryland, USA, 2000.
- [22] ICC Standard No. 123/1, *International Association for Cereal Science and Technology*, ICC, Vienna, Austria, 1994.
- [23] N. Nedeljković, M. Hadnađev, T. Hadnađev Dapčević, B. Šarić, L. Pezo, M. Sakač, B. Pajin, *LWT-Food Sci. Technol.* 86 (2017) 377–384. <https://doi.org/10.1016/j.lwt.2017.08.004>.
- [24] C. Villemejeane, P. Roussel, S. Berland, P. Aymard, C. Michon, *J. Cereal Sci.* 57 (2013) 551–559. <https://doi.org/10.1016/j.jcs.2013.03.005>.
- [25] M.L. Sudha, A.K. Srivastava, R. Vetrmani, K. Leelavathi, *J. Food Eng.* 80 (2007) 922–930. <https://doi.org/10.1016/j.jfoodeng.2006.08.006>.
- [26] B. Pareyt, F. Talhaoui, G. Kerckhofs, K. Brijs, H. Goesaert, M. Wevers, J.A. Delcour, *J. Food Eng.* 90 (2009) 400–408. <https://doi.org/10.1016/j.jfoodeng.2008.07.010>.
- [27] C. Sanchez, C.F. Klopfenstein, C.E. Walker, *Cereal Chem.* 72 (1995) 25–29. https://www.cerealsgrains.org/publications/cc/backissues/1995/Documents/72_25.pdf.
- [28] H. Mamat, S.E. Hill, *J. Food Sci. Technol.* 51 (2014) 1998–2005. <https://doi.org/10.1007/s13197-012-0708-x>.
- [29] B. Filipčev, N. Nedeljković, O. Šimurina, M. Sakač, M. Pestorić, D. Jambrec, B. Šarić, P. Jovanov, *Hem Ind.* 71 (2017) 61–67. <https://doi.org/10.2298/HEMIND150922018F>.
- [30] S. Lee, G.E. Inglett, *Int. J. Food Sci. Technol.* 41 (2006) 553–559. <https://doi.org/10.1111/j.1365-2621.2005.01105.x>.
- [31] L. Laguna, C. Primo-Martín, P. Varela, A. Salvador, T. Sanz, *LWT-Food Sci. Technol.* 56 (2014) 494–501.

- <https://doi.org/10.1016/j.lwt.2013.12.025>.
- [32] S. Chevallier, P. Colonna, G. Della Valle, D. Lourdin, J. Cereal Sci. 31 (2000) 241–52. <https://doi.org/10.1006/jcrs.2000.0308>.
- [33] K.B. Arun, F. Persia, P.S. Aswathy, J. Chandran, M.S. Sajeev, P. Jayamurthy, P. Nisha, J. Food Sci. Technol. 52 (2015) 6355–6364. <https://doi.org/10.1007/s13197-015-1727-1>.
- [34] E. Capuano, A. Ferrigno, I. Acampa, A. Serpen, Ö.Ç. Açar, V. Gökmen, V. Fogliano, Food Res. Int. 42 (2009) 1295–1302. <https://doi.org/10.1016/j.foodres.2009.03.018>.
- [35] D. Jaros, H. Rohm, J. Food Qual. 24 (2001) 79–86. <https://doi.org/10.1111/j.1745-4557.2001.tb00592.x>.
- [36] Regulation (EC) No 1924/2006 of the European Parliament and of the Council of 20 December 2006 on Nutrition and Health claims made on foods. OJ L 404, 9–25. Available from: <https://eur-lex.europa.eu/legal-content/en/ALL/?uri=CELEX%3A32006R1924>.
- [37] Food and Nutrition Board, Dietary Reference Intakes (DRIs): Recommended Intakes for Individuals, Elements, 2004. Available from: https://www.nal.usda.gov/sites/default/files/fnic_uploads/recommended_intakes_individuals.pdf.
- [38] S. Patel, J. Funct. Foods. 14 (2015) 255–269. <https://doi.org/10.1016/j.jff.2015.02.010>.
- [39] T. Thompson, M. Dennis, L.A. Higgins, A.R. Lee, M.K. Sharrett, J. Hum. Nutr. Diet. 18 (2005) 163–169. <https://doi.org/10.1111/j.1365-277X.2005.00607.x>.

NATAŠA MILIĆEVIĆ
MARIJANA SAKAČ
BOJANA ŠARIĆ
DUBRAVKA ŠKROBOT
BOJANA FILIPČEV
OLIVERA ŠIMURINA
PAVLE JOVANOVIĆ
MLADENKA PESTORIĆ
ALEKSANDAR MARIĆ

Naučni institut za prehrambene
tehnologije u Novom Sadu,
Univerzitet u Novom Sadu, Novi
Sad, Srbija

NAUČNI RAD

SOJINE MEKINJE KAO ZAMENJIVAČI MASTI U FORMULACIJI BEZGLUTENSKOG KEKSA: FIZIČKO-HEMIJSKA SVOJSTVA I SENZORSKI PROFIL

Sojine mekinje su korišćene za delimičnu zamenu masti (30%–50%) u formulaciji bezglutenskog keksa. Karakteristike testa, kao i fizička (dimenzija keksa i gubitak težine) i teksturna (tvrdoća i lomljivost) svojstva keksa, te parametri boje i senzorske svojstva, kao i nutritivni profil su određivani u svrhu karakterizacije punomasnog keksa i keksa sa smanjenim sadržajem masti. Na osnovu dobijenih rezultata, zaključeno je da smanjenje masti u formulaciji keksa na nivou od 30% rezultira neznatno promenjenim senzorskim svojstvima punomasnog keksa. Zamena masti korišćenjem sojinih mekinja na nivou od 30% rezultirala je dobijanjem bezglutenskog keksa sa smanjenim sadržajem masti, ali sa dodatom vrednošću u pogledu dijetnih vlakana i minerala. Dnevni unos keksa sa 30% zamene masti zadovoljava 11,87% i 18,04% preporučenog dnevnog unosa u ishrani (DRI) za dijetna vlakna, 26,50% DRI za kalcijum, 35,71% i 46,88% DRI za magnezijum i 65,43% i 83,61% DRI za mangan, za odrasle muškarce i žene, respektivno.

Ključne reči: bezglutenski keks, zamenjivači masti, sojine mekinje, fizičko-hemijska svojstva, senzorska analiza.

AMARÍLIS SEVERINO E
SOUZA¹
THIAGO CÉSAR DE SOUZA
PINTO²
ALFREDO MOISÉS SARKIS³
THIAGO FAGGION DE
PÁDUA¹
RODRIGO BÉTTEGA¹

¹Federal University of São
Carlos, Department of Chemical
Engineering, Drying Center of
Pastes, Suspensions, and
Seeds, São Carlos, SP, Brazil

²Mineral Development Center -
CDM/Vale, Santa Luzia, MG,
Brazil

³Instituto Tecnológico Vale - ITV,
Santa Luzia, MG, Brazil

SCIENTIFIC PAPER

UDC 622.785:66.047

ENERGY ANALYSIS OF THE CONVECTIVE DRYING OF IRON ORE FINES

Article Highlights

- Characterization of iron ore fines according to IMSBC code
- Handling and drying of wet agglomerates of iron ore fines in a fixed bed
- Each air condition was associated with an optimal solids load that minimized the SEC
- Drying at the identified optimal condition resulted in the highest energy efficiency

Abstract

Drying operations in iron ore processing plants have a particularly high energy demand due to the massive solid flow rates employed in this industry. A 3³ full-factorial design was applied to investigate the effects of air temperature, airflow velocity, and solids load on the drying time and the specific energy consumption (SEC) of the convective drying of iron ore fines in a fixed bed. The results demonstrated that each drying air condition was associated with an optimal solids load that minimized the SEC. A load of 73 g (bed height of about 0.8 cm) was identified and validated as the optimal condition in terms of energy consumption for the configuration with the highest air temperature (90 °C) and airflow velocity (4.5 m/s). This condition resulted in a drying time of 29.0 s and a corresponding SEC of 12.8 MJ/kg to reduce the moisture from 0.11 kg water/kg dry solids to a target of 0.05 kg water/kg dry solids. Identifying the optimum values for the process variables should assist in designing and operating energy-efficient convective dryers for iron ore fines.

Keywords: iron ore agglomerates, transportable moisture limit, energy consumption, drying efficiency, pellet feed.

An important step in the processing of iron ore is the removal of moisture. The grinding and separation processes of mineral species are usually carried out using wet routes, so there is a subsequent need to remove water from concentrates before sending the ore to direct reduction, pelletizing, or exportation [1–3]. Even after the dewatering processes, rain and poor conditions at the storage yards can increase the amount of water in the ore. These problems are detri-

mental for direct shipping ores because a high moisture level increases the freight cost and decreases the profit since the price of the sold ore is assessed on a dry basis. Another issue is that, before shipping, the iron ore must comply with the maximum moisture level established by the International Maritime Organization (IMO) for the safe transport of bulk materials in ships, known as the Transportable Moisture Limit (TML) [4,5].

Iron ore fines are classified as Group A cargo according to the IMSBC (International Maritime Solids Bulk Cargoes) Code [5]. It means that if the moisture content of this material is above the TML, the wet mineral cargo is subject to liquefaction. When ore liquefaction occurs in the cargo hold, the ship can progressively lose its stability due to cargo movement and may capsize and sink. Consequently, if the material does not comply with the TML value, the cargo is rejected, and the product remains in the storage yards,

Correspondence: A. Severino E Souza, Federal University of São Carlos, Department of Chemical Engineering, Drying Center of Pastes, Suspensions, and Seeds, São Carlos, SP, Brazil.

E-mail: amarilis.sev@gmail.com

Paper received: 8 February, 2022

Paper revised: 25 May, 2022

Paper accepted: 11 October, 2022

<https://doi.org/10.2298/CICEQ220208026S>

causing economic losses for the mining company and difficulties in handling procedures, affecting the entire production chain. Therefore, dewatering and drying systems are important for commercializing and transporting this ore.

The TML value can vary widely according to the characteristics of the ore. Moreira *et al.* [6] investigated the variation of TML for iron ore according to particle size distribution. They concluded that the addition of fine particles could increase the TML. Munro and Mohajerani [4] and Ferreira *et al.* [7] determined the TML for samples with various size distributions, iron contents, and mineralogical compositions. The results of these studies covered TML values from 8.00% to 16.80% and from 7.69% to 14.95%, respectively, representing considerable ranges in terms of moisture. Usually, when the mechanical removal of water from a specific variety of iron ore using hydrocyclones [8], thickeners [9], filters [10,11], and vacuum filters [12,13] is not sufficient to meet the TML standard, or when layout or process conditions do not permit installation of these systems, thermal drying becomes necessary.

Since thermal drying requires hot air, the process is expensive for ore processing plants in terms of fuel consumption, equipment, dust abatement, and greenhouse gas generation. On the other hand, convective drying is one of the industrial processes with the highest energy demand [14,15] because it provides the thermal energy necessary to vaporize moisture. Consequently, the energy required for drying massive amounts of ore under severe air velocity and temperature conditions is one of the main challenges for employing and maintaining convective drying in iron ore processing plants [16]. For example, a temperature of more than 1000 °C and an airflow of 4.6 t/h were used to dry an iron ore flow of 4.0 t/h at an initial moisture level of 19% (wet basis) [17]. Considering this commodity's relatively low unit price (US\$168 per dry metric ton of 62.5% Fe ore in 2021 [18]), the drying air conditions, and the process's scale, drying operations incur high costs for the mining industry. Therefore, studies that offer strategies for efficient energy use are of paramount interest to this sector [19].

Although drying processes represent a considerable challenge for the mining industry, the existing work in this area is scarce [19,20]. Considering iron ore drying, the literature focuses on pellets [21–25], while work regarding iron ore fines is rare. In drying iron ore fines, Namkung and Cho [26] determined some fluid dynamic aspects of a pneumatic dryer operating with iron ore particles with diameters ranging. For an initial moisture content of 6.95% (wet basis), it was observed that the degree of particle drying increased from 48.6% to 82.5% with an increase in the air temperature from 100 °C to 400 °C. Souza Pinto *et al.*

[27] investigated the characteristics and drying kinetics of iron ore pellet and sinter feed. This study showed that for a drying operation using a fixed bed with an air temperature of 400 °C, moisture removal decreased by around 60% when the operation involved the final drying stage (falling rate period). This result indicated potential energy savings and cost reductions for drying operations occurring within the initial drying period (constant rate). However, no further investigation was performed on the energy aspects of iron ore fines drying operations.

Knowledge about energy consumption is important for a better understanding of the drying processes. The thermal energy consumption of hot air drying operations in a fixed bed is related to the drying air conditions and the solids load. The few studies that have investigated the effect of the solids load on the specific energy consumption of drying operations [28,29] have reported that increasing the solids load resulted in lower energy consumption. Nevertheless, in these experimental studies, no analysis was performed to investigate if there was a limit to this trend. Since the further increase of the solids loads also leads to less energy being absorbed per unit mass, the evaporation rates can drop, and the drying time can rise to the point of increasing the energy consumption of the process. Therefore, additional studies are still required to investigate the behavior of the energy consumption of drying processes in fixed beds according to the solids load.

The objective of the present work was to analyze the drying kinetics and energy consumption for the convective drying of iron ore fines in a fixed bed. To this end, a 3³ full-factorial design and a statistical analysis using response surface methodology were employed to investigate the effects of the variables solids load, air temperature, and airflow velocity on the responses drying time and specific energy consumption. In addition, the energy performance was evaluated based on energy efficiency, drying efficiency, and specific energy consumption parameters. The aim was to identify operating conditions that could minimize the energy consumption of the drying process.

MATERIALS AND METHODS

Sample characterization and preparation

Dry iron ore samples from Carajás (Pará State, Brazil) were provided by Instituto Tecnológico Vale (ITV-MI). Chemical characterization was performed for a sample fused with lithium tetraborate using an X-ray fluorescence spectrometer (Zetium, Malvern Panalytical). Loss on ignition (LOI) determination was performed using a temperature of 1020 °C for 2 h. The

results obtained were 65.3% Fe, 0.74% SiO₂, 1.10% Al₂O₃, and 3.97% LOI.

The particle size was determined using a Malvern Mastersizer Microplus instrument (Micromeritics). Figure 1 presents the particle size distribution (ϕ - cumulative; $\Delta\phi$ - per fraction), showing D₁₀ and D₅₀ values of around 0.3 μ m and 40 μ m, respectively. The density of the iron ore was 4.2 g/cm³.

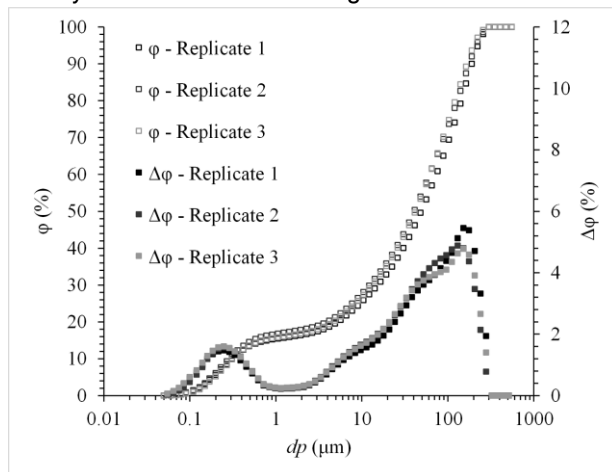


Figure 1. Cumulative particle size distribution of the iron ore fines.

The modal mineralogical composition of the sample was determined by reflected light microscopy (DM750P-Leica). The quantification of hematite minerals, goethite, quartz, silicate, and others, was performed by counting at least 500 grains per polished section. Results showed 72.45% of hematite and 25.28% of goethite. Quartz, silicate, and others were 1.32%, 0.19%, and 0.75%, respectively. Concerning the mineralogical composition (goethite content less than 35%) and the size distribution ($D_{10} \leq 1$ mm and $D_{50} \leq 10$ mm), the sample was classified as Iron Ore Fines according to the IMSBC Code (IMO, 2019), a Group A cargo susceptible to liquefaction if shipped at a moisture content above its TML.

Distilled water was added to portions of 200 g of dry ore until reaching the desired nominal moisture content of 0.11 kg water/kg dry solids (dry basis) to humidify the material [27]. The material was kept in closed plastic bags, at room temperature, for up to 12 h before the tests. Standard deviations for the initial moisture content determined by this method were approximately 0.3%. The dry and humidified ore can be seen in Figure 2. Before the drying assays, the sample of the wet material was extruded through a coarse mesh sieve to standardize the agglomerates that were formed. This procedure maintained the agglomerates with diameters less than 6 mm (sieve opening), and this procedure had no impact on the nominal moisture content of the sample. The formation of agglomerates is a feature of the humidified ore [27,30].

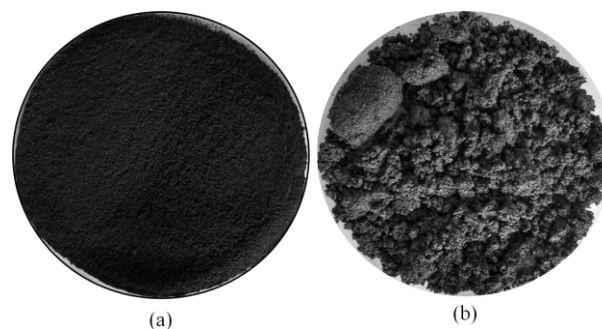


Figure 2. Photographs of the iron ore fines: (a) dry and (b) with a nominal moisture content of 0.11 kg water/kg dry solids, showing agglomeration of wet particles.

Experimental apparatus and procedure

Figure 3 shows the experimental apparatus used in this study. The equipment consisted of a blower with a controlled airflow, an electric heater, and a cylindrical glass drying chamber (7.2 cm inside diameter, 50 cm height). The temperature of the air entering the drying chamber was controlled to within ± 1 °C by a temperature controller and remained unchanged at the setpoint during each of the experimental drying assays. The superficial air velocity was measured at the center of the cylindrical drying chamber (Figure 3) using a hot wire anemometer (AK833, Akso) and was adjusted before each assay.

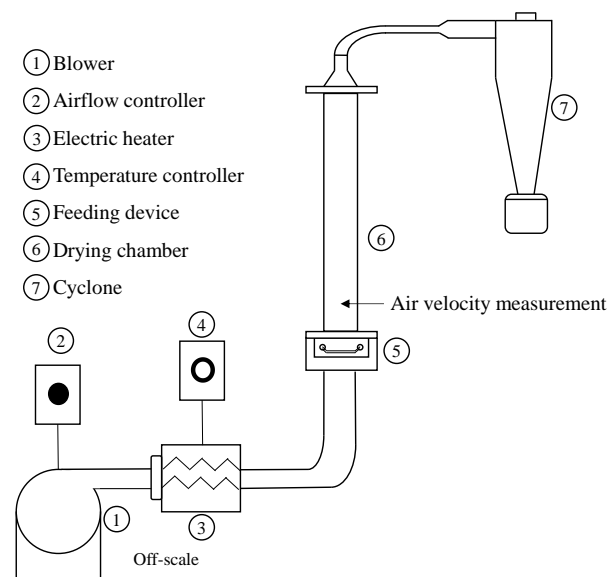


Figure 3. Diagram of experimental apparatus.

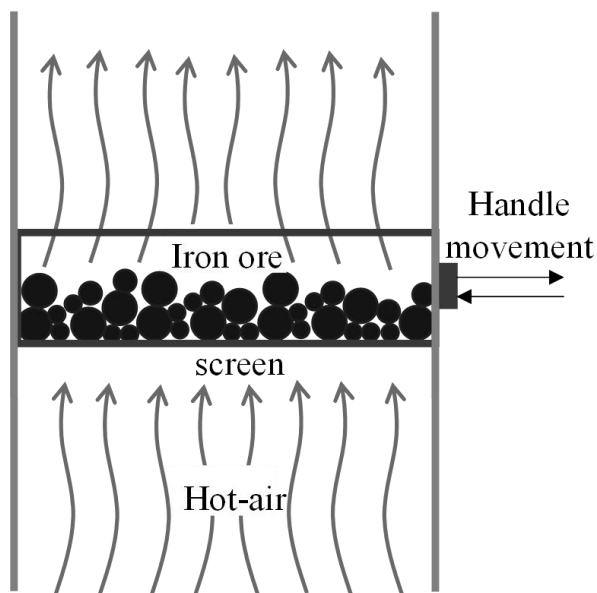
A cyclone was installed on the top of the drying chamber to collect entrained fine dust. However, humidification and consequent agglomeration of iron ore fines substantially reduced particle entraining at the analyzed airflow conditions. Therefore, the mass of dust collected by the cyclone was very low (less than 1.5% of the feed), and this portion of the material was neglected when analyzing the drying kinetics.

The feeding device (Figure 4a) consisted of a drawer-like system where a container could be moved

across a fixed base. For loading, the container was entirely removed from the drying chamber, filled with solids, and then inserted back into the system, sealing the chamber and preventing air leakage. The base of the container had a screen that supported the solids and allowed contact of the drying air with the sample. The advantage of the device was the feeding and collecting of the solid agglomerates from the chamber without needing to turn off the air supply, as well as for easy removal and weighing of the whole sample at the end of the drying time. The loaded solids kept a fixed bed configuration during drying (Figure 4b). In order to avoid breakage of the ore agglomerates and consequent dragging of fine particulate material, the fluidized bed condition was not used.



(a)



(b)

Figure 4. Feeding apparatus (a) photograph, showing attachment of the drawer to the drying chamber, and (b) scheme of air contact with the sample in the drying chamber.

The experimental procedure consisted of setting the operating conditions and stabilizing the system

(with the airflow and temperature reaching a steady state), after which the drying chamber was loaded with a mass of wet material at 0.11 kg water/kg dry solid, using the feeding device. At the end of each drying time interval (0 s, 30 s, 60 s, 120 s, 240 s, 360 s, 480 s), the sample was removed from the equipment, weighed, and dried in an oven at a constant temperature of 105 °C. After 24 h, the weight of the sample was measured again to obtain its moisture content [31]. This procedure was performed to obtain the behavior of the moisture content with time.

The process kinetics was described using the dimensionless moisture content:

$$X^*(t) = \frac{X_t - X_{eq}}{X_i - X_{eq}} \quad (1)$$

where X_t is the average moisture content at time t , X_i is the initial moisture content, and X_{eq} is the moisture content at the dynamic equilibrium condition, all on a dry basis. Drying experiments were performed until reaching X_{eq} , which was about 0.003 kg water/kg dry solid.

The temperature of the solids (T_s) was monitored during the drying assays using an infrared thermometer (UT300A, UNI-Trend) with an accuracy of ± 2 °C. After removing the sample from the equipment at the end of the drying time, the thermometer was pointed toward the surface of the ore at a distance of about 1 cm. Three temperature readings were performed, and the average value for T_s was employed in the energy analysis to estimate the energy used to heat the solids.

Energy analysis

The usual parameters adopted in the literature were estimated to evaluate the dryer performance [32–34], calculating the energy and drying efficiencies using instantaneous non-cumulative indexes and the specific energy consumption (the total amount of energy necessary to evaporate a unit mass of water). The advantage of using specific energy consumption is that it is an understandable and straightforward measure that considers how efficiently energy is used in the drying process. In addition, this approach has been reported in the literature [32,33] for quantification of the variation of the energy used according to the moisture content of the material.

The energy required to heat the material (Q_m) was calculated using the following equation:

$$Q_m = m_{ws} c_{ps} (T_{s,t} - T_{s,i}) \quad (2)$$

where m_{ws} is the mass of wet ore, c_{ps} is the specific heat of iron ore, which was considered constant, equal to 620 J kg⁻¹ K⁻¹ [35], and $T_{s,t}$ and $T_{s,i}$ are the mean temperature of the iron ore at time t and the initial time, respectively.

The energy required to evaporate the water present in the sample (Q_w) was estimated based on the mass of bone-dry ore (m_{ds}) and the latent heat of free water vaporization (ΔH_s):

$$Q_w = \Delta H_s m_{ds} (X_i - X_f) \quad (3)$$

The latent heat of free water vaporization was obtained using Eq. 4 [36]:

$$\Delta H_s = 3168 - 2.4364 T_s \quad (K) \quad (4)$$

The thermal energy supplied to the system (Q) was calculated as follows:

$$Q = \dot{m} c_p (T_f - T_a) \quad (5)$$

where, \dot{m} is the mass flow of air, c_p is the specific heat of air, T_f is the temperature of the drying air, and T_a is the ambient temperature, equal to 25 °C.

The parameters used to analyze the energy performance of the convective dryer were energy efficiency (EE), drying efficiency (DE), and specific energy consumption (SEC) [37]. These parameters were calculated as follows:

$$EE = \frac{Q_w}{Q t} \quad (6)$$

$$DE = \frac{Q_w + Q_m}{Q t} \quad (7)$$

$$SEC = \frac{Q t}{m_{ds} (X_i - X_f)} \quad (8)$$

The heat absorbed by the feeding device and the drying chamber during the assays is process inefficiency, which is accounted for in the energy performance parameters.

Experimental design and statistical analysis

The experimental design technique has been employed to analyze the energy demands and optimize drying process variables for different materials [29,38–40]. This method enables investigation of the effects of the independent variables involved in the process and their interactions, identifying the operating conditions that favor energy savings.

A 3³ full-factorial design (face-centered composite design) was performed to determine the effect of external conditions on the convective drying of the iron ore fines. The design evaluated the effects of the variables solids load (m_p), air temperature (T_f), and airflow velocity (u_f) on the responses drying time to a 0.05 kg water/kg dry solids moisture content (t_d) and the specific energy consumption required for the sample to attain this moisture value (E_s). A final moisture level of 0.05 kg water/kg dry solids for both t_d and E_s was defined to meet the minimum moisture content desired for iron ore since lower values can lead to high dust

generation, product loss, and difficulties in handling the material [41]. Furthermore, this value is above the critical humidity found in tests for other dryers [27] and was used as a reference for drying to occur mainly within the constant rate period. This value is also below the TML usually found for iron ore and hence meets the moisture content required for shipping operations [4,7].

The experimental data of the dimensionless moisture content over time were fitted using a kinetic model (Eq. 9) to obtain the value of t_d [27,42]. The drying time to 0.05 kg water/kg dry solid was then estimated using the equation of the fit. A similar method was employed by Silva *et al.* [43] to estimate the drying time necessary for the sample to achieve a specific moisture level. Finally, the E_s value was calculated for each experiment, considering the corresponding value obtained for t_d . This equation showed good agreement with the fitted experimental data, with determination coefficients (R^2) above 0.98. It is important to mention that Eq. (9) was not used to represent the drying kinetics physically but only to obtain a more accurate prediction of t_d according to the experimental results.

$$X^*(t) = A \exp(-kt^n) \quad (9)$$

A 3³ full-factorial design was used, with three replicates at the central point, considering three solids loads (26 g, 58 g, and 90 g, corresponding to bed heights of about 0.3 cm, 0.6 cm, and 0.9 cm, respectively), three air temperatures (50 °C, 70 °C, and 90 °C), and three airflow velocities (2.5 m/s, 3.5 m/s, and 4.5 m/s), resulting in 29 assays. The ranges of the variables were chosen according to the operational limits of the equipment, as well as to avoid particles falling through the solids support screen or being entrained away from the drying chamber.

The results were treated using the response surface technique, employing Statistica 7.0 software for the statistical analysis and mathematical modeling. Multiple regression of the data, using a significance level of 0.05, was used to quantify the effects of the variables, as well as their interactions and quadratic contributions. The independent variables were treated in their coded forms, as given by Eqs. (10), (11), and (12).

$$x_1 = \frac{m_p - 58}{32} \quad (10)$$

$$x_2 = \frac{T_f - 70}{20} \quad (11)$$

$$x_3 = u - 3.5 \quad (12)$$

An analysis of variance (ANOVA) was applied to evaluate the quality of the model fitted to the data.

F -statistic (ratio between two mean squares) was used to compare the variances in the hypothesis test [44]. The significance level was 0.05 for each hypothesis test.

The operating conditions that provided the lowest energy consumption and shorter drying times were subjected to an energy efficiency analysis.

RESULTS AND DISCUSSION

Drying kinetics experiments

The effects of air temperature, airflow velocity, and solids load on the drying process of iron ore fines are shown in Figure 5. The results for the other conditions presented the same behavior. As expected, the drying time decreased with the airflow velocity and temperature increase. An increase in the air temperature from 50 °C to 90 °C resulted in shorter residence times to reach the same moisture content due to the enhancement of the thermal capacity of the air and higher mass transfer rates. The initial period of the process was characterized by a substantial reduction of the moisture content, corresponding to the removal of free water from the material. On the other hand, the drying time increased when more solids were fed into the system. Souza Pinto *et al.* [27] reported a similar behavior for the effect of air temperature on the drying of iron ore with particle diameters less than 500 μm in an oven.

A thorough analysis of the effects of air temperature, airflow velocity, and solids load on drying time and specific energy consumption was performed by statistical analysis of the factorial design results.

Statistical analysis and response surface plots

Table 1 shows the solids loads (m_p , g) and the operational drying conditions, considering the air temperature (T_f , °C) and the airflow velocity (u_f , m/s), together with the corresponding responses for the drying time and the specific energy consumption, for each assay of the experimental design. The drying time and the SEC corresponded to the period required for the sample to achieve a moisture value of 0.05 kg water/kg dry solids. For example, when drying a solids load of 26 g at 50 °C and 2.5 m/s, the time required to decrease the moisture of the sample from its initial moisture content to a moisture content of 0.05 kg water/kg dry solids (t_d) was 79.2 s and the SEC was 18.8 MJ/kg.

The regressions resulted in residuals that were randomly distributed around the mean.

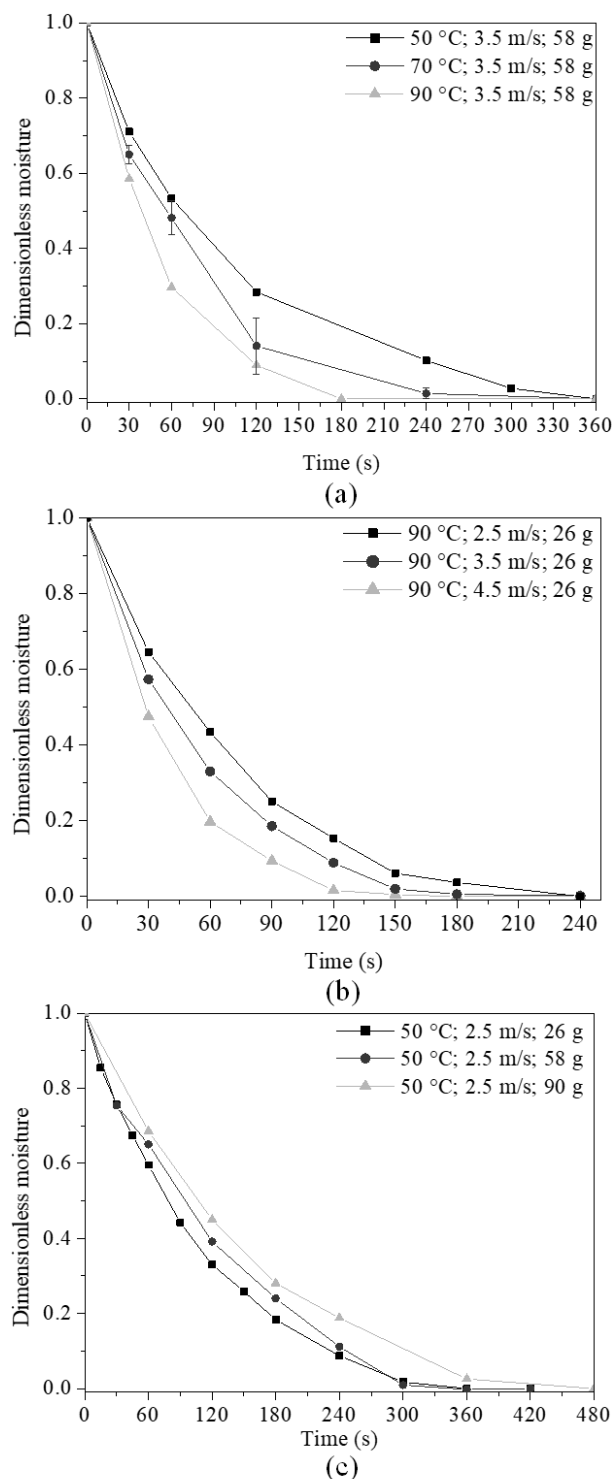


Figure 5. Drying kinetics curves for the convective drying of iron ore fines, showing the dimensionless moisture as a function of time for various experimental conditions: (a) comparing different inlet air temperatures, (b) airflow velocities, and (c) solids loads.

Effect of the independent variables on the drying time

The responses for the t_d (Table 1) ranged between 27.9 s and 105.6 s. Multiple regression of the experimental data resulted in the polynomial fit described by Eq. 13 for the drying time, with the

Table 1. Factorial design (3^3): settings and responses for the drying time and the specific energy consumption to a moisture content of 0.05 kg water/kg dry solids.

Independent variables			Responses	
m_p [g] (x_1)	T_r [°C] (x_2)	u [m/s] (x_3)	t_d (s)	E_s (MJ/kg)
26(-1)	50(-1)	2.5(-1)	79.2	18.8
26(-1)	70 (0)	2.5(-1)	54.5	21.9
26(-1)	90(+1)	2.5(-1)	45.4	24.9
26(-1)	50(-1)	3.5 (0)	59.0	19.7
26(-1)	70 (0)	3.5 (0)	42.2	23.8
26(-1)	90(+1)	3.5 (0)	34.4	26.4
26(-1)	50(-1)	4.5(+1)	51.7	22.1
26(-1)	70 (0)	4.5(+1)	29.7	21.5
26(-1)	90(+1)	4.5(+1)	27.9	27.5
58(0)	50(-1)	2.5(-1)	87.9	9.4
58(0)	70 (0)	2.5(-1)	55.1	9.9
58(0)	90(+1)	2.5(-1)	43.9	10.8
58(0)	50(-1)	3.5 (0)	64.2	9.6
58(0)	70 (0)	3.5 (0)	56.0	14.1
58(0)	70 (0)	3.5 (0)	47.6	12.0
58(0)	70 (0)	3.5 (0)	51.1	12.9
58(0)	90(+1)	3.5 (0)	29.7	10.2
58(0)	50(-1)	4.5(+1)	54.7	10.5
58(0)	70 (0)	4.5(+1)	37.7	12.2
58(0)	90(+1)	4.5(+1)	30.3	13.4
90(+1)	50(-1)	2.5(-1)	105.6	11.3
90(+1)	70 (0)	2.5(-1)	66.1	11.9
90(+1)	90(+1)	2.5(-1)	47.3	11.6
90(+1)	50(-1)	3.5 (0)	89.0	13.3
90(+1)	70 (0)	3.5 (0)	48.5	12.2
90(+1)	90(+1)	3.5 (0)	41.3	14.2
90(+1)	50(-1)	4.5(+1)	75.5	14.5
90(+1)	70 (0)	4.5(+1)	50.5	16.4
90(+1)	90(+1)	4.5(+1)	33.0	14.6

variables in coded form. Only the terms influencing the response within a 95% confidence interval are presented.

$$t_d = 48.9942 + 7.3695x_1 - 18.5336x_2 + 6.5715x_2^2 - 10.7689x_3 - 5.5254x_1x_2 + 3.7907x_2x_3 \quad (13)$$

The determination coefficient (R^2) for this empirical model was 0.958, indicating that Eq. 13 could explain 95.8% of the variability of the t_d responses. Statistical evaluation of the model obtained for t_d (Eq. 13) was performed using analysis of variance (ANOVA), as shown in Table 2. According to the literature [44], the calculated value of the F distribution for the regression should be about 3 times higher than the tabulated value for the model to be considered statistically significant. This requirement was fulfilled since $F_{\text{calc}}(\text{regression/residual}) = 33.1 > F_{\text{tab}}(\text{regression/residual})$. Furthermore, the model showed no lack of fit ($F_{\text{calc}}(\text{lack of fit/pure error}) < F_{\text{tab}}(\text{lack of fit/pure error})$). Therefore, the independent variables were sufficient to describe the

behavior of t_d in the range studied.

There were significant effects of all the independent variables in isolated form and the quadratic term corresponding to air temperature. The independent variable T_r (x_2 , coded) showed the greatest effect on t_d . In addition, interaction effects were identified between the variables solids load and air temperature and air temperature and air velocity. The significant interaction effects observed among all three variables highlighted the importance of evaluating them simultaneously when analyzing the iron ore drying time.

The response surfaces (Figure 6) showed that t_d decreased when lower solids loads, higher air temperatures, and higher airflow velocities were employed. These effects were physically coherent regarding the drying phenomena for the constant drying rate period.

Figure 6 could be used to investigate the interaction effects between the independent variables. Regarding the interaction of m_p and T_r , an increase of 42% in the drying time was calculated between the lower and upper level of m_p for the lowest air temperature. On the other hand, when the highest air temperature was used, a t_d increase of only 10% was observed, considering the same m_p levels. Therefore, the magnitude of the influence of the air temperature on t_d depended on the solids load in the bed. This behavior could be explained by considering the relation between the air temperature and the quantity of heat supplied to the sample per unit mass. When lower temperatures were used, an increase in solids load caused a decrease in heat per unit mass supplied to the sample. Consequently, lower drying rates and longer drying times occurred because less energy per unit mass was available to supply the latent heat required to evaporate the water. However, heat transfer was sufficient for higher temperatures to ensure high drying rates for the solids loads evaluated. Therefore, at this condition, the increase of the solids load did not substantially affect the supply of heat per unit mass to the sample, so the drying time was less pronounced.

Although the conditions that employed higher air temperatures and airflow velocities demanded more

Table 2. ANOVA for drying time for a final moisture content of 0.05 kg water/kg dry solid (t_d).

Source of variation	Sum of squares	Degrees of freedom	Mean of square	F_{calc}
Regression	10081.56	6	1680.26	84.44
Residual	437.76	22	19.90	
Lack of fit	402.34	20	20.12	1.14
Pure error	35.41	2	17.70	
Total	10519.32	28	375.69	

$$F_{\text{tab}}(\text{regression/residual}) = 2.55; F_{\text{tab}}(\text{lack of fit/pure error}) = 19.44$$

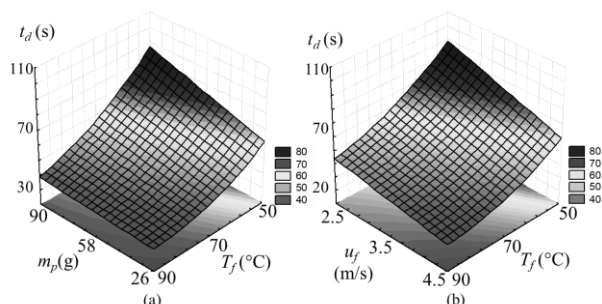


Figure 6. Response surfaces showing the drying time to a moisture content of 0.05 kg water/kg dry solid (t_d) as a function of the variables (a) air temperature and solids load and (b) air velocity and air temperature. In each case, the remaining variable was kept at the center level.

energy per unit of time to heat and blow the drying air, the value of t_d for these settings was substantially smaller. Therefore, the following analysis evaluated the SEC to understand the behaviour of the energy demand according to the process variables.

Effect of independent variables on energy consumption

E_s responses ranged between 9.4 MJ/kg and 27.5 MJ/kg (Table 1). Eq. (14) presents the multiple

regression of the experimental data for E_s , disregarding the effects that were not statistically significant. A determination coefficient (R^2) of 0.959 was calculated for the polynomial quadratic model. Statistical evaluation of the model was performed using analysis of variance (ANOVA), as shown in Table 3. The model could be considered statistically significant since $F_{\text{calc}}(\text{regression/residual}) = 40.9 F_{\text{tab}}(\text{regression/residual})$. Furthermore, the model showed no lack of fit ($F_{\text{calc}}(\text{lack of fit/pure error}) < F_{\text{tab}}(\text{lack of fit/pure error})$).

$$E_s = 11373.77 - 4815.89x_1 + 6779.86x_1^2 + 1354.58x_2 + 1239.56x_3 - 1339.24x_1x_2 \quad (14)$$

There were significant effects of all the variables in isolated form and the presence of a quadratic term for the solids load. There was also a significant interaction between the solids load and the air temperature. For the range of operating conditions evaluated, the independent variable m_p (x_1 , coded) had the greatest influence on E_s , followed by air temperature and air velocity. Brito *et al.* [33] also found that the specific energy consumption was significantly affected by air temperature and solids load for convective drying of sorghum seeds.

Table 3. ANOVA for specific energy consumption for final moisture of 0.05 (E_s).

Source of variation	Sum of squares	Degrees of freedom	Mean of square	F_{calc}
Regression	815489765	5	163097953	108.035
Residual	34722496	23	1509673.7	
Lack of fit	32462494	21	1545833	1.36799
Pure error	2260002	2	1130001	
Total	850212261	28	30364724	

$$F_{\text{tab}}(\text{regression/residual}) = 2.64; F_{\text{tab}}(\text{lackoffit/pureerror}) = 19.45$$

Although the processes with high values of T_f and u_f consumed more energy, the drying time was substantially shorter under these conditions. For example, maintaining the higher load of solids and changing the temperature and air velocity levels from their lower to upper limits resulted in an approximately 69% reduction in the drying time and a 29% increase in E_s . Although the higher energy consumption is generally undesirable, this additional energy cost could be inevitable depending on the process demands or conditions (such as the solids' residence time in the equipment).

The response surfaces for E_s (Figure 7) showed that the energy consumption increased when higher air temperatures and airflow velocities were used. The quadratic behavior of the E_s response concerning the solids load indicated a point of minimum energy consumption at a specific m_p within the ranges of the variables analyzed. The energy consumption decreased as the solids load increased. This behavior was consistent because the energy consumption was inversely proportional to the solids load (Eq. 8).

However, there was a limit to this trend since a further increase of the solids load led to less heat being absorbed per unit mass. Furthermore, a higher solids load implied a higher solids bed height, which increased the temperature and moisture gradients between the layers of agglomerates located at the bottom and the top of the sample. Consequently, the material heated up more slowly, and the evaporation rate decreased, leading to increased drying time and energy consumption. For these reasons, the E_s values declined to a minimum as m_p increased and then went back up. Therefore, a compromise between the solids load and the process conditions was required to minimize the energy consumption of the iron ore convective drying process.

Experimental optimization

An energy optimization analysis was performed, considering the drying air conditions that provided the shortest drying time within the ranges of the studied variables ($T_f = 90$ °C; $u_f = 4.5$ m/s). For these settings, the corresponding solids load value that minimized the

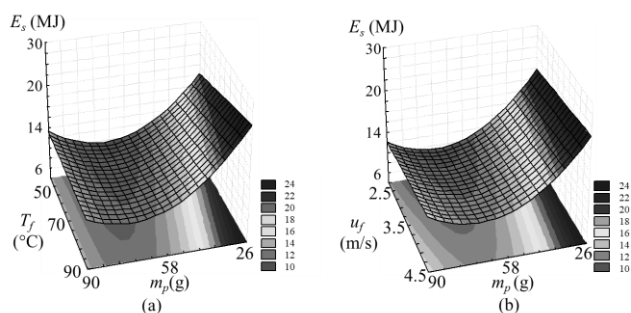


Figure 7. Response surfaces showing the specific energy consumption (E_s) as a function of the variables (a) air temperature and solids load and (b) air velocity and solids load, considering a final moisture content of 0.05 kg water/kg dry solid. In each case, the remaining variable was kept at the center level.

energy consumption was estimated using the regression equation for E_s (Eq. 14). As a result, a value of m_p of approximately 73 g (bed height of about 0.8 cm) was obtained, with estimated values of t_d (Eq. 13) and E_s (Eq. 14) of 30.9 s and 11.8 MJ/kg, respectively. New drying assays were performed in triplicate for this m_p value to validate the values predicted from the regression equations and determine the experimental results for t_d and E_s . As a result, a t_d value of 29.0 ± 0.6 s was obtained, with E_s of 12.8 ± 0.3 MJ/kg, the lowest E_s observed for these air conditions (T_f and u_f). Furthermore, deviations of 6.1% and 8.6% were calculated between the values estimated by Eqs. (13) and (14) and the experimental t_d and E_s results, respectively. Therefore, the assays performed under the optimal conditions confirmed the models' predictions for the evaluated experimental region within a significance level of 0.05.

Energy analysis

Figure 8 shows the curves for energy efficiency (filled symbols) and drying efficiency (open symbols), according to drying time, for different solids loads at a given air temperature and velocity. For all the conditions, the drying efficiency was higher than the energy efficiency because part of the sensible heat was used to heat the material [14]. However, the curves showed a steady decrease in the drying efficiency with time, up to approximately 100 s–120 s, after which the decrease was less pronounced. It could be explained by the fact that the removal of the remaining water in the final stages became increasingly difficult due to the lower gradients of water concentration and temperature between the drying air and the solids. Furthermore, the moisture content became close to equilibrium, and the process was limited by internal mass transfer mechanisms [14]. Given the moderate removal of moisture that is desired for iron ore fines (a final product moisture content of 0.05 kg water/kg dry solid was

adopted here), this result provides further evidence that operation within the drying period limited by external moisture diffusion could provide substantial energy savings for the drying process [27].

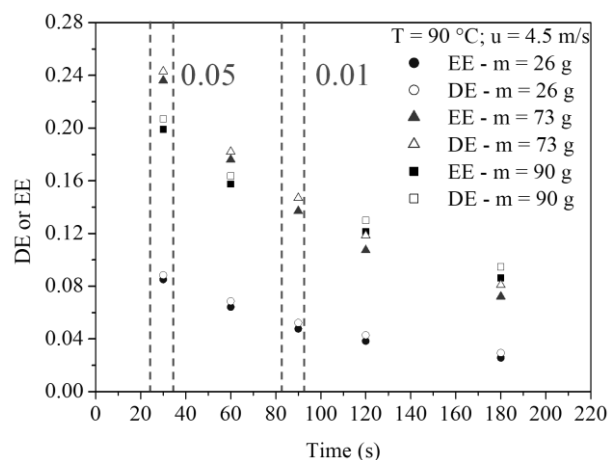


Figure 8. Drying and energy efficiencies for different solids loads as a function of time. The dashed lines indicate the approximate time intervals in which all the samples reached humidity values of 0.05 kg water/kg dry solid and 0.01 kg water/kg dry solid during drying.

The condition with the lowest mass showed the minimum DE and EE values. In convective drying processes, the attainment of high efficiency is hindered by the high amount of unsaturated air leaving the dryer, as well as by the short residence time of the air. Based on Eq. 6 and Eq. 7, increasing the quantity of water evaporated will increase the energy and drying efficiencies. Since the thermal energy supplied to the dryer was the same for all three conditions, the configurations with higher loads allowed higher saturation of the drying air, consequently increasing energy efficiency. On the other hand, the higher the solids load, the lower the quantity of heat transferred per unit mass of the sample, so the drying rate started to decrease when an excess of solids was fed to the system. Therefore, the mass of 73 g (bed height of about 0.8 cm) estimated by the response surface method represented the optimum value among the conditions analyzed.

The approach presented in this energy analysis provides a base for further investigation on the design of iron ore dryers, for example, when sizing conveyor dryers considering airflow conditions, product retention time, and bed height.

CONCLUSION

Statistical analysis of the drying results demonstrated that air temperature, airflow velocity, and solids load significantly affected the drying time and the specific energy consumption to a moisture content of

0.05 kg water/kg dry solid. The response surface method showed that a specific load of solids for each air condition could minimize the energy consumption for an iron ore drying process on a fixed bed. This finding means that a successive increase in the solids load decreases the energy consumption of the drying process only to a certain degree, after which the energy consumption rises. According to the optimization scheme of the experiments, when the highest values of air temperature ($T_f = 90$ °C) and air velocity ($u_f = 4.5$ m/s) were employed, the lowest energy consumption was obtained for a solids load of 73 g.

The results presented in this work show that efficient use of energy in drying operations of iron ore fines in fixed beds requires a compromise between the solids load, air temperature, and airflow velocity. Therefore, the approach presented here for identifying the optimum values of these variables should assist in designing and operating energy-efficient convective dryers for iron ore fines.

ACKNOWLEDGEMENT

This study was financed in part by the Coordenação de Aperfeiçoamento de Pessoal de Nível Superior - Brasil (CAPES) - Finance Code 001. In addition, this work was supported by CNPq- Brazil under Grant [142102/2019-9]; and Vale S.A. - Brazil.

NOTATION

c_p	Specific heat of air, $\text{kJ kg}^{-1} \text{K}^{-1}$
c_{ps}	Specific heat of solids, $\text{kJ kg}^{-1} \text{K}^{-1}$
DE	Drying efficiency
EE	Energy efficiency
ΔH_s	Latent heat of vaporization of hematite, kJ kg^{-1}
\dot{m}	Mass flow rate of air, kg s^{-1}
m_{ds}	Mass of dry solids, kg
m_p	Load of solids, g
m_{ws}	Mass of wet solids, kg
Q	Thermal energy supplied, kJ s^{-1}
Q_m	Energy required to heat the material, kJ
Q_w	Energy required to evaporate the water, kJ
E_s	Specific energy consumption for final moisture of 0.05 (dry basis), MJ kg^{-1}
t	Time, s
t_d	Drying time for a final moisture content of 0.05 (dry basis), s
T_a	Ambient temperature, °C
T_f	Drying air temperature, °C
u_f	Airflow velocity, m/s
x_1	Coded form of variable m_p
x_2	Coded form of variable T_f
x_3	Coded form of variable u_f
X	Dimensionless moisture
\bar{X}	Mean moisture in dry basis, kg kg^{-1}
X_i	Initial moisture in dry basis, kg kg^{-1}
X_{eq}	Moisture at dynamic equilibrium in dry basis, kg kg^{-1}

REFERENCES

- [1] F.P. Van Der Meer, Miner. Eng. 73 (2015) 21–30. <https://doi.org/10.1016/j.mineng.2014.12.018>.
- [2] A. Abazarpoor, M. Halali, R. Hejazi, M. Saghaeian, Miner. Process. Extr. Metall. 127 (2018) 40–48. <https://doi.org/10.1080/03719553.2017.1284414>.
- [3] H.J. Haselhuhn, S.K. Kawatra, Miner. Process. Extr. Metall. Rev. 36 (2015) 370–376. <https://doi.org/10.1080/08827508.2015.1004401>.
- [4] M.C. Munro, A. Mohajerani, Mar. Struct. 40 (2015) 193–224. <https://doi.org/10.1016/j.marstruc.2014.11.004>.
- [5] International Maritime Organization (IMO), Amendments (05-19) to the International Maritime Solid Bulk Cargoes (IMSBC) Code (on 1 January 2021) (MSC101/24Add.3), London, (2019).
- [6] D.D.C. Moreira, C.A.S. dos Santos, A.L.A. Mesquita, D.C. Moreira, Powder Technol. 373 (2020) 301–309. <https://doi.org/10.1016/j.powtec.2020.06.052>.
- [7] R.F. Ferreira, T.M. Pereira, R.M.F. Lima, Powder Technol. 345 (2019) 329–337. <https://doi.org/10.1016/j.powtec.2019.01.024>.
- [8] S.P. Suthers, V. Nunna, A. Tripathi, J. Douglas, S. Hapugoda, Trans. Inst. Min. Metall., Sect. C 123 (2014) 212–227. <https://doi.org/10.1179/1743285514Y.0000000067>.
- [9] A.S. Patra, D. Makhija, A.K. Mukherjee, R. Tiwari, C.R. Sahoo, B.D. Mohanty, Powder Technol. 287 (2016) 43–50. <https://doi.org/10.1016/j.powtec.2015.09.030>.
- [10] C.C. Mwaba, Miner. Eng. 4 (1991) 49–62. [https://doi.org/10.1016/0892-6875\(91\)90118-F](https://doi.org/10.1016/0892-6875(91)90118-F).
- [11] J. Smith, C. Sheridan, L. van Dyk, S. Naik, N. Plint, H.D.G. Turrer, Miner. Eng. 115 (2018) 1–3. <https://doi.org/10.1016/j.mineng.2017.10.011>.
- [12] B.L. Krasnyi, V.P. Tarasovskii, A.B. Krasnyi, Refract. Ind. Ceram. 50 (2009) 107–111. <https://doi.org/10.1007/s11148-009-9156-1>.
- [13] M. Huttunen, L. Nygren, T. Kinnarinen, A. Häkkinen, T. Lindh, J. Ahola, V. Karvonen, Miner. Eng. 100 (2017) 144–154. <https://doi.org/10.1016/j.mineng.2016.10.025>.
- [14] T. Kudra, Dry. Technol. 22 (2004) 917–932. <https://doi.org/10.1081/DRT-120038572>.
- [15] T. Kudra, Dry. Technol. (2012) 1190–1198. <https://doi.org/10.1080/07373937.2012.690803>.
- [16] A.S. Mujumdar, Handbook of Industrial Drying, 4th Ed., CRC Press, Boca Raton (2015), 861–866.
- [17] A. Sass, Ind. Eng. Chem. Process Des. Dev. 7 (1968) 319–320. <https://doi.org/10.1021/i260026a031>.
- [18] United States Geological Survey (USGS), Iron ore in May 2021, <https://d9-wret.s3.us-west-2.amazonaws.com/assets/palladium/production/s3fs-public/atoms/files/mis-202105-feore.pdf> [accessed 6 September 2021].
- [19] B.A. Chaedir, J.C. Kurnia, A.P. Sasmito, A.S. Mujumdar, Dry. Technol. 39 (2021) 1667–1684. <https://doi.org/10.1080/07373937.2021.1907754>.
- [20] Z.H. Wu, Y.J. Hu, D.J. Lee, A.S. Mujumdar, Z.Y. Li, Dry. Technol. 28 (2010) 834–842. <https://doi.org/10.1080/07373937.2010.490485>.
- [21] T. Tsukerman, C. Duchesne, D. Hodouin, Int. J. Miner. Process. 83 (2007) 99–115. <https://doi.org/10.1016/j.minpro.2007.06.004>.
- [22] M. Athayde, M.C. Fonseca, B.M. Covcevic, Miner. Process. Extr. Metall. Rev. 39 (2018) 266–275. <https://doi.org/10.1080/08827508.2017.1423295>.
- [23] A.L. Ljung, T.S. Lundström, B.D. Marjavaara,

- K. Tano, *Int. J. Heat Mass Transf.* 54 (2011) 3882–3890. <https://doi.org/10.1016/j.ijheatmasstransfer.2011.04.040>.
- [24] S. Tan, J. Peng, H. Shi, *Dry. Technol.* 34 (2016) 651–664. <https://doi.org/10.1080/07373937.2015.1070357>.
- [25] J.X. Feng, Y. Zhang, H.W. Zheng, X.Y. Xie, C. Zhang, *Int. J. Miner. Metall. Mater.* 17 (2010) 535–540. <https://doi.org/10.1007/s12613-010-0354-0>.
- [26] W. Namkung, M. Cho, *Dry. Technol.* 22 (2004) 877–891. <https://doi.org/10.1081/DRT-120034268>.
- [27] T.C. Souza Pinto, A.S. Souza, J.N.M. Batista, A.M. Sarkis, L.S.L. Filho, T.F. Pádua, R. Béttega, *Dry. Technol.* 39 (2020) 1359–1370. <https://doi.org/10.1080/07373937.2020.1747073>.
- [28] A. Okunola, T. Adekanye, E. Idahosa, *Res. Agric. Eng.* 67 (2021) 8–16. <https://doi.org/10.17221/48/2020-RAE>.
- [29] N. Zhang, L. Shi, H. Qi, Y. Xie, L. Cai, *Dry. Technol.* 34 (2016) 161–166. <https://doi.org/10.1080/07373937.2015.1012677>.
- [30] J.Q. Xu, R.P. Zou, A.B. Yu, *Powder Technol.* 169 (2006) 99–107. <https://doi.org/10.1016/j.powtec.2006.08.004>.
- [31] AOAC, *Official Methods of Analysis of the Association of Official Analytical Chemists*, 17th ed., AOAC International, Maryland (2002).
- [32] G. Albin, F.B. Freire, J.T. Freire, *Chem. Eng. Process. - Process Intensif.* 134 (2018) 97–104. <https://doi.org/10.1016/j.cep.2018.11.001>.
- [33] R.C. de Brito, T.F. de Pádua, J.T. Freire, R. Béttega, *Chem. Eng. Process. - Process Intensif.* 117 (2017) 95–105. <https://doi.org/10.1016/j.cep.2017.03.021>.
- [34] M.G.A. Vieira, L. Estrella, S.C.S. Rocha, *Dry. Technol.* 25 (2007) 1639–1648. <https://doi.org/10.1080/0737393701590806>.
- [35] A.E. Takegoshi, Y. Hirasawa, S. Imura, T. Shimazaki, *Int. J. Thermophys.* 5 (1984) 219–228. <https://doi.org/10.1007/BF00505502>.
- [36] J. Jang, H. Arastoopour, *Powder Technol.* 263 (2014) 14–25. <https://doi.org/10.1016/j.powtec.2014.04.054>.
- [37] T. Kudra, *Chem. Process Eng.* 19 (1998) 163–172. ISSN 0208-6425.
- [38] E. Holtz, L. Ahrné, T.H. Karlsson, M. Rittenauer, A. Rasmuson, *Dry. Technol.* 27 (2009) 173–185. <https://doi.org/10.1080/07373930802603334>.
- [39] P. Karimi, H. Abdollahi, N. Aslan, M. Noaparast, S.Z. Shafaei, *Miner. Process. Extr. Metall. Rev.* 32 (2011) 1–16. <https://doi.org/10.1080/08827508.2010.508828>.
- [40] Z. Cai, Y. Feng, H. Li, X. Liu, *Miner. Process. Extr. Metall. Rev.* 36 (2015) 1–6. <https://doi.org/10.1080/08827508.2012.762915>.
- [41] K. Meyer, *Pelletizing of Iron Ores*, Springer-Verlag, Heidelberg (1980).
- [42] A. Midilli, H. Kucuk, Z. Yapar, *Dry. Technol.* 20 (2002) 1503–1513. <https://doi.org/10.1081/DRT-120005864>.
- [43] E.M. Silva, J.S. Da Silva, R.S. Pena, H. Rogez, *Food Bioprod. Process.* 89 (2011) 39–46. <https://doi.org/10.1016/j.fbp.2010.03.004>.
- [44] G.E.P. Box, J.S. Hunter, W.G. Hunter, *Statistics for Experimenters: Design, Innovation and Discovery*, 2nd Ed., John Wiley & Sons, New Jersey (2005). ISBN: 978-0-471-71813-0.

AMARÍLIS SEVERINO E
SOUZA¹
THIAGO CÉSAR DE SOUZA
PINTO²
ALFREDO MOISÉS SARKIS³
THIAGO FAGGION DE
PÁDUA¹
RODRIGO BÉTTEGA¹

¹Federal University of São
Carlos, Department of Chemical
Engineering, Drying Center of
Pastes, Suspensions, and
Seeds, São Carlos, SP, Brazil

²Mineral Development Center -
CDM/Vale, Santa Luzia, MG,
Brazil

³Instituto Tecnológico Vale - ITV,
Santa Luzia, MG, Brazil

ENERGETSKA ANALIZA KONVEKTIVNOG SUŠENJA FINE GVOZDENE RUDE

Operacije sušenja u postrojenjima za preradu rude gvožđa imaju posebno veliku potražnju za energijom zbog velikog protoka čvrstog materijala koji se koristi u ovoj industriji. ³ potpuni faktorijalni plan je primenjen za istraživanje uticaja temperature vazduha, brzine protoka vazduha i količine čvrstog materijala na vreme sušenja i specifičnu potrošnju energije konvektivnog sušenja fine rude gvožđa u nepokretnom sloju. Rezultati su pokazali da je svaki uslov vazduha za sušenje bio povezan sa optimalnom količinom čvrstog materijala koje je minimiziralo specifičnu potrošnju energije. Količina od 73 g (visina sloja od oko 0,8 cm) je identifikovana i potvrđena kao optimalna u pogledu potrošnje energije za konfiguraciju sa najvišom temperaturom (90 °C) i brzinom protoka vazduha (4,5 m/s). Pri ovom uslovu vreme sušenja je 29 s i odgovarajućom specifičnom potrošnjom energije od 12,8 MJ/kg, pri čemu se vlaga smanjuje sa 0,11 kg vode/kg suve čvrste materije na 0,05 kg vode/kg suve čvrste materije. Identifikovanje optimalnih vrednosti za procesne promenljive trebalo bi da pomogne u projektovanju i radu energetski efikasnih konvektivnih sušara za fine rude gvožđe.

Ključne reči: aglomerati gvozdene rude, granica prenosive vlage, potrošnja energije, efikasnost sušenja, peletna hrana.

NAUČNI RAD

VENUGOPAL PALANISWAMY¹
KALIAPPAN SEENIAPPAN²
THANIGAIVELAN
RAJASEKARAN³
NATRAYAN LAKSHMAIYA⁴

¹Department of Mechanical Engineering, Muthayammal College of Engineering, Rasipuram, Namakkal (Dt), Tamil Nadu, India

²Department of Mechanical Engineering, Velammal Institute of Technology, Tamil Nadu, Chennai, India

³Department of Mechanical Engineering, AKT Memorial College of Engineering and Technology, Kallakurichi, Tamil Nadu, India

⁴Department of Mechanical Engineering, Saveetha School of Engineering, SIMATS, Tamil Nadu, Chennai., India

SCIENTIFIC PAPER

UDC 544.5/.6:621

ENHANCING MRR AND ACCURACY WITH MAGNETIZED GRAPHITE TOOL IN ELECTROCHEMICAL MICROMACHINING OF COPPER

Article Highlights

- The effect of graphite and magnetized tool in EMM is reported
- Electro-magnetized graphite tool electrode shows a higher machining rate and lower overcut
- Graphite electrode produces an 11.9% reduced overcut

Abstract

Micro hole is the fundamental feature found in any device and its components. Hence this paper aims to produce the micro holes using electrochemical micromachining (EMM). The existing machining techniques in EMM for creating micro holes are associated with more overcut (OC). Hence, reducing OC and enhancing the machining rate (MR) is essential. This paper aspires to investigate the effect of the graphite electrode with magnetic force on the copper plate. Four different tools, namely the electromagnetic graphite tool (EMGT), permanent magnet graphite tool (PMGT), graphite tool, and stainless steel (SS) tool, are employed for these experiments. The major influencing factors are machining voltage in volts, duty cycle in % and electrolyte concentration in g/l was considered on MR and OC. The results revealed that EMGT, PMGT, and graphite electrodes produce MR of 106.4%, 74.6 % and 44.5 % over the SS tool at a parameter level of 23 g/l, 15 V, and 85%, respectively. Furthermore, graphite and EMGT electrodes resulted in 11.9% and 3.41% reduced OC, respectively, than the SS tool at parameter levels of 8 V, 95% and 28 g/l. Additionally, the scanning electron microscope (SEM) picture examination is conducted to identify the magnetic field effect on the work surface.

Keywords: electrode, electromagnet, coating, machining rate, overcut.

Copper, one of the finest ductile nature materials. is appropriate material for manufacturing power circuit boards, automobile parts, and medical and biomedical components. Due to its crystalline nature, the copper material produces more burrs while machining through conventional technology due to the tool structure,

rotational speed and cutting forces [1,2]. On the other hand, among various techniques in unconventional methods, EMM provides the right solutions for the problems stated above due to its advantages characteristics such as non-contact machining, no tool wear, high precision and excellent surface finish etc., [3,4]. To enhance the machining rate, researchers worldwide followed various strategies in EMM. Sharma *et al.* [5] studied the EMM performance with different pulsed voltages to obtain high accuracy and machining rate on stainless steel workpieces. They employed the various waveforms of pulsed current, such as rectangular, sinusoidal, triangular and half-wave rectified power supplies. Among these waveforms,

Correspondence: T. Rajasekaran, Department of Mechanical Engineering, AKT Memorial College of Engineering and Technology, Kallakurichi, Tamil Nadu, India-606 202.

E-mail: tvelan10@gmail.com

Paper received: 31 July, 2022

Paper revised: 11 October, 2022

Paper accepted: 14 October, 2022

<https://doi.org/10.2298/CICEQ220731027P>

triangular improves accuracy. Bian *et al.* [6] attempted with five different electrodes, namely SS, aluminium alloy, brass, tungsten and steel, to realize the influence of tool materials on the EMM performance. The stray current effect in the machining zone was slowed down while using aluminium alloy due to the formation of oxide layers on the electrode surface. These oxide layers act as side insulation attributes for lesser OC. Also, micro holes' machining rate and quality are 3 times better with aluminium alloy than other materials. Zhan *et al.* [7] have generated gas bubbles around the electrode to provide an insulating effect in the EMM process. These generated gas bubbles remove the machined products quickly, stabilize the current flow, and improve the machining rate by 2.6 times over normal EMM processes. Rajkeerthi *et al.* [8] employed \varnothing 300 μ m fabricated hollow tool in the EMM process on the nickel-based superalloy. The MR and OC improved by 2.04% and 24.57%, respectively for the fabricated hollow tool. Kunar *et al.* [9] have improved micro-hole accuracy by applying rectangular waveform voltage in the EMM process on SS 304 work material with masked tool electrodes. Soundarrajan *et al.* [10] employed hot air in the EMM process to study the effect of electrolyte temperature on the copper work material. The results reveal that using citric acid for the copper work materials produces the non-conductive dissolved products surrounding the tool and create the insulating effect for improving micro-hole accuracy. Mouliprasanth *et al.* [11] tried different electrolytes for machining shape memory alloy in EMM with SS electrodes. Among those electrolytes, passivating electrolyte shows a higher machining rate than the non-passivating electrolyte. Shanmugam *et al.* [12] fabricated the stainless-steel electrode through additive manufacturing and used it in the EMM process to study its effects on titanium alloy. The machining parameters such as voltage, concentration and duty cycle are varied on the MR, OC and conicity. They noted the improved OC and conicity with the fabricated tool due to the higher molecular bond than the normal electrode. Liu *et al.* [13] have used novel silver-coated glass tube electrodes to control the stray current effect in the EMM process. Yang *et al.* [14] conducted the EMM experiments with hollow electrodes with a vibrating workpiece at a 1.5 Hz frequency to ensure the continuous removal of machined products. The uniform current flow and distribution in the machining zone due to the workpiece's vibration contribute to a high-precision micro hole. Pradeep *et al.* [15] investigated the EMM process parameters with graphite electrodes for SS 304 work material. They compared the results of graphite electrodes to the cryogenically treated tool and normal electrodes. The surface of micro holes was noted with fewer stray cuts while using cryogenically

treated electrodes than other electrodes. Arul *et al.* [16] have utilized square shape composite electrodes in the EMM for the copper work material. The composite square tool produces sharp corners than normal stainless-steel electrodes while machining rectangular slots. Gopinath *et al.* [17] conducted experiments on a titanium alloy with the assistance of a magnetic field using the EMM process. They noted 68%, 47%, and 55% improvement in the MR, OC and surface roughness, respectively, for magnetic field-assisted machining compared to non-magnetic machining. Palani *et al.* [18] studied the suitability of electrode material in the EMM process for a nickel-based alloy. The materials, such as copper, tungsten and brass, are considered electrode materials, and the response surface methodology technique has been employed to understand the relation between the process variables and responses. They noted that copper and tungsten produce the improved MR and OC, respectively, compared to the brass electrode. Liu *et al.* [19] studied the EMM process through a helical electrode with a jet electrolyte. This type of electrode hinders the stray current corrosion near the micro holes. Patel *et al.* [20] tried the flexible electrode in the EMM process to fabricate the micro texture on the SS 304 work material. They created the curvatures in the electrode to increase the machining zone's current density. Soundarrajan *et al.* [21] studied the influence of different electrode coating on copper work material through the EMM process. The length of the tool and coating thickness significantly affects the machining performance.

Saravanan *et al.* [22] studied the ultraviolet rays and magnetic field coupled effect on the EMM performances and employed various optimization techniques, such as TOPSIS, VIKOR and GRA. Vats *et al.* [23] examined the EMM performance using different electrolyte temperatures on Inconel alloy and noted a 4-19% improvement in the MR at 40 °C. Vinod Kumar *et al.* [24] studied the EMM process using a magnetic field on a SS 316 work material. They found a 1.82 times higher MR over the normal EMM process. Geethapiriyam *et al.* [25] conducted experiments using a nickel-coated electrode in the EMM of titanium alloy. They observed a better surface finish and 12% improved OC by nickel-coated tools than the standard electrode. Maniraj *et al.* [26] fabricated a different set-up to heat the electrode and studied the machining characteristics. The heated electrode results in 37 % and 88 % improvement in the OC and MR, respectively. Liu *et al.* [27] have employed non-conductive materials on the tool steel alloy, such as SiO₂ and Si₃N₄ insulated tools. They noted considerable development in the taper angle of the hole and OC. Guo *et al.* [28] carried out experiments in the EMM on the nickel superalloy through the rotating electrode. The tool rotation speed

instantly pushes out the electrolytic products from the machining zone and causes a higher MR. Mouliprasanth and Hariharan [29] have studied the effect of mixed electrolytes on the ECMM process and found an improvement in machining speed, circularity, conicity, and overcut. Thanigaivelan *et al.* [30] employed different tool tips coated with the epoxy insulation in EMM for machining SS 304. Wang *et al.* [31] adopted the spherical tool in The EMM process to study the effect of tool rotation on the taper angle of the hole and MR. They noticed a 139% reduced taper angle of the hole and a 43% improvement in the MR.

It is clear from the literature mentioned above that researchers have attempted to enhance MR and OC with modified tools. Although many techniques exist, namely tool modifications and insulation, it is still challenging to insulate the tool economically at the micro level. Therefore, in this study, an attempt was made to affect the copper plate with a graphite electrode and magnetic field. Commercially available graphite pencil tips are considered electrodes combined with electromagnetic and permanent magnet effects. Generally, electromagnets and permanent magnets are successfully employed in various sectors, such as biomedical and electronics, for different applications. Although Gopinath *et al.* [17] have applied a magnetic field for machining titanium alloy in EMM, a detailed study is needed to understand the effect of the magnetic field in the EMM process. This magnetic effect could repel the machined product and instantly refresh the electrolyte at the machining zone. Therefore, it is important to investigate the influences of magnetic and non-magnetic graphite tools with SS tools on the EMM performance. The most significant EMM process variables, machining voltage in V, duty cycle in %, and electrolyte concentration in g/l, were considered for the experiment. In addition, the output responses, such as MR and OR, are considered for assessing the EMM performance. Furthermore, SEM image analyses of machined surfaces were done to explore the effect of the magnetic force on micro holes.

EXPERIMENTAL

The experiments were conducted through an indigenously fabricated EMM set-up. The set-up incorporated different subcomponents, such as tool control arrangement, electrolyte supply system, electrolyte tank and microcontroller system. The workpiece of a 1 mm thick copper plate, \varnothing 500 μ m SS rod, and commercially available graphite were used as tool electrodes for the experiments. The tools were insulated with epoxy resin to control the stray current, and sodium nitrate (NaNO_3) under different

concentrations was used as an electrolyte. The micro-hole completion was witnessed by the progression of gas bubbles beneath the workpiece. Four different electrodes were used in the experiments. The remaining tools were made of graphite material besides the standard electrode. The electromagnetic tool (EMT) holder was fabricated and energized separately. The commercially available graphite pencil tip was fixed with an EMT holder, which is wound with insulated copper coils of diameter 10 mm. Based on Ampere's law of electromagnetism, the electromagnetic flux was induced by an electric current when it passed through the graphite material. The EMT holder set-up was connected to a separate power supply unit. Also, commercially available ten numbers of round hollow N 52 grade permanent neodymium magnets were used as another tool. The use of permanent magnets produced a constant magnetic flux and electromagnets with varying magnetic flux. The MR was calculated by dividing the thickness of the workpiece by the time taken for machining through the hole. The difference in diameter between the tool electrode (constant) and the top side micro hole was noted to find the OC of the micro hole. The major factors and their range are displayed in Table 1. The plan of experiments was developed according to the method of varying one factor at a time.

Table 1. Machining parameters and their levels.

Machining parameters	Units	Range
Type of Electrode	-	Electromagnetic Graphite Tool (EMGT), Permanent Magnet Graphite Tool (PMGT), Graphite tool and stainless steel (SS) tool
Machining Voltage (MV)	V	8,9,10,11,12
Duty cycle (DC)	%	55,65,75,85,95
Electrolyte concentration (EC)	g/l	20,22,24,26,28
Frequency	Hz	85

RESULTS AND DISCUSSION

Effect of machining voltage on MR and OC

Figure 1a presents the dependence of machining voltage on MR for various tool electrodes. It shows that the PMGT electrode produces the highest MR among the tested electrodes. An increase in voltage level increases the MR. The combined magnetic and electrical force of a round magnet increases the MR. The round-shaped magnets constantly induce the magnetic flux in the machining zone. Along with that

electric force in between the inter-electrode gap (IEG) removes the machined product quickly. The quick and continuous removal of machined products leads to a higher MR [32,33]. In the PMGT electrode, the MR is 106.4% higher than the SS tool for the parameter level of 8 V, 95%, and 28 g/l. Also, this value is the maximum MR in all experiments conducted by different types of electrodes. This phenomenon is because the constant magnetic field effects accelerate the displacement of the ions in the electrolyte, which triggers the flow of electricity in addition to other chemical changes [34]. The delocalized electrons in graphite cause its conductivity. A magnetic effect is generated when the current passes through the graphite electrode, surrounded by a permanent magnet. This effect attributes to a rise in the MR over other electrode types. Concerning the EMGT electrode, a discontinuous magnetic flux in the electrolyte is responsible for the next highest MR. In the EMGT, the magnetic flux generation depends on the quantity of voltage supplied to the coil. Generally, the presence of salt in the electrolyte increases the conductivity. Also, the magnetic flux creates the turbulence effect on electrolyte molecules and leads to higher conductivity [35,36]. The EMGT electrode produces a 74.6% higher MR than the SS tool. The graphite tool electrode induces the electrostatic effect when current is passed through it. This phenomenon of electrostatic flux pulls out the machined products from the IEG and machining area. Therefore, the graphite tool electrode produces a 44.5% increased MR over the SS tool. Moreover, the PMGT, EMGT and graphite electrodes produce an

increased MR of 82.04%, 55.5%, and 28.8%, respectively, for the parameter solution of 9 V, 95% and 28 g/l over the SS tool.

Figure 1 (b) displays the influences of voltage over OC for different tool electrodes. As per the graph, the graphite electrode reduces the OC to 258 μm at a parameter solution of 8 V, 95%, and 28 g/l. Moreover, this is the first least OC value in the experiment. The rising level of machining voltage contributes more to the OC. The graphite electrode is made up of a hexagonal molecular structure, and this formation of an atom causes its excellent electrical conductivity. This phenomenon and electrostatic pull-out force are attributed to a lesser OC [37]. The use of EMGT and PMGT produces the next lowest OC. The Graphite tool electrode resulted in an 11.9% lesser OC than the standard SS tool electrode. The EMGT electrode creates the second lesser OC (283 μm), which is 3.41% lower than the SS tool for similar parameters. Also, the PMGT electrode generates OC of 292 μm , which is 3.03% lesser than the SS tool. In this, EMGT takes slight edge improvement than PMGT electrode. The round-shaped permanent magnet swirls the electrolyte molecules rapidly in the machining zone, leading to the dissolution of the excess materials with PMGT than EMGT electrode [38]. As a result, the graphite, EMGT, and PMGT electrodes produce an OC of 302 μm (i.e. 39.2% enhancement), 311 μm (i.e. 8.48% enhancement), and 320 μm (i.e. 5.76% enhancement), respectively, at the parameter combination of 8 V, 95% and 28 g/l compared to the SS tool.

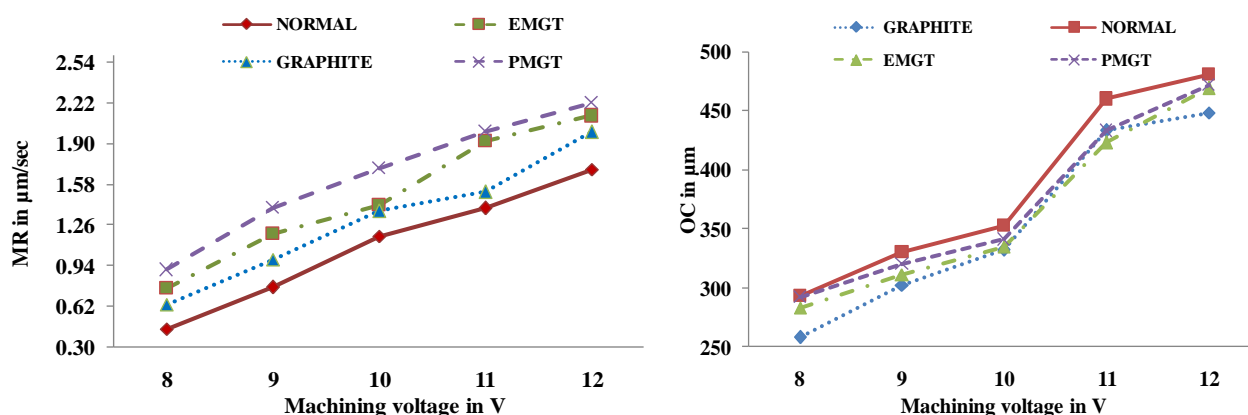


Figure 1. Influence of machining voltage on (a) MR and (b) OC.

Effect of duty cycle on MR and OC

Figure 2a represents the influence of the duty cycle over the MR for all four tool electrodes. The graph infers that the PMGT electrode produces the highest MR than other tools, and the MR increases with respect to the duty cycle. The increase in the duty cycle induces the electrochemical reaction and generates hydrogen

bubbles near the electrode due to the application of permanent magnets [38]. The higher formation of hydrogen bubbles contributes to the higher bubbles diffusions, which attribute to the micro-moving force, leading to the quick refreshment of the electrolyte and a fast electron movement [27]. Thus, the PMGT electrode generates a 61.76% elevated MR compared

to the SS tool at the parametric levels of 55%, 12 V, and 28 g/l. The next maximum MR is attained with the EMGT electrode, which generates a 39.92% higher MR than the SS tool. The graphite electrode contributes the second highest MR, which is 21.8% higher than the SS tool. These PMGT, EMGT, and graphite tool electrodes produce the maximum MR, i.e. 97.8%, 67.5%, and 61.9% higher than the SS tool, respectively, at the parameter levels of 65%, 12 V, and 28 g/l.

Figure 2b illustrates the influences of the duty cycle on the OC for various tool electrodes. The graphite electrode enlarges the OC to 289 μm for 55%, 12 V, and 28 g/l. In general, due to the electrochemical and magnetic effect, the electrolyte temperature rises in the machining zone to a certain extent. These temperature changes create a good bonding between the graphite electrode surface and epoxy coating [39]. Hence, this phenomenon arrests the stray current and confines the current flow attributing to a lesser OC than others. The EMGT and PMGT electrodes generate the next lesser OC, i.e. 307 μm and 319 μm , respectively than the SS tool for the same parameter level. The EMGT and PMGT electrodes produce 10.14% and 7.89% lower OCs than the SS tool. In addition, at the

parametric level of 65%, 12 V, and 28 g/l, the graphite, EMGT, and PMGT electrodes generate lower OC of 390 μm (i.e. 10.1%), 395 μm (i.e. 8.99%) and 390 μm (i.e., 10.1%) respectively than the SS tool. SEM images in Figure 3 (a–b) present the micro hole machined with different electrodes, such as the EMGT and PMGT, for the parameters 55%, 12 V, and 28 g/l. The graphite electrode shows good-quality holes, and the magnetic field effect shows unnecessary material erosion over the edge of the micro-hole. Figure 3a shows the electromagnetic effect of disproportionate material removal on the circumference compared to the PMGT, as shown in Figure 3b.

Effect of electrolyte concentration on MR and OC

Figure 4a presents the influences of the electrolyte concentration on the MR using various tool electrodes, and the MR increases with the electrolyte concentration. The PMGT electrode generates the maximum MR among the electrodes because the graphite electrodes undergo a galvanic chemical reaction in the electrolyte solution [40].

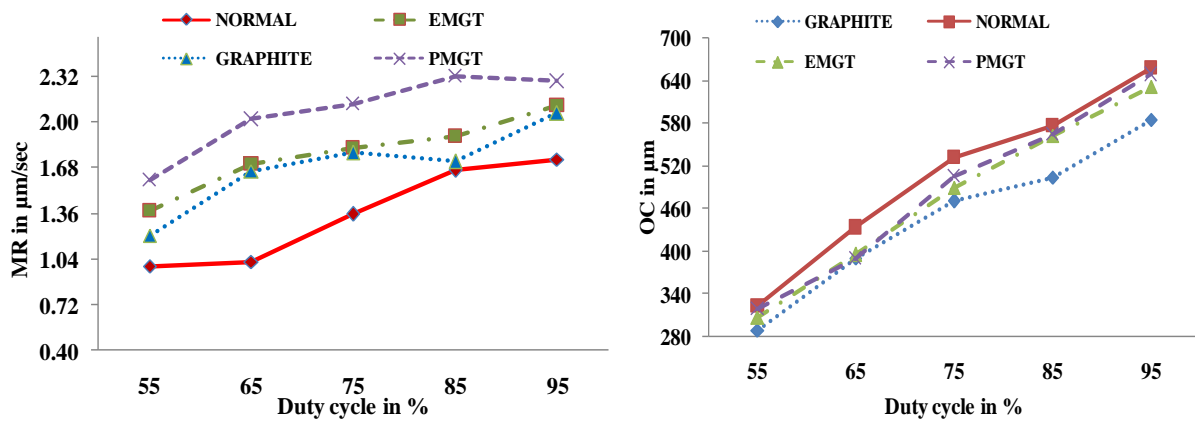


Figure 2. Influence of duty cycle on (a) MR and (b) OC.

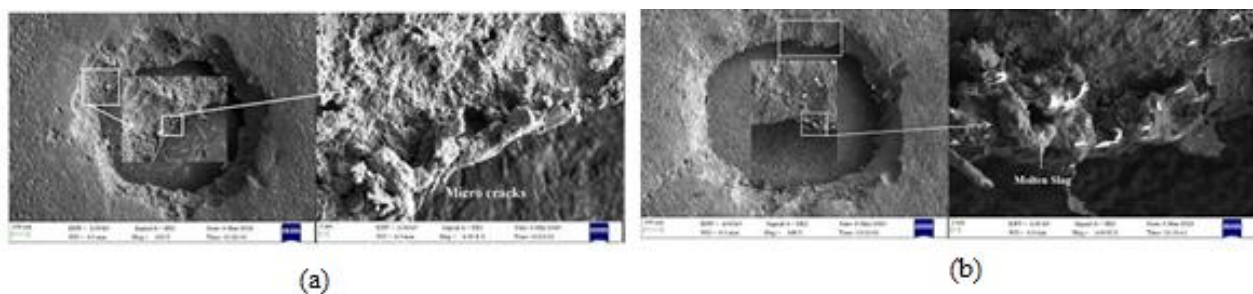


Figure 3. SEM image of micro holes machined at 55%, 12 V, and 28 g/l for (a) EMGT and (b) PMGT.

In the PMGT electrode, the positive and negative polarization galvanic reaction occurs at the IEG, leading to a high MR. During this reaction, the chance for adherence of sludge to the graphite electrode surface is more [41]. In addition, with magnetic Lorentz force, the PMGT electrode produces a 104% maximum MR compared to the SS tool for the parameter levels of 20 g/l, 12 V, and 95%. The EMGT electrode exhibits the next highest MR for a similar parameter level. The EMGT electrode contributes 86.9% higher MR than the SS tool. The MR for the graphite tool electrode is 77.2% higher than for the SS tool. Furthermore, at the parametric levels of 22 g/l, 12 V, and 95%, PMGT, the EMGT and graphite electrodes show 97.8%, 78.5%, and 38.5% higher MR compared to the SS tool.

Figure 4b shows the influence of the electrolyte concentration on the OC for various tools. The graphite, EMGT, and PMGT electrodes generate the OC of

177 μm , 182 μm , and 188 μm , respectively, for the parameter levels of 22 g/l, 12 V, and 95%. Moreover, these OC values are the lowest among the conducted experiments [15]. The graphite electrode shows a 15.02% lesser OC than the standard SS tool. Figure 5a portrays the micro holes fabricated with the graphite electrodes. The figure clears that circumference of the micro holes is precise, and there is less etching surface due to the confined current distributions on the machining area. The SEM micrograph presented in figure 5 (b) shows the micro-hole fabricated with EMGT at the parameter level of 20 g/l, 12 V, and 95%. The over-etching surface is witnessed on its circumference. The PMGT electrode offers the next lowest OC. Hence, in the PMGT electrode, the OC is 10.6% lower than that of the SS tool. Figure 5c presents the micro-hole fabricated through the PMGT electrode. Figure 5 (d) shows the micro-hole surface machined using the SS tool at 20 g/l, 12 V, and 95%.

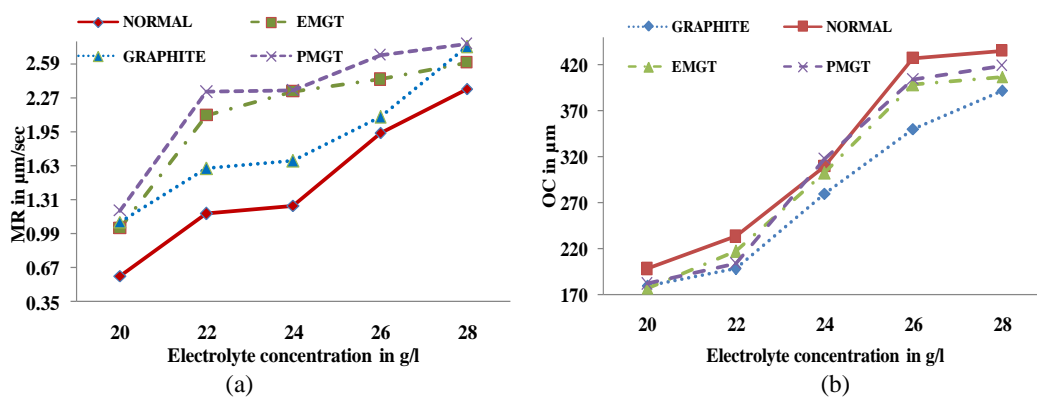


Figure 4. Influence of electrolyte concentration on (a) MR and (b) OC.

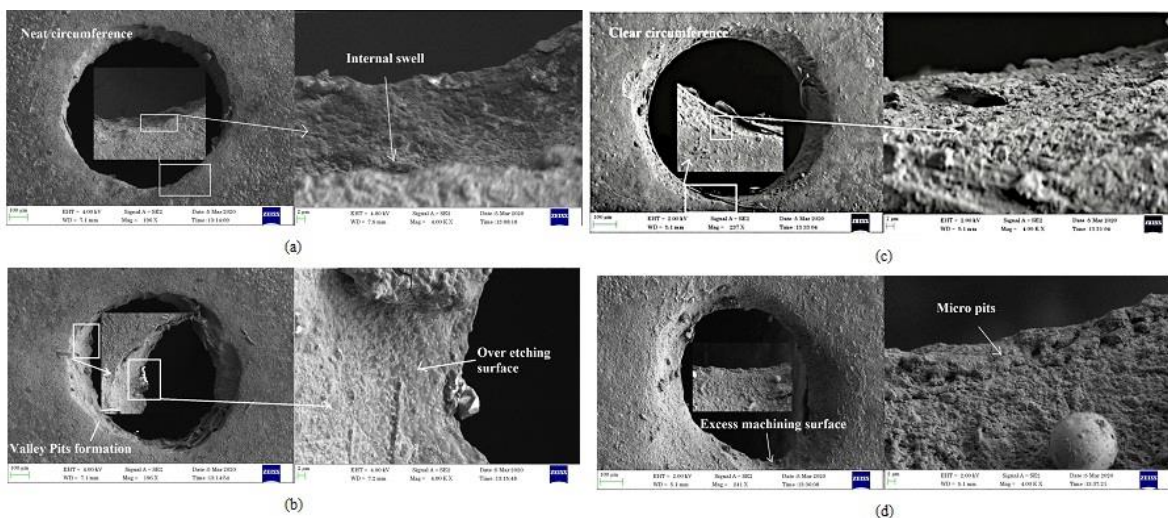


Figure 5. SEM image of micro holes machined at 20 g/l, 12 V and 95% for (a) Graphite, (b) EMGT, (c) PMGT, and (d) SS tool.

CONCLUSION

Four different electrodes, such as the EMGT, PMGT, graphite, and SS tool, are used for the experiments. The experimental results show that the PMGT electrode produces a 106.4% higher MR than the standard SS tool for the parameter solution of 8 V, 95%, and the EMGT electrode of 74.6% shows 28 g/l and the next highest MR. The graphite tool electrode produces a 44.5% increased MR compared to the SS tool electrode due to the electrostatic effect. The graphite tool electrode resulted in an 11.9 % lesser OC than the SS tool. The EMGT electrode creates the second lesser 283 μm OC, which is 3.41 % lower than the SS tool for the parameter solution of 8 V, 95% and 28 g/l. Based on the investigation, the PMGT and EMGT electrodes are recommended where the MR is in demand, and the graphite electrode could be chosen for enhancing the accuracy. Further experiments can be planned, such as different tool electrode materials and magnetic fields.

ACKNOWLEDGEMENT

This dataset is the outcome of the experiments carried out in the Department of Mechanical Engineering, Muthayammal Engineering College, Rasipuram, India. The authors are also thankful for all the support the institution provides.

REFERENCES

- [1] X. Wu, L. Li, N. He, M. Zhao, Z. Zhan, *Int. J. Adv. Manuf. Technol.* 79 (2015) 321–327. <https://doi.org/10.1007/s00170-015-6828-5>.
- [2] R. Thanigaivelan, R.M. Arunachalam, P. Drukpa, *Int. J. Adv. Manuf. Technol.* 61 (2012) 1185–1190. <https://doi.org/10.1007/s00170-012-4093-4>.
- [3] M. Soundarrajan, R. Thanigaivelan, *Russ. J. Appl. Chem.* 91 (2018) 1805–1813. <https://doi.org/10.1134/S1070427218110101>.
- [4] J.R. Vinod Kumaar, R. Thanigaivelan, M. Soundarrajan, *Mater. Manuf. Process.* 37 (2022) 1526–1539. <https://doi.org/10.1080/10426914.2022.2030874>.
- [5] V. Sharma, P. Gupta, J. Ramkumar, *J. Manuf. Process.* 75 (2022) 110–124. <https://doi.org/10.1016/j.jmapro.2022.01.006>.
- [6] J. Bian, B. Ma, H. Ai, L. Qi, *Materials* 14 (2021) 2311. <https://doi.org/10.3390/ma14092311>.
- [7] S. Zhan, Y. Zhao, *J. Mater. Process. Technol.* 291 (2021) 117049. <https://doi.org/10.1016/j.jmatprotec.2021.117049>.
- [8] E. Rajkeerthi, P. Hariharan, N. Pradeep, *Mater. Manuf. Process.* 36 (2021) 488–500. <https://doi.org/10.1080/10426914.2020.1843672>.
- [9] S. Kunar, B. Bhattacharyya, *J. Adv. Manuf. Syst.* 20 (2021) 27–50. <https://doi.org/10.1142/S0219686721500025>.
- [10] M. Soundarrajan, R. Thanigaivelan, *Russ. J. Electrochem.* 57 (2021) 172–182. <https://doi.org/10.1134/S1023193521020117>.
- [11] B. Mouliprasanth, P. Hariharan, *Russ. J. Electrochem.* 57 (2021) 197–213. <https://doi.org/10.1134/S1023193521030095>.
- [12] R. Shanmugam, M. Ramoni, G. Thangamani, M. Thangaraj, *Metals* 1 (2021) 778. <https://doi.org/10.3390/met11050778>.
- [13] G. Liu, H. Tong, Y. Li, H. Zhong, *Precis. Eng.* 72 (2021) 356–369. <https://doi.org/10.1016/j.precisioneng.2021.05.009>.
- [14] T. Yang, X. Fang, Y. Hang, Z. Xu, Y. Zeng, *Int. J. Adv. Manuf. Technol.* 116 (2021) 2651–2660. <https://doi.org/10.1007/s00170-021-07556-8>.
- [15] N. Pradeep, K.S. Sundaram, M. Pradeep Kumar, *Mater. Manuf. Process.* 35 (2020) 72–85. <https://doi.org/10.1080/10426914.2019.1697445>.
- [16] T.G. Arul, V. Perumal, R. Thanigaivelan, *Chem. Ind. Chem. Eng. Q.* 28 (2022) 247–253. <https://doi.org/10.2298/CICEQ210501036A>.
- [17] T.P. Gopinath, J. Prasanna, C.C. Sastry, S. Patil, *Mater. Sci.-Pol.* 39 (2021) 124–138. <https://doi.org/10.2478/msp-2021-0013>.
- [18] S. Palani, P. Lakshmanan, R. Kaliyamurthy, *Mater. Manuf. Process.* 35 (2020) 1860–1869. <https://doi.org/10.1080/10426914.2020.1813888>.
- [19] B. Liu, H. Zou, H. Luo, X. Yue, *Micromachines* 11 (2020) 118. <https://doi.org/10.3390/mi11020118>.
- [20] D.S. Patel, V. Agrawal, J. Ramkumar, V.K. Jain, G. Singh, *J. Mater. Process. Technol.* 282 (2020) 116644. <https://doi.org/10.1016/j.jmatprotec.2020.116644>.
- [21] M. Soundarrajan, R. Thanigaivelan, *Mater. Manuf. Process.* 35 (2020) 775–782. <https://doi.org/10.1080/10426914.2020.1740252>.
- [22] K.G. Saravanan, R. Thanigaivelan, M. Soundarrajan, *Bull. Pol. Acad. Sci.:Tech. Sci.* 69 (2021) e138816. <https://doi.org/10.24425/bpasts.2020.135382>.
- [23] A. Vats, A. Dvivedi, P. Kumar, *Mater. Manuf. Process.* 36 (2020) 677–692. <https://doi.org/10.1080/10426914.2020.1866189>.
- [24] J.R. Vinod Kumaar, R. Thanigaivelan, *Mater. Manuf. Process.* 35 (2020) 969–977. <https://doi.org/10.1080/10426914.2020.1750630>.
- [25] T. Geethapiriyam, A.A. Kumar, A.A. Raj, G. Kumarasamy, J.S. John, *IOP Conf. Ser.: Mater. Sci. Eng.* 912 (2020) p.032039. <https://doi.org/10.1088/1757-899X/912/3/032039>.
- [26] S. Maniraj, R. Thanigaivelan, *Mater. Manuf. Process.* 34 (2019) 1494–1501. <https://doi.org/10.1080/10426914.2019.1655153>.
- [27] G. Liu, Y. Li, Q. Kong, H. Tong, H. Zhong, *Precis. Eng.* 52 (2018) 425–433. <https://doi.org/10.1016/j.precisioneng.2018.02.003>.
- [28] C. Guo, Y. Liu, Z. Wei, J. Niu, *Recent Pat. Mech. Eng.* 10 (2017) 51–59. <https://doi.org/10.2174/2212797610666170208142044>.
- [29] B. Mouliprasanth, P. Hariharan, *Exp. Tech.* 44 (2020) 259–273. <https://doi.org/10.1007/s40799-019-00350-y>.
- [30] R. Thanigaivelan, R. Senthilkumar, R.M. Arunachalam, N. Natarajan, *Surf. Eng. Appl. Electrochem.* 53 (2017) 486–492. <https://doi.org/10.3103/S1068375517050143>.
- [31] Y. Wang, Y. Zeng, N. Qu, D. Zhu, *Int. J. Adv. Manuf. Technol.* 84 (2016) 851–859. <https://doi.org/10.1007/s00170-015-7759-x>.
- [32] W.A. Jorgensen, B.M. Frome, C. Wallach, *Eur. J. Surg.*

- 574 (1994) 83–86.
<https://pubmed.ncbi.nlm.nih.gov/7531030/>.
- [33] D.Y. Wu, J.F. Li, B. Ren, Z.Q. Tian, Chem. Soc. Rev. 37 (2008) 1025–1041. <https://doi.org/10.1039/B707872M>.
- [34] M. Iqbal, M.M. Nauman, F.U. Khan, P.E. Abas, Q. Cheok, A. Iqbal, B. Aissa, Int. J. Energy Res. 45 (2020) 65–102. <https://doi.org/10.1002/er.5643>.
- [35] Y. Lu, Z. Tu, L.A. Archer, Nat. Mater. 13 (2014) 961–969. <https://doi.org/10.1038/nmat4041>.
- [36] Y. Jin, N. Yang, X. Xu, Appl. Therm. Eng. 179 (2020) 115732. <https://doi.org/10.1016/j.applthermaleng.2020.115732>.
- [37] M. Wissler, J. Power Sources 156 (2006) 142–150. <https://doi.org/10.1016/j.jpowsour.2006.02.064>.
- [38] R.C. Cruz Gómez, L. Zavala Sansón, M.A. Pinilla, Exp. Fluids 54 (2013) 1582. <https://doi.org/10.1007/s00348-013-1582-7>.
- [39] O. Sambalova, E. Billeter, O. Yildirim, A. Sterzi, D. Bleiner, A. Borgschulte, Int. J. Hydrogen Energy 46 (2021) 3346–3353. <https://doi.org/10.1016/j.ijhydene.2020.10.210>.
- [40] F. Bellucci, A. Di Martino, C. Liberti, J. Appl. Electrochem. 16 (1986) 15–22. <https://doi.org/10.1007/BF01015979>.
- [41] P. Natarajan, S.S. Karibeeran, P.K. Murugesan, J. Braz. Soc. Mech. Sci. Eng. 43 (2021). 507. <https://doi.org/10.1007/s40430-021-03228-6>.

VENUGOPAL PALANISWAMY¹
 KALIAPPAN SEENIAPPAN²
 THANIGAIVELAN
 RAJASEKARAN³
 NATRAYAN LAKSHMAIYA⁴

¹Department of Mechanical Engineering, Muthayammal College of Engineering, Rasipuram, Namakkal (Dt), Tamil Nadu, India

²Department of Mechanical Engineering, Velammal Institute of Technology, Tamil Nadu, Chennai, India

³Department of Mechanical Engineering, AKT Memorial College of Engineering and Technology, Kallakurichi, Tamil Nadu, India

⁴Department of Mechanical Engineering, Saveetha School of Engineering, SIMATS, Tamil Nadu, Chennai., India

POVEĆAVANJE BRZINE UKLANJANJA MATERIJALA I TAČNOST SA MAGNETIZOVANIM GRAFITNIM ALATOM U ELEKTROHEMIJSKOM MIKROKOMHINIRANJU BAKRA

Mikro rupe su osnovna karakteristika svakog uređaja i njegovih komponenti. Stoga ovaj rad ima za cilj da proizvede mikro rupe pomoću elektrohemijske mikromašinske obrade. Postojeće tehnike elektrohemijske mikromašinske obrade za pravljenje mikro rupa su povezane sa više preseka. Stoga je smanjenje preseka i povećanje brzine obrade od suštinskog značaja. Ovaj rad teži da se istraži efekat grafitne elektrode sa magnetnom silom na bakarnu ploču. Za ove eksperimente korišćena su četiri različita alata, a to su: alat, alat sa stalnim magnetom, grafitni alat i alat od nerđajućeg čelika. Razmatrani su glavni faktori uticaja na brzinu obrade i presek, kao što su: napon obrade u voltima, radni ciklus u % i koncentracija elektrolita u g/l razmatrani su na brzine obrade i preseka. Rezultati su otkrili da elektromagnetni grafitni alat, alat sa stalnim magnetom i grafitne elektrode omogućuju brzinu obrade od 106,4%, 74,6% i 44,5% u odnosu na alat od nerđajućeg čelika pri sledećim uslovima glavnih faktora: 23 g/l, 15 V i 85%, redom.. Štaviše, grafitne i elektromagnetne grafitne elektrode su smanjile presek za 11,9% i 3,41%, redom, u odnosu na alat od nerđajućeg čelika pri sledećim uslovima: 8 V, 95% i 28 g/l. Pored toga, izvršeno je ispitivanje skenirajućim elektronskim mikroskopom da bi se identifikovao efekat magnetnog polja na radnu površinu.

Ključne reči: elektroda, elektromagnet, premaz, brzina obrade, presek.

NAUČNI RAD

LUCAS OLIVEIRA CARDOSO¹
BRUNO SANTOS
CONCEIÇÃO¹
MÁRCIO LUIS LYRA
PAREDES²
SILVANA MATTEDI¹

¹Chemical Engineering
Graduate Program
(UFBA/UNIFACS), Polytechnic
School, Federal University of
Bahia, Salvador, BA, Brazil

²Chemical Engineering
Graduate Program, Rio de
Janeiro State University, Rio de
Janeiro, RJ, Brazil

SCIENTIFIC PAPER

UDC 544.6:66:004

THERMODYNAMIC MODELING OF GAS SOLUBILITY IN IONIC LIQUIDS USING EQUATIONS OF STATE

Article Highlights

- The SRK expressed the same behavior as the CPA EoS for the properties of pure ionic liquids
- The change of the associative schemes did not present differences for pure ILs for CPA EoS
- PC-SAFT with the 4C associative scheme presented the best fit for both pure ionic liquids
- [OMIM][NTf₂] with CO₂ and H₂S had as best models PC-SAFT (4C) and CPA (2B), respectively
- For [EMIM][TfO] with CH₄, CO₂ and H₂S were CPA (NA), PC-SAFT (4C), and SRK, respectively

Abstract

This work aimed at the thermodynamic modeling of gas solubility in ionic liquids (ILs) using the Soave-Redlich-Kwong (SRK), cubic-plus-association (CPA), and perturbed-chain statistical associating fluid theory (PC-SAFT) equations of state. Wherefore, the routines were developed for the parameterization of ILs. Then, the ILs were implemented in the Aspen plus simulator to evaluate the equations of state and explore the phase equilibrium data with the predictive equations and the correlation of the binary interaction parameter. Hence, it was verified the correlation of the density and speed of sound curves presented limitations to correcting the slope of the curves of pure ILs. Nonetheless, the PC-SAFT with the 4C associative scheme demonstrated a better fit for the thermophysical properties. As for the prediction of phase equilibrium for the [EMIM][TfO], the PC-SAFT with the 2B scheme showed a better fit with CO₂, while the CPA with the 2B scheme presented the best result for H₂S. For [OMIM][NTf₂], the PC-SAFT with the 1A scheme showed better results with CO₂, and the CPA with the 2B scheme showed the lowest deviation with H₂S.

Keywords: thermodynamic modeling, ionic liquids, equations of state, associating, Aspen plus.

Natural gas is a fossil fuel formed by a multicomponent mixture, in which it contains methane and other higher alkanes in lesser amounts, as well as acid gases such as carbon dioxide (CO₂) and hydrogen

sulfide (H₂S), nitrogen (N₂), mercaptans, carbonyl sulfide, organic sulfides, and water (H₂O) [1,2].

Moreover, natural gas is a valuable energy source, which can be highlighted as a source of energy for industries and domestic applications due to its abundance and low cost [3], as it is also considered a non-polluting energy source, being in opposition to other fuels [4,5]. Thus, using natural gas in contrast to coal and oil emerges as a less polluting and significant alternative for energy security.

The extracted raw gas is often saturated by a steam of water [6]. Hence, to prevent the formation of

Correspondence: S. Mattedi, Chemical Engineering Graduate Program (UFBA/UNIFACS), Polytechnic School, Federal University of Bahia, Salvador, BA, Brazil.
E-mail: silvana@ufba.br
Paper received: 17 April, 2022
Paper revised: 6 September, 2022
Paper accepted: 29 October, 2022

hydrates and acids due to the presence of carbon dioxide (CO₂) and hydrogen sulfide (H₂S), the water (H₂O) and these gases present in natural gas must be removed, being that these components are alarming due to their negative consequences for humans, equipment, and the environment [5,7]. Among acid gases, H₂S is a very toxic and corrosive contaminant, which can cause various diseases and even death in specific concentrations. Besides, it is noteworthy that the presence of CO₂ contributes to the decrease in the heat capacity of natural gas and the performance of liquefaction processes [5,8,9].

In recent decades, the development of sustainable alternative technologies through green chemistry practices led to the design of solvents with lower environmental impact, such as ionic liquids (ILs). The ILs are salts of organic cations and inorganic or organic anions. The presence of bulky and asymmetric ions concerning single ions of inorganic salts results in a melting point below 100 °C [10]. They have excellent physical, biological, and chemical properties due to their good thermal capacity and low volatility. Hence, they are also safe to manage compared to mineral acids, have high thermal stability compared to commonly used organic solvents, and have a wide adjustable range of acidity, basicity, and solubility in the organic and aqueous solvents [11]. In this way, ILs can offer unique selectivity and replace conventional solvents [12].

In this sense, separation processes aim to obtain a product with greater added value and less environmental impact. In recent years, ILs began to be investigated for the removal of acid gas present in natural gas [4]. For example, Jalili *et al.* [13] observed the solubility of CO₂ is higher in ILs with -CF₃ and [NTf₂]- groups. Meanwhile, Nematpour *et al.* [14] analyzed fluorinated-based ILs and found that [EMIM][TfO] had the potential to be used to separate CO₂ and H₂S from each other. Also, Haider *et al.* [4] showed in their review the effectiveness of CO₂ and H₂S separation following the trend of [EMIM][FAP] > [BMIM][PF₆] > [OMIM][NTf₂]. So, the description of the phase equilibria is of great interest for the design, simulation, and optimization of these processes. Consequently, a good selection and parameterization of the thermodynamic model become essential steps for the reliable representation of the process.

The simulation of the process allows a better understanding of the environment under analysis, identifying problems, formulating strategies, and identifying opportunities for system improvements. Hence, one of the most used commercial process simulators in the chemical and petroleum industry is ASPEN (Advanced System for Process Engineering),

which has a wide library of properties, many thermodynamic models, and tools for the design, simulation, and analysis of components, and equipment [15,16]. On this wise, with the support of the Aspen Plus® process simulator, it was possible to study the properties modeling of associative systems due to its robustness for solving the equations of state present in the simulator.

The goal of this work was to develop thermodynamic modeling using ILs as a solvent to remove acid gases present in natural gas and its application in the Aspen Plus simulator in the analysis of the solubility of ILs, methane, and acid gases. Thus, this work consisted of the thermodynamic modeling of the pure and binary components through the thermodynamic models SRK, CPA, and PC-SAFT based on experimental data from the literature. Furthermore, ILs were parameterized and added to Aspen Plus by Aspen Technology®, as they are not present in the database.

Equations of state

Equations of State (EoS) are used for calculations of thermodynamic properties of pure substances and mixtures in industry and academia, especially for systems at high pressure. The term "high pressure" refers to pressures high enough to significantly change the thermodynamics of the system [17]. The traditional way to extend the application of the EoS to mixtures is using mixing rules, i.e., mathematical expressions that propose the dependence of the EoS on the concentration of species [18].

In this present work, the Soave-Redlich-Kwong (SRK), cubic-plus-association (CPA), and perturbed-chain statistical associating fluid theory (PC-SAFT) EoS were studied to evaluate the representations of the vapor-liquid equilibrium involving acid gases and ILs.

SRK EoS

The SRK EoS appeared in 1972 when Giorgio Soave realized that although the Redlich-Kwong equation (1949) could be applied to calculate with a good degree of accuracy, the volumetric and thermal properties of pure compounds and mixtures often presented poor results for calculations of gas-liquid equilibrium (GLE) of multicomponent mixtures [19]. Nevertheless, it is widely applied in the oil and gas industry, in addition to being widely applied for nonpolar mixtures, for example, hydrocarbons. So, for further details concerning the description of terms and their application related to the SRK, it is recommended to consult the basic works [19–21].

CPA EoS

The CPA was developed by Kontogeorgis *et al.*

[22] to give an EoS suitable for associative fluids and their mixtures based on perturbation theory, which could extend to compounds with hydrogen bonding (polar), thus attending a variety of systems of interest to the oil and gas industry (hydrocarbons, gases, water, alcohols, and glycols). Furthermore, it would be possible to evaluate the performance correlating the vapor pressures of pure compounds and densities in the liquid phase [23].

The CPA EoS can be expressed in terms of pressure as a sum of the SRK cubic equation and the contribution of the association term in the form provided by Michelsen and Hendriks [23].

$$P = \frac{RT}{V_m - b} - \frac{a(T)}{V_m(V_m + b)} - \frac{1}{2} \left(\frac{RT}{V_m} \right) \left(1 + \frac{1}{V_m} \frac{\partial \ln g}{\partial \left(\frac{1}{V_m} \right)} \right) \sum_i x_i \sum_A (1 - X_{Ai}) \quad (1)$$

Hence, for further details concerning the description of terms and their application related to the CPA EoS, it is recommended to consult the basic works [22–24].

PC-SAFT EoS

The PC-SAFT EoS, one of the most prevalent versions of the Statistical Associating Fluid Theory (SAFT) EoS, was pioneered by Gross and Sadowski [25], providing reliable and applicable thermodynamics to model thermodynamic properties of many systems, especially systems that are asymmetric in size [26]. Additionally, the PC-SAFT model proved suitable for pure components and mixtures involving solvents and gases, covering liquid-liquid equilibrium (LLE) and GLE of polymeric systems [27].

The main idea of the perturbation theory is to divide molecular interactions into main and additional contributions, such as attraction and repulsion. The attractive part is divided into dispersive and associative interactions. Meanwhile, the repulsive part is described by the hard-chain term derived from Chapman *et al.* [28], which contains the terms hard-sphere and chain [27], which uses another perturbation theory to include softness in this reference potential.

$$\tilde{a} = \tilde{a}^{\text{res}} + \tilde{a}^{\text{hs}} + \tilde{a}^{\text{chain}} + \tilde{a}^{\text{disp}} + \tilde{a}^{\text{assoc}} \quad (2)$$

The \tilde{a}^{res} represents the residual Helmholtz energy, the \tilde{a}^{hs} represent the contribution of the hard-sphere Helmholtz energy term, the \tilde{a}^{chain} represents the chain Helmholtz energy, the \tilde{a}^{disp} represents the energy of dispersive Helmholtz and, finally, the \tilde{a}^{assoc} represents the associative Helmholtz energy. For

further details concerning the description of terms and their application related to the PC-SAFT EoS, it is recommended to consult the basic works [24,25,27–29].

For the thermodynamic modeling of ILs and acid gases, the SRK, CPA, and PC-SAFT equations of state were used to verify the improvements in calculating the properties of pure components and binaries mixtures. Furthermore, knowing that the SRK can be interpreted as a model for attractive spheres based on the repulsive potential of hard spheres plus dispersive forces, the CPA includes the contribution of SRK plus an association term and, finally, the PC-SAFT, which attractive part also contains an associative term, and terms for chains of segment interacting but a softened repulsive term plus a better-defined attractive dispersion term [25].

Nevertheless, as the vapor pressure of ILs is low and there are usually few available data, this property is difficult to apply to the parametrization of ILs. In this way, Loreno *et al.* [30] developed a methodology using density and speed of sound in the adjustment of the parameters of the pure components with the GC-s-PC-SAFT (Group Contribution Simplified Perturbed Chain Statistical Associating Fluid Theory). However, their work was restricted to assessing the equilibrium of ionic liquid + carbon dioxide and ionic liquid + methane. For this reason, it justifies the emergence of interest in evaluating other thermodynamic models with different associative types for the evaluation of acid gases and, thus, be applied to the calculation of the solubility of ILs and acid gases present in natural gas. Also, those authors did not employ a commercial simulator in their calculations, which is an objective of this work.

METHODOLOGY

ILs

In this work, two fluorinated ILs that dissolve acid gases were selected: 1-ethyl-3-methylimidazolium trifluoromethanesulfonate [EMIM][TfO] (CAS: 145022-44-2) and 1-octyl-3-methylimidazolium bis(trifluoromethyl)sulfonylimide [OMIM][NTf₂] (CAS: 178631-04-4). Therefore, it was necessary to obtain experimental data, such as density (ρ), speed of sound (u), liquid heat capacity at constant pressure (C_p^{liq}), for pure ILs and the GLE with acid gases and methane for evaluation. For the first IL, the experimental data were taken from Vercher *et al.* [31], while the GLE data were obtained from Nematpour *et al.* [14] for [EMIM][TfO]/CO₂ and [EMIM][TfO]/H₂S and from Lee [32] for [EMIM][TfO]/CH₄. For the second IL, the experimental data and the GLE data for [OMIM][NTf₂]/CO₂ and [OMIM][NTf₂]/H₂S were taken

from Zorębski *et al.* [33] and Jalili *et al.* [13], respectively.

Thermodynamic modeling

The comparison between the experimental data and those calculated by the EoS was performed by calculating the absolute average relative deviation (AARD), which is provided as a percentage from Eq. (3):

$$AARD(\%) = \frac{1}{n} \sum_{i=1}^n \left| \frac{V_i^{\text{exp}} - V_i^{\text{cal}}}{V_i^{\text{exp}}} \right| 100 \quad (3)$$

Therefore, the estimation of the parameters took place through the minimization of the objective function (F_{obj}), defined as the weighted sum of squares by the experimental uncertainties in density and speed of sound, according to Eq. (4):

$$F_{obj} = \sum_{i=1}^n \left(\frac{\rho_i^{\text{cal}} - \rho_i^{\text{exp}}}{\delta \rho^{\text{exp}}} \right)^2 + \left(\frac{u_i^{\text{cal}} - u_i^{\text{exp}}}{\delta u^{\text{exp}}} \right)^2 \quad (4)$$

The Swarm method proposed by Kennedy and Eberhart [34] was used to estimate the parameters of the EoS, which iteratively optimizes a problem to improve the candidate solution and then applies lower and upper bounds to obtain better estimates of the parameters. In line with this, the Simplex method described by Nelder and Mead [35] was used to minimize the objective function using the best candidate obtained with the Swarm method since performing this procedure improves the adjustment of the estimated parameters. Finally, the methodology proposed by Topliss *et al.* [36] was used to solve the problem of finding roots of a non-cubic EoS, which reliably converges.

In this way, the program developed outside the Aspen plus simulator for estimating parameters from the density and speed of sound data has protections to guarantee the reliable resolution of the proposed problem.

SRK equation

The SRK EoS is calculated from P_c , T_c , and ω data [19], but for ILs, these experimental properties are difficult to obtain, as the degradation of the IL occurs before reaching the critical point. In this way, these parameters were obtained from the data a_0 , b_{CPA} , and c_1 of the CPA EoS using density and speed of sound data. The model selected in the Aspen plus was the RK-Aspen (SRK), given that the physical part of the CPA EoS uses the c_1 function proposed by Graboski and Daubert [20].

In this wise, the calculation of T_{cm} was performed

using the parameters a_0 , b_{CPA} and c_1 , which can be observed in Equation (5).

$$T_{cm} = \frac{\left(\frac{1+c_1}{c_1} \right)^2}{\left(\frac{1+m_m}{m_m} \right)^2} \frac{\Omega_B a_0}{\Omega_A R b_{CPA}} \quad (5)$$

Moreover, the terms m_m and P_{cm} were obtained according to Equations (6) and (7), respectively.

$$m_m = c_1 \sqrt{\frac{a_0 \Omega_B}{\Omega_A b_{CPA} R T_{cm}}} \quad (6)$$

$$P_{cm} = \Omega_B \frac{R T_{cm}}{b_{CPA}} \quad (7)$$

The parameters of the SRK equation were established considering $T_c^* = T_{cm}$, $P_c^* = P_{cm}$ and the ω was obtained from the consideration of $m_m = c_1$, and, in this way, analytically solved the equation proposed by Graboski and Daubert [20] for obtaining the acentric factor. These results can be found in the Supplementary Material of this work.

CPA equation

The CPA EoS has five pure parameters for each component, in addition to the choice of associative type. In this sense, three parameters refer to the physical part (a_0 , b_{CPA} , and c_1) and two parameters refer to the association (ϵ^{AB} and β^{AB}) [23]. The methodology is like the one applied to the SRK model of this present work, apart from the addition of associative parameters and the choice of associative type, in which parameterizations were conducted in this study using associative schemes 1A, 2B, 3B, and 4C. This work represents an engineering model using association to represent interactions in complex systems involving ILs, which are treated as neutral molecules. Thus, the schemes analyzed in this work correspond to the schemes present in the Aspen plus simulator, and the main discussions of the associative types can be seen elsewhere [24].

The parameters T_{cm} , m_m , and P_{cm} were calculated as shown in Eqs. (5) and (7), and the associative parameters ϵ^{AB} and β^{AB} were determined along with a_0 , b_{CPA} , and c_1 according to the proposed methodology using density and speed of sound, the calculation memory can be found in the Supplementary Material of this work.

PC-SAFT

The PC-SAFT EoS for a non-associative substance necessarily requires three parameters (m_i ,

σ_i , and ε_i) [25], while for the associative components, there are two additional parameters (ϵ^{AB} and K^{AB}), besides the choice of associative type [27]. According to the scenario presented for ILs concerning vapor pressure, the parameterization proposed for the PC-SAFT model follows similarly to the proposal for the CPA, based on the density and speed of sound data. Furthermore, the calculation memory can be found in the Supplementary Material of this work.

The associative term in the CPA and PC-SAFT demand two parameters, the associative energy and the associative volume. Moreover, these parameters may be highly correlated. Hence, in this study, some orders of magnitude for the associative volume were tested better to understand the effect of this parameter in the modeling.

Aspen plus simulator

ILs are compounds not presented in the Aspen plus database; therefore, for the simulation and analysis of pure and binary data, creating a component informing the structure and its properties in the software became necessary. In addition to informing the parameters of the components in the equations of state, it is necessary to add two properties that are ideal gas heat capacity (C_p^{gi}) and Antoine vapor pressure (P_{Ant}^V). Therefore, in this part, the PML equation (Modified API) was selected to adjust the C_p^{gi} of ILs, according to Equation (8).

$$C_p^{gi} = C_{1i} + C_{2i}T + C_{3i}T^2 - \frac{C_{4i}}{T^2} + \frac{C_{5i}}{T} \quad (8)$$

Another important property is the vapor pressure, which is required by the simulator, even if it is not applied in the tests. Thus, a very low value was fixed for the vapor pressure, and the Antoine equation was informed as $\ln(P_{Ant}^V) = -10$ with Antoine pressure in bars.

Another important part is the regression of parameters, which can be performed for pure components or mixtures. So, the regressed binary interaction parameters were obtained from phase equilibrium data, which equations are presented below for the SRK, CPA, and PC-SAFT, respectively.

The SRK model, when dealing with mixtures, uses the mixing rules suggested by Mathias [21]. Thus, the regressed parameters were k_{aij}^0 , k_{aij}^1 , k_{bij}^0 , and k_{bij}^1 as presented in Equations (9) and (10).

$$a = \sum_i \sum_j x_i x_j \sqrt{a_i a_j} \left(1 - k_{aij}^0 - k_{aij}^1 \frac{T}{1000} \right) \quad (9)$$

For CPA, the equation has two parameters for the

k_{ij} , as shown in Equation (11).

$$k_{ij} = k_{ij}^0 + k_{ij}^1 \frac{T}{T_{ref=298.15\text{ K}}} \quad (11)$$

For PC-SAFT, the equation has five parameters for the k_{ij} , but the regression was performed only for two parameters, as shown in Equations (12).

$$k_{ij} = k_{ij}^0 + k_{ij}^1 \frac{T_{ref=298.15\text{ K}}}{T} \quad (12)$$

RESULTS AND DISCUSSION

Thermodynamic modeling of pure components

Parameters of gases for the EoS

The parameters of gases for the EoS were obtained from the literature [25,37–40]. The parameters of gases allowed the validation of the algorithm developed for estimating ILs parameters, which could calculate thermophysical properties and show excellent results. Vapor pressure data also are important for pure components. The thermodynamic models were compared with experimental data for CH₄, CO₂, and H₂S [41], as shown in the Supplementary Material.

Parameters of ILs for the EoS

For pure ILs, the parameters estimated from the liquid density and speed of sound data are presented for the SRK (RK-Aspen model in the Aspen plus simulator), CPA, and PC-SAFT equations of state in Tables 1, 2, and 3, respectively.

Thus, an aspect being observed is the estimation time of the ILs parameters that vary with the models and the amount of experimental data. For example, the [EMIM][TfO] presented seven experimental points for density, while the [OMIM][NTf₂] presented seventeen experimental points. Regarding the liquid heat capacity at constant pressure and speed of sound, the [EMIM][TfO] presented seven experimental points, and the [OMIM][NTf₂] presented twenty-two points. Estimation time and the used computer machine were reported in Supplementary Material.

For the non-associative CPA, three parameters were estimated, while in the associative CPA, five parameters were varied by fixing the values of β^{AB} and obtaining the other four parameters. Hence, when providing Aspen plus with the associative obtained outside the simulator, a limitation was discovered concerning the $\epsilon^{AB/R}$ parameter, in which values above $1.2 \cdot 10^4$ K led to errors in calculating pure components properties. In this way, it was verified that the gradual decrease of the parameter $\epsilon^{AB/R}$ did not affect the

Table 1. Estimated parameters of ILs for the SRK model.

Components	MM [g/mol]	T_c^* [K]	P_c^* [bar]	ω [-]
[EMIM][TfO]	260.23	1217.53	49.742	0.01164
[OMIM][NTf ₂]	475.47	581.50	12.287	2.44405

Table 2. Estimated parameters of ILs for the CPA EoS.

Components	MM [g/mol]	CPA					Associative types
		m_m [-]	T_{cm} [K]	P_{cm} [bar]	ϵ^{AB}/Rb [K]	β^{AB} [-]	
[EMIM][TfO]	260.23	0.50313	1217.53	49.742			NA*
		0.66353	1050.84	42.929	9000.0	1	1A
		0.83466	916.68	37.446	9000.0	1	2B
		0.83466	916.68	37.446	9000.0	0.1	2B
		0.83466	916.68	37.446	9000.0	0.001	2B
		0.83466	916.68	37.446	9000.0	0.00001	2B
		0.83466	916.68	37.446	9000.0	1	3B
		1.21621	716.66	29.272	9000.0	1	4C
[OMIM][NTf ₂]	475.47	3.34491	581.50	12.287			NA*
		3.59020	551.59	11.654	9000.0	1	1A
		3.85350	524.11	11.073	9000.0	1	2B
		3.85350	524.11	11.073	9000.0	0.1	2B
		3.85350	524.25	11.076	9000.0	0.001	2B
		3.85350	524.11	11.073	9000.0	0.00001	2B
		3.85386	524.09	11.072	9000.0	1	3B
		4.44497	475.55	10.045	9000.0	1	4C

*NA: Non-associative.

Table 3. Estimated parameters of ILs for the PC-SAFT EoS.

Components	MM [g/mol]	m [-]	σ [Å]	$\frac{\epsilon_{ij}}{k_b}$ [K]	$\frac{\epsilon^{AB}}{k_b}$ [K]	K^{AB} [-]	Associative types
[EMIM][TfO]	260.23	6.4888	3.5351	373.28			NA*
		6.9693	3.4466	345.90	9000.0	1	1A
		7.4774	3.3617	321.82	12122.6	1	2B
		7.4782	3.3615	321.80	12562.3	0.1	2B
		7.4777	3.3616	321.81	15055.6	0.001	2B
		7.4779	3.3616	321.81	17213.4	0.00001	2B
		7.4775	3.3617	321.82	7424.5	1	3B
		8.6163	3.1968	280.47	9000.0	1	4C
		9.6006	3.8578	355.48			NA*
		10.1783	3.7766	334.53	9000.0	1	1A
[OMIM][NTf ₂]	475.47	10.8035	3.6957	315.22	9000.0	1	2B
		10.8035	3.6957	315.22	9000.0	0.1	2B
		10.8035	3.6957	315.22	9000.0	0.001	2B
		10.8035	3.6957	315.22	9000.0	0.00001	2B
		10.8035	3.6957	315.22	9000.0	1	3B
		12.5487	3.4980	275.55	9000.0	1	4C

*NA: Non-associative.

calculated pure component or mixture properties. Therefore, it was used a default value of $\epsilon^{AB/R} = 9000.0$ K as the Aspen plus software performed the intended procedure correctly and reliably.

Like what was presented in the CPA EoS, the mentioned limitation with the parameter $\epsilon^{AB/kb}$ was also found when dealing with the PC-SAFT EoS. On the

other hand, differently from what was presented for CPA, the PC-SAFT complications were found around $2 \cdot 10^4$ K. Therefore, the estimated values that were above the established limit were also empirically set to the value of $\epsilon^{AB/kb} = 9000.0$ K. The $\epsilon^{AB/kb}$ values that were below this limit were kept in estimated values. In this regard, another valuable piece of information to be

highlighted is that there is a relationship between the optimal values of $\epsilon^{AB/R}$ and β^{AB} for CPA and $\epsilon^{AB/kb}$ and K^{AB} for PC-SAFT, which values present inversely proportional relationships, thus, generating compensation in associative terms. This fact happens when the Δ^{AiBj} assumes sufficiently high values, and the results of interest in this paper are not sensitive to the associative parameters.

Another vital piece of information to be added to the Aspen plus is the C_p^{gi} , which was calculated from experimental data from C_p^{liq} , while C_p^{res} was calculated using the adjusted parameters. Thus, the parameters for the C_p^{gi} function of the mentioned software was obtained. The parameters applied can be found in the

Supplementary Material of this present work for the respective thermodynamic models.

Properties calculations of pure ILs

It was analyzed that the non-association, the choice of the scheme, and the variation of the associative parameter did not influence the fit of the pure [EMIM][TfO] data using the SRK and CPA models, thus proving freedom for the model selection. Furthermore, it investigated the contribution of the term, and the selection of the associative scheme for the CPA EoS showed no differences in the density adjustment, leading to an AARD of 0.54%, as shown in Table 4.

Table 4. Absolute Average Relative Deviation (AARD) in percentage for thermophysical properties for SRK, CPA, and PC-SAFT models for [EMIM][TfO] and [OMIM][NTf₂].

		[EMIM][TfO]										
AARD (%)	Density						Speed of sound					
	SRK	NA*	1A	2B	3B	4C	SRK	NA*	1A	2B	3B	4C
SRK	0.54						1.95					
CPA		0.54	0.54	0.54	0.54	0.54		1.95	1.95	1.95	1.95	1.93
PC-SAFT		0.32	0.29	0.25	0.25	0.16		0.84	0.70	0.61	0.60	0.53
		[OMIM][NTf ₂]										
AARD (%)	Density						Speed of sound					
	SRK	NA*	1A	2B	3B	4C	SRK	NA*	1A	2B	3B	4C
SRK	0.24						4.02					
CPA		0.24	0.24	0.24	0.24	0.25		4.05	4.09	4.09	4.09	4.16
PC-SAFT		0.20	0.17	0.13	0.13	0.07		1.00	0.93	0.87	0.87	0.75

In addition, analogously, the variation of the associative term demonstrates no difference in the adjustment of the density and speed of sound data as a function of temperature for the [EMIM][TfO] using the SRK, non-associative and associative CPA with 2B scheme, which presented AARD of 0.54% and 1.95% for density and speed of sound, respectively.

In agreement with the CPA EoS, the PC-SAFT did not show divergence in the selection of the associative parameter, thus allowing a wide choice of the associative parameter. Nonetheless, in the PC-SAFT EoS, the choice of the associative scheme influenced the adjustment of the pure component, in which there was a decrease in the AARD of the associative PC-SAFT compared to the non-associative one, in which the AARDs for density were 0.32 % for non-associative, 0.29% for 1A scheme, 0.25% 2B and 3B schemes, and 0.16% for 4C scheme, while for the speed of sound, the AARD was 0.84% for the non-associative PC-SAFT, 0.70% for 1A scheme, 0.61% 2B scheme, 0.60% for 3B scheme and 0.53% for the 4C scheme. Therefore, for the PC-SAFT EoS, the 4C scheme was the one that presented the best fit for the thermophysical properties of density and speed of sound due to the AARDs that were 0.16% and 0.53%, respectively.

Table 4 also presents the deviation for the density and speed of sound of the ionic liquid [OMIM][NTf₂]

using SRK, CPA, and PC-SAFT models. Thus, from Table 4, it was found that for the density curve, there was no difference between SRK and non-associative and associative CPA EoS, which presented an AARD of 0.24%. However, regarding the speed of sound, the SRK model presented the lowest AARD, concluding that the contribution of the associative term did not improve the fit of the mentioned curve; thus, the lowest AARD was 4.02% for the SRK model.

On the other hand, PC-SAFT showed significant improvements in the adjustment of density curves. The non-associative PC-SAFT obtained a reduction of 0.04% compared to SRK and CPA. Moreover, PC-SAFT, with the 4C scheme in the associative term, led to the lowest AARD.

Finally, as shown for the other ionic liquid, the C_p^{liq} was adjusted from the calculation of the C_p^{res} of the respective equations of state to inform the C_p^{gi} in the Aspen plus, causing it to be adjusted the C_p^{liq} . Further details and information on the properties and parameters, and associative schemes are present in the Supplementary Material.

GLE results

Methane + [EMIM][TfO] equilibria results

The solubility calculation was carried out to

evaluate the thermodynamic models in predicting the solubility curves of methane, the main component of natural gas, in ILs so that it was possible to select the best thermodynamic model for this application.

At first, the solubility curves will be presented with the SRK and CPA ($\beta^{AB}=1$ for the associative ones) models in a predictive way, i.e., the binary interaction parameter equals zero ($k_{ij}=0$). In this way, Figure 1(a)

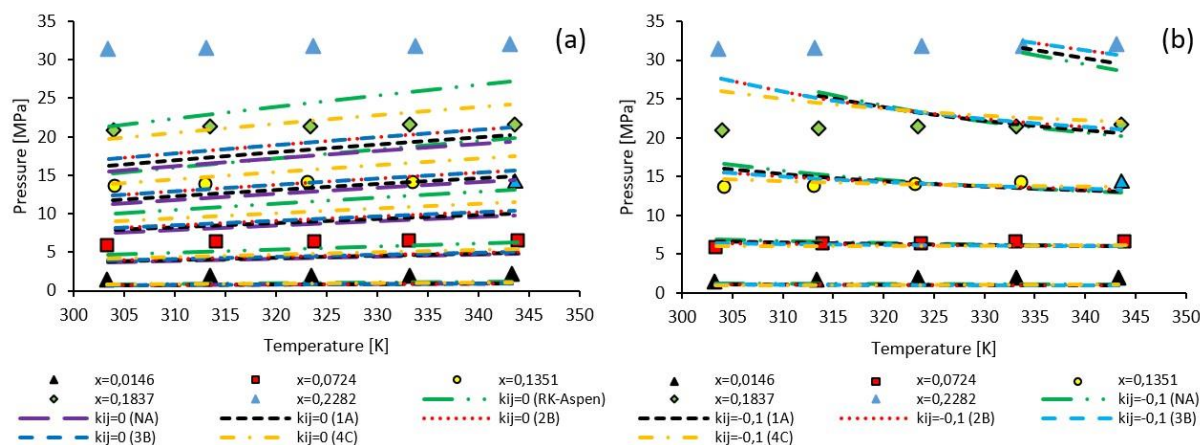


Figure 1. *P-T* results for CH₄ and [EMIM][TfO]: (a) Results with $k_{ij}=0$ for SRK and CPA for different associative schemes; (b) Results with $k_{ij}=-0,1$ for non-associative PC-SAFT and PC-SAFT for different associative schemes; Experimental data from Lee [32].

The AARD for SRK, CPA, and PC-SAFT models are included in the supplementary material. Thus, when analyzing, with $k_{ij}=0$, the SRK model showed the lowest AARD, 23.02%, which showed that the association for the IL did not enhance the prediction of the solubility of methane.

The equilibrium calculation outside the Aspen plus software allowed the convergence of equilibrium in conditions where there was no convergence in the simulator to the PC-SAFT EoS. The pressure values found were way higher than the experimental values. It is important to study other systems for which equilibrium data with other hydrocarbons are available, so a more comprehensive analysis can be conducted.

A regression of the binary interaction parameters was performed using two parameters (2p). Nevertheless, it is worth noting that concerning the SRK model, two binary interaction parameters were adjusted, one for the attractive parameter and another for the covolume parameter simultaneously, so for the SRK model, 2p represents the adjusted parameters $k_{a_{ij}}^0$ and $k_{b_{ij}}^0$, while 4p represents the adjusted parameters $k_{a_{ij}}^0$, $k_{a_{ij}}^1$, $k_{b_{ij}}^0$, and $k_{b_{ij}}^1$. In this way, the results were shown to improve significantly.

The models with two parameters showed AARD of 11.50% for SRK, 8.99% for CPA (NA), 9.12% for CPA (1A), 11.40% for PC-SAFT (NA), and 12.13% for PC-SAFT (1A), concluding that the CPA (NA) model presented the best fit with two parameters.

shows far the predictive results were in comparison with the experimental data. Additionally, another model to be analyzed was PC-SAFT ($K^{AB}=1$ for associations), but initially, tests were performed with $k_{ij}=-0,1$, as shown in Figure 1(b). It is because it was not possible to converge the vapor-liquid equilibrium in the simulator with $k_{ij}=0$. In this way, an empirical adjustment was made for the binary interaction parameter.

Nevertheless, when considering the SRK model with four parameters, i.e., the parameter of binary interaction as a function of temperature for the attractive and covolume parameters, the latter presented the lowest AARD of 8.54%. More details of the AARD are in the Supplementary Material.

Carbon dioxide + ILs equilibria results

The solubility curves for CO₂ and [EMIM][TfO] are shown using the SRK model, presenting predictive results and the fit of the binary interaction parameters for the attractive and covolume parameters. As explained for methane, the adjustments 2p and 4p were performed for the parameter k_{ij} . Thus, Figure 2 shows a decrease in AARD by adding binary interaction parameters as a function of temperature, i.e., with four parameters.

The solubility curves for CO₂ and [EMIM][TfO] are shown using the CPA and PC-SAFT EoS to demonstrate that the variation of the associative parameter did not cause changes in the CPA and PC-SAFT curves, which can be verified in Figure 3(a) and Figure 3(b), respectively.

To improve the fits of the solubility curves and, thus, represent the experimental data more accurately, the binary interaction parameters of the CPA and PC-SAFT EoS were adjusted based on the equilibrium data of CO₂ and [EMIM][TfO]. Thus, the curves with 2 regressed parameters are shown in Figure 3(c) and

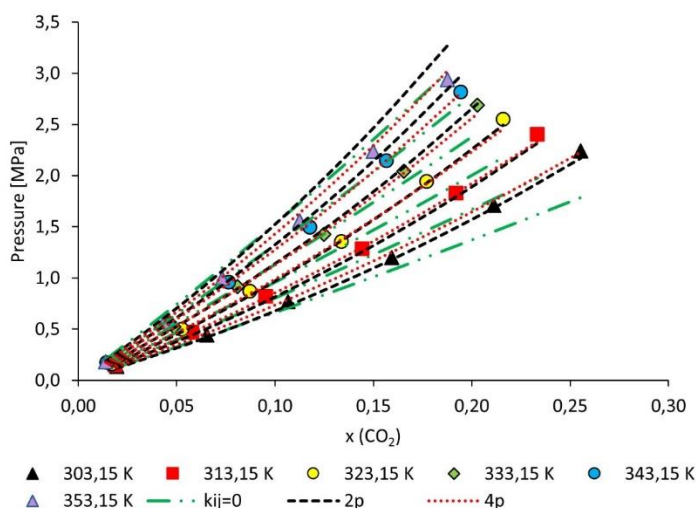


Figure 2. *P*-*x* results for CO₂ and [EMIM][TfO] using SRK model with *k_{ij}*=0, 2*p* and 4*p*. Experimental data from Nematpour *et al.* [14].

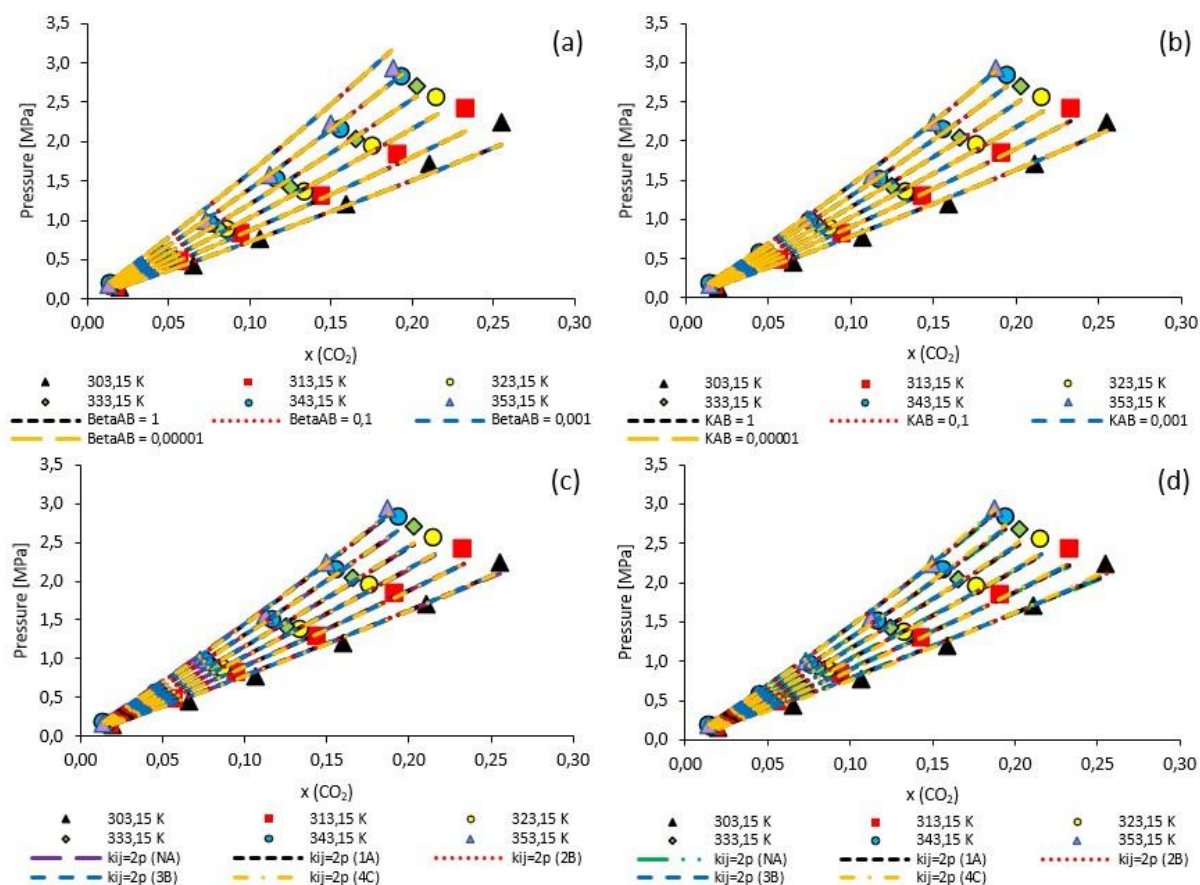


Figure 3. *P*-*x* results for CO₂ and [EMIM][TfO]: (a) CPA with different associative parameters (β^{AB}) for the 2B scheme with *k_{ij}*=0; (b) PC-SAFT with different associative parameters (K^{AB}) for the 2B scheme with *k_{ij}*=0; (c) Results for CPA EoS with *k_{ij}*=2*p* for different associative schemes; (d) Results for PC-SAFT EoS with *k_{ij}*=2*p* for different associative schemes. Experimental data from Nematpour *et al.* [14].

Figure 3(d), respectively, and in the Supplementary Material are presented the AARDs.

For two parameters, the SRK model had AARD of 4.69%, non-associative CPA was 5.81%, CPA (1A) was

5.62%, CPA (2B) and (3B) were 5.43%, and CPA(4C) of 5.07%, while for the non-associative PC-SAFT, it was 5.95%, PC-SAFT (1A) was 5.22%, PC-SAFT (2B) and (3B) was 4.54%, and PC-SAFT (4C) was 3.37% for the same situation. Thus, analyzing the same set of

parameters, the PC-SAFT (4C) EoS had the lowest AARD of 3.37%. On the other hand, when considering the SRK model with four parameters lower deviation is obtained, resulting in an AARD of 2.17%.

For the [OMIM][NTf₂] ionic liquid, we started by performing the solubility curves for the SRK and the CPA (NA) models with $k_{ij}=0$, which shows a limitation of the EoS in accurately predicting the solubility curves.

After that, adjustments were made to the binary interaction parameters based on phase equilibrium data, in which a significant decrease in AARD was obtained. Thus, adjustments were made to the SRK model with 2 and 4 parameters. And as exposed for the previous ionic liquid, the adjustments made with four parameters significantly reduced the AARD, causing a decrease from 9.71% to 1.12%. It happens because it also uses a binary interaction parameter for the covolume parameter (b), making it a quadratic mixing rule different from the linear mixing rule presented in the CPA EoS.

Furthermore, analyzes were performed using the associative CPA and PC-SAFT models, in which, for this ionic liquid, scheme 1A was the one that presented the best predictive result, being then estimated for the

parameter k_{ij} as a function of temperature ($k_{ij}=2p$). Therefore, in Figure 4, the curves for these models are presented.

In conclusion, the predictive PC-SAFT model showed an excellent fit for the solubility of CO₂ in [OMIM][NTf₂]. With the regression of the binary parameters for the same amount (2 parameters) from the solubility data, the PC-SAFT (4C) model showed the lowest AARD. However, when considering the SRK model with four parameters, it presented the lowest AARD of 1.12%, as shown in the Supplementary Material.

Kontogeorgis and Folas [42] consider induced association (solvation) relevant in mixtures of CO₂+H₂O or CO₂ with methanol or ethanol. However, this application is not considered when considering higher molecular weight alcohols. Mixtures of CO₂ or H₂S and glycols could be well correlated without the need to explicitly explain solvation, for example, for the CO₂-MEG and CO₂-DEG systems, as well as for the CO₂-H₂O-MEG multicomponent mixture. For this reason, since the ILs are not present in the vapor phase, and good results were obtained with the mixtures, there was no interest in adding another parameter.

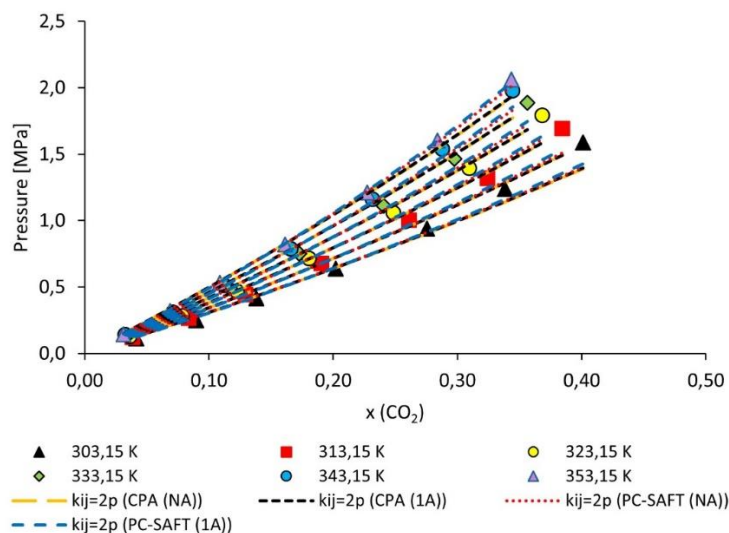


Figure 4. P - x results for CO₂ and [OMIM][NTf₂] for CPA and PC-SAFT EoS with $k_{ij}=2p$. Experimental data from Jalili *et al.* [13].

Hydrogen sulfide + ILs equilibria results

Like the presented solubility curves of [EMIM][TfO] and CO₂, the addition of the associative parameter influenced the prediction of the solubility of hydrogen sulfide in the IL, which can be seen in Figure 5(a). Moreover, the same similarity to the previous case can be observed, in which there is no variation in the solubility prediction with the CPA and PC-SAFT EoS with variations in the association parameter.

Differently from what was shown for CO₂

solubility, [EMIM][TfO] using CPA (NA) presented significant errors compared to SRK, and this can be explained by the fact that SRK is not using association for any of the components. At the same time, the CPA was applied with non-association for IL and 3B scheme for H₂S, which leads to the conclusion that in addition to a good parameterization of the IL, the relationship with the association of the other component must be jointly analyzed. Besides, it was important to verify that the addition of associative terms to IL contributed to a better prediction of the solubility curve, presenting

better-calculated values for low H_2S concentrations and higher deviations for higher compositions.

It is possible to observe in Figure 5(b), differently from what is presented for the CPA, that the non-

associative PC-SAFT presents a good prediction of the solubility of hydrogen sulfide in the ionic liquid.

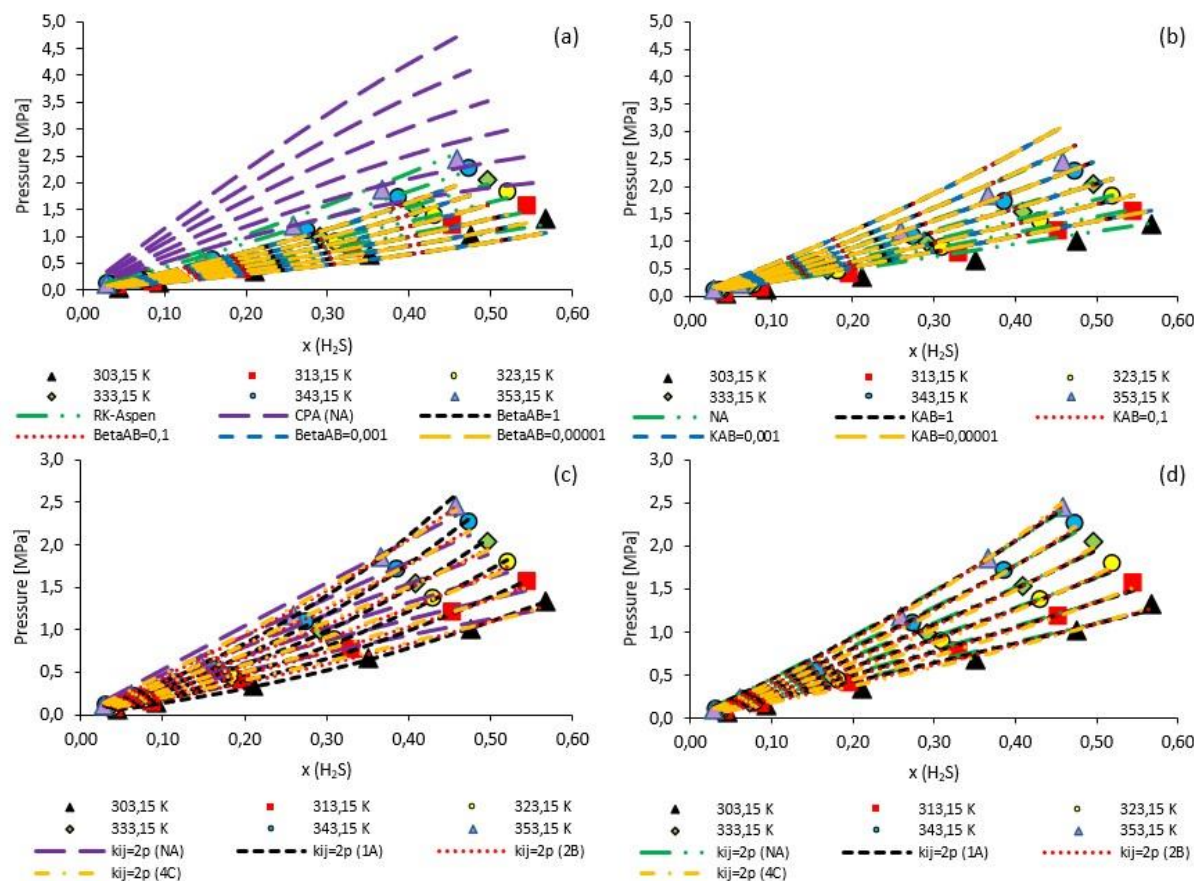


Figure 5. P - x results for H_2S and $[EMIM][TfO]$: (a) Non-associative and associative CPA with different associative parameters (β^{AB}) for the 2B scheme with $k_{ij}=0$; (b) Non-associative and associative PC-SAFT EoS with different associative parameters (K^{AB}) for the 2B scheme with $k_{ij}=0$; (c) Non-associative and associative CPA with different associative schemes with $k_{ij}=2p$; (d) Non-associative and associative PC-SAFT with different associative schemes with $k_{ij}=2p$. Experimental data from Nematpour *et al.* [14].

As previously presented for the mixtures of IL (3B) with CO_2 and CH_4 , which were non-associative, it was noticed there were no differences between 2B and 3B schemes. Nonetheless, when analyzing the equilibrium of IL (3B) with H_2S (3B scheme for CPA and 2B scheme for PC-SAFT), it was noticed that the scheme was limited for the prediction of solubility, leading to erroneous equilibrium results. In this context, the 3B associative scheme for ILs has become inappropriate for applications with H_2S . The Aspen plus could not perform the data regression for the CPA EoS, but it was able to perform it for the PC-SAFT. Nevertheless, the results presented were incoherent, thus discarding the possibility of adjusting the parameter k_{ij} for the $[EMIM][TfO]$ (3B). Further details about that scheme are present in the Supplementary Material.

For the CPA and PC-SAFT EoS, data regressions were performed for k_{ij} as a function of temperature for

the non-associative and 1A, 2B, and 4C schemes since the 3B scheme has already been evaluated. Therefore, there were significant improvements in the solubility curves from the reduction of the AARD present in the Supplementary Material and verified in Figures 5(c) and 5(d), respectively.

The AARD decreased with the adjustment of the binary interaction parameter, including for the CPA (NA), which presented an AARD of 32.28% (for $k_{ij}=0$, the deviation was 160.3%). This result showed the impact of modeling H_2S as an associative compound, as in the SRK model, there was no association for H_2S , leading to a reduction in AARD from 160.3% to 18.55%, which was lowered to 1.74%, comparing the predictive with the parameter $k_{ij}=4p$ modes. The other associative CPA schemes showed improvements, in which scheme 1A showed a significant improvement from 20.05% of the predictive to 3.54% for the $k_{ij}=2p$. The 2B scheme

had 14.39% for the predictive model and 10.48% for the 2p model, and the 4C scheme had 31.99% for the predictive and 15.04% for the $k_{ij}=2p$ model.

In the PC-SAFT EoS, the non-association for IL presented an AARD of 26.49% for the predictive and 18.17% for the model, with k_{ij} adjusted as a function of temperature, i.e., $k_{ij}=2p$. PC-SAFT (1A) had 29.20% for the predictive and 15.08% for the model with $k_{ij}=2p$, PC-SAFT 2B had 42.68% for the predictive and 11.87% for the model with $k_{ij}=2p$, and, finally, the associative 4C scheme showed improvement from 64.83% for the predictive model to 6.56% for the model with $k_{ij}=2p$.

Figure 6 shows the solubility curves for H₂S in

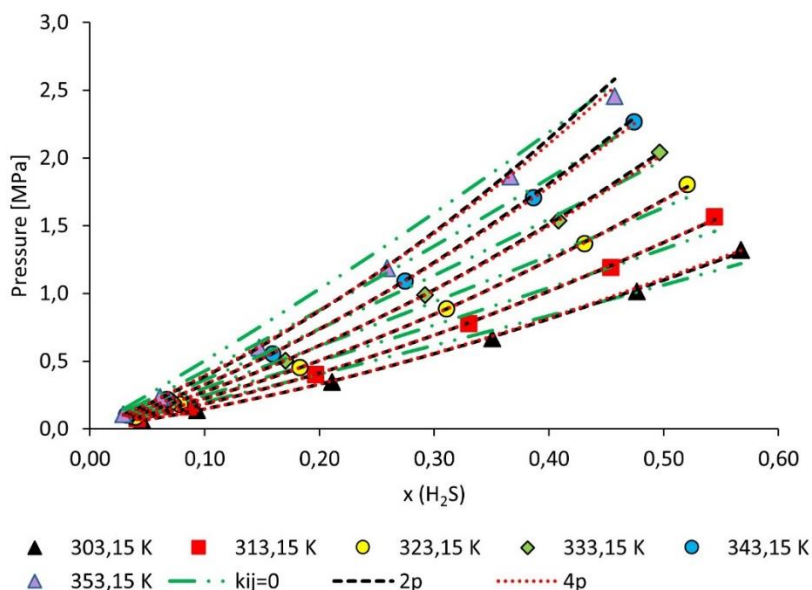


Figure 6. *P-x* results for H₂S and [EMIM][TfO] using SRK model with $k_{ij}=0$, 2p and 4p. Experimental data from Nematpour *et al.* [14].

SRK model adjusted as a function of temperature for the attractive parameter and the covolume parameter for the H₂S solubility curves in [EMIM][TfO], it presented a better fit with AARD of 1.74%.

Among the models analyzed for the [OMIM][NTf₂], the CPA model (2B) showed the lowest AARD for the predictive models, resulting in an AARD of 5.67%. In contrast, the predictive models SRK, CPA (NA), PC-SAFT (NA), and PC-SAFT (2B) showed AARD of 57.51%, 183.69%, 6.78%, and 9.54%, respectively. Furthermore, regressions of the binary interaction parameters of the models mentioned above were performed to improve the solubility curves, thus contributing to a decrease in the AARD.

Analogously to the present for the previous IL, the comparison between the results for the SRK and CPA (NA) models shows that considering H₂S as associative led to much worse predictive results for CPA (NA), however considering H₂S as associative and IL as associative 2B scheme led to better predictive results

[EMIM][TfO] using the SRK model to verify the effect of the adjustment of the binary interaction parameters for the attractive and covolume parameters.

Figure 6 shows better adjustments with the addition of binary interaction parameters, and for the predictive model, the AARD was 18.55%, while for the parameter k_{ij} with 2p and 4p, it was 2.16% and 1.74%, respectively, showing that the adjustment of the parameter k_{ij} both as a function of temperature and constant values resulted in satisfactory adjustments.

Thus, when evaluating the values of k_{ij} adjusted for 2p, the CPA model (1A) presented the lowest AARD of 3.54%. On the other hand, when considering the

for CPA than SRK. These results underscore the importance of optimal parameterization for each substance to be designed to work properly together with the other substances in the mixture.

The adjusted SRK model presented AARD for 2p and 4p of 9.53% and 3.51%, respectively, showing that with the adjustment of the binary parameters as a function of temperature, the SRK model was able to represent well the equilibrium data, reducing the predictive AARD from 57.51% to 3.51%, as shown in Figure 7(a).

The CPA (NA) presented an AARD of 11.77%, and the PC-SAFT (NA) indicated a deviation of 5.60%, with two adjusted parameters. Furthermore, for the associative models, CPA and PC-SAFT were analyzed with the same associative schemes, showing that the CPA (2B) had the lowest AARD of 1.81%. The AARD of the PC-SAFT (2B) was 3.48% for two adjusted parameters. These results can be seen in the Supplementary Material.

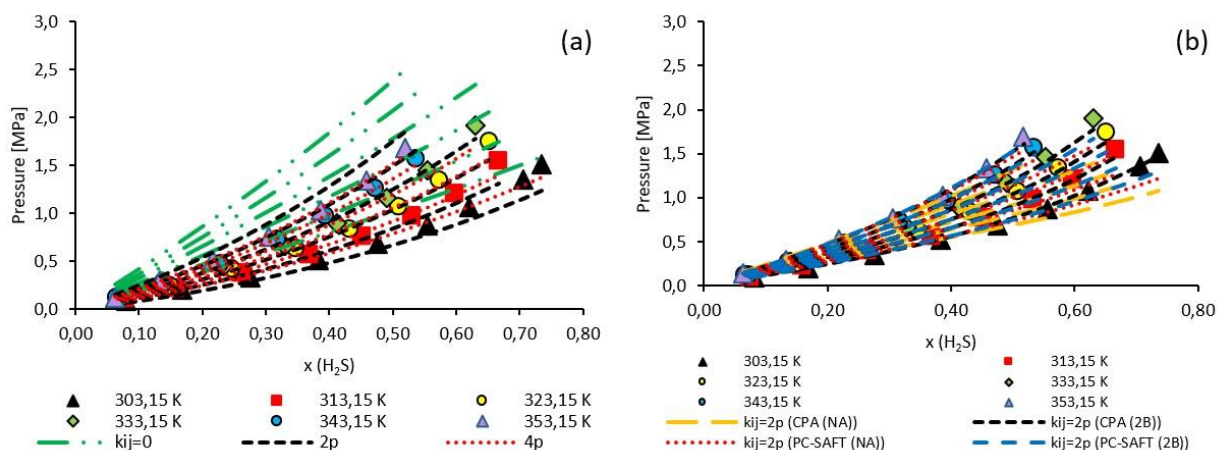


Figure 7. P - x results for H_2S and $[\text{OMIM}][\text{NTf}_2]$: (a) Results for SRK model with $k_{ij}=0$, 2p and 4p; (b) Results for SRK, CPA, and PC-SAFT models with $k_{ij}=2p$. Experimental data from Jalili *et al.* [13].

In this way, and as shown in Figure 7(b), the models with adjustments of the binary interaction parameter became efficient in correlating the solubility curves. Nonetheless, the CPA model (2B) presented the lowest AARD.

In conclusion to the cases studied, Table 5 summarizes the best models for the cases previously studied using predictive models ($k_{ij}=0$), and with binary interaction parameters with one and two regressed

parameters.

When considering the 4p SRK model, this model showed smaller deviations in all cases, except for the solubility of H_2S in $[\text{OMIM}][\text{NTf}_2]$, for which the CPA (2B) EoS was the best. Nevertheless, it is worth noting that the SRK model contains more binary parameters than the other models since the covolume parameter of the mixture was adjusted simultaneously.

Table 5. Summary of the best models for ILs with methane and acid gases, in a predictive way ($k_{ij}=0$) and with the correlation of binary interaction parameters

Components	[EMIM][TfO]		
	$k_{ij}=0$	1p	2p
CH_4	SRK	CPA (NA)	CPA (NA)
CO_2	PC-SAFT (2B)	PC-SAFT (4C)	PC-SAFT (4C)
H_2S	CPA (2B)	CPA (1A)	SRK
Components	[OMIM][NTf ₂]		
	$k_{ij}=0$	1p	2p
CO_2	PC-SAFT (1A)	PC-SAFT (1A)	PC-SAFT (4C)
H_2S	CPA (2B)	CPA (2B)	CPA (2B)

CONCLUSION

The SRK model expressed the same behavior as the CPA EoS for the correlation of properties of pure ILs ($[\text{EMIM}][\text{TfO}]$ and $[\text{OMIM}][\text{NTf}_2]$). Nonetheless, for PC-SAFT, the associative effect corroborated the absolute Average Relative Deviation (AARD) decrease in the analyzed properties.

For the $[\text{EMIM}][\text{TfO}]$ and $[\text{OMIM}][\text{NTf}_2]$, the PC-SAFT (4C) showed the lowest AARD for density and speed of sound, thus presenting the best fit for both ILs.

For $[\text{EMIM}][\text{TfO}]$ and the other mentioned components, when adjusting the parameter k_{ij} with 2 parameters, the models that presented the lowest AARD for the system $[\text{EMIM}][\text{TfO}]/\text{CH}_4$, $[\text{EMIM}][\text{TfO}]/\text{CO}_2$, and $[\text{EMIM}][\text{TfO}]/\text{H}_2\text{S}$ were CPA (NA), PC-SAFT (4C), and SRK, respectively. Furthermore, $[\text{OMIM}][\text{NTf}_2]$ was analyzed with CO_2 and

H_2S with two parameters, and the best models were PC-SAFT (4C) and CPA (2B), respectively.

This present study enabled the thermodynamic modeling of ILs from density and speed of sound data for the SRK, CPA, and PC-SAFT EoS. In addition, this study conceded the addition of ILs in the Aspen plus process simulator. As a result, the data of pure components and mixtures can be explored, allowing their applicability in the simulation of removing acid gases from natural gas.

ACKNOWLEDGEMENT

This work was supported by Coordenação de Aperfeiçoamento de Pessoal de Nível Superior - Brazil (CAPES) under PROC. 88887.633974/2021-00; Fundação de Amparo à Pesquisa do Estado da Bahia

(FAPESB/SECTI/Bahia/Brazil) under Project APP0075/2016 and Conselho Nacional de Desenvolvimento Científico e Tecnológico (CNPq/Brazil) through Grant 303089/2019-9. In addition, the authors acknowledge the financial support provided by Programa de Recursos Humanos da Agência Nacional do Petróleo, Gás Natural e Biocombustíveis - PRH-ANP.

NOMENCLATURE

[BMIM][PF ₆]	1-butyl-3-methylimidazolium hexafluorophosphate
[EMIM][FAP]	1-ethyl-3-methylimidazolium Tris(pentafluoroethyl) trifluorophosphate
[EMIM][TfO]	1-ethyl-3-methylimidazolium trifluoromethanesulfonate
[OMIM][NTf ₂]	1-octyl-3-methylimidazolium bis(trifluoromethylsulfonyl) imide
AARD	Absolute Average Relative Deviation
CH ₄	Methane
CO ₂	Carbon dioxide
CPA	Cubic-Plus-Association
DEG	Diethylene glycol
EoS	Equation of state
H ₂ O	Water
H ₂ S	Hydrogen sulfide
IL	Ionic liquid
MEG	(Mono)ethylene glycol
NA	Non-associative
N ₂	Nitrogen
PC-SAFT	Perturbed-Chain Statistical Associating Fluid Theory
SRK	Soave-Redlich-Kwong
LLE	Liquid-liquid equilibrium
GLE	Gas-liquid equilibria (GLE)

LIST OF SYMBOLS

a_0	Modified alpha function parameter of SRK equation
$a(T)$	Attractive parameter as a function of temperature
\tilde{a}^{assoc}	Associative Helmholtz energy
\tilde{a}^{chain}	Chain Helmholtz energy
\tilde{a}^{disp}	Dispersive Helmholtz energy
\tilde{a}^{hs}	Hard-sphere Helmholtz energy

\tilde{a}^{res}	Residual Helmholtz energy
a	Attractive mixing parameter
b	Covolume mixing parameter
b_{CPA}	Covolume parameter of CPA
β^{AB}	Association volume of interaction between sites A and B
c_1	Modified alpha function parameter of the SRK equation
C_{1i}	Aspen plus polynomial equations constants
C_{2i}	Aspen plus polynomial equations constants
C_{3i}	Aspen plus polynomial equations constants
C_{4i}	Aspen plus polynomial equations constants
C_{5i}	Aspen plus polynomial equations constants
C_p^{ig}	Ideal gas heat capacity at constant pressure
C_p^{liq}	Liquid heat capacity at constant pressure
C_p^{res}	Residual heat capacity at constant pressure
C_v^{res}	Residual heat capacity at constant volume
δ	Experimental uncertainty
$\Delta^{A_iB_j}$	Strength of interaction between sites A and B
ϵ_{ij}	Segment energy parameter i and j
ϵ^{AB}	Association energy of interaction between sites A and B
F_{obj}	Objective function
g	Radial distribution function
k_B	Boltzmann's constant
K^{AB}	Parameter of the effective associative volume of PC-SAFT between site A and site B
k_{ij}	Binary interaction
k_{aij}^0	Parameter 0 of binary interaction of component i and j for parameter a of SRK
k_{aij}^1	Parameter 1 of binary interaction of component i and j for parameter a of SRK
k_{bij}^0	Parameter 0 of binary interaction of component i and j for parameter b of SRK
k_{bij}^1	Parameter 1 of binary interaction of component i and j for parameter b of SRK
k_{ij}^0	Parameter 0 of binary interaction of components i and j for CPA and PC-SAFT models
k_{ij}^1	Parameter 1 of binary interaction of components i and j for CPA and PC-SAFT models
m_i	Segment number i
m_m	"Monomer" parameter
MM	Molar mass
n	Total number of elements

σ_i	Segment diameter i
Ω_A	Parameter of the SRK EoS, $\Omega_A = 0.42748$
Ω_B	Parameter of the SRK EoS, $\Omega_B = 0.08664$
P	Pressure
P_{Ant}^v	Antoine's pressure
P_c^*	Critical pressure adapted from SRK
P_{cm}	"monomer" critical pressure
ρ	Density
ρ_i^{cal}	Calculated density of component i
ρ_i^{exp}	Experimental density of component i
R	Gas constant
T	Temperature
T_c^*	Critical temperature adapted from SRK
T_{cm}	"monomer" critical temperature
T_{ref}	Reference temperature, $T_{ref} = 298.15$ K
u_i^{cal}	Calculated density of component i
u_i^{exp}	Experimental density of component i
V_m	Mole volume
v_i^{exp}	Experimental variable
v_i^{cal}	Calculated variable
ω	Acentric factor
X_{A_i}	Mole fraction of the compound not bonded at site A
x_i	Mole fraction of component i
x_j	Mole fraction of component j

REFERENCES

- [1] I. Iliuta, F. Iarachi, *Int. J. Greenhouse Gas Control* 79 (2018) 1–13. <https://doi.org/10.1016/j.ijggc.2018.09.016>.
- [2] J. Carrol, *Natural Gas Hydrates: A Guide for Engineers*, 4. Ed., Gulf Professional Publishing (2020) p. 377. ISBN: 978-0-12-821771-9.
- [3] A. Haghtalab, A. Afsharpour, *Fluid Phase Equilib.* 406 (2015) 10–20. <https://doi.org/10.1016/j.fluid.2015.08.001>.
- [4] J. Haider, S. Saeed, M.A. Qyyum, B. Kazmi, R. Ahmad, A. Muhammad, M. Lee, *Renewable Sustainable Energy Rev.* 123 (2020) 109771. <https://doi.org/10.1016/j.rser.2020.109771>.
- [5] R. Santiago, J. Lemus, A.X. Outomuro, J. Bedia, J. Palomar, *Sep. Purif. Technol.* 233 (2020) 116050. <https://doi.org/10.1016/j.seppur.2019.116050>.
- [6] G. Yu, C. Dai, L. Wu, Z. Lei, *Energy Fuels* 31 (2017) 1429–1439. <https://doi.org/10.1016/j.fuel.2018.08.152>.
- [7] S.E. Sanni, O. Agboola, O. Fagbiele, E.O. Yusuf, M.E. Emeterere, *Egypt. J. Pet.* 29 (2020) 83–94. <https://doi.org/10.1016/j.ejpe.2019.11.003>.
- [8] T.E. Akinola, E. Oko, M. Wang, *Fuel* 236 (2019) 135–146. <https://doi.org/10.1016/j.fuel.2018.08.152>.
- [9] K. Huang, X.-M. Zhang, Y. Xu, Y.-T. Wu, X.-B. Hu, *AIChE J.* 60 (2014) 4232–4240. <https://doi.org/10.1002/aic.14634>.
- [10] S. Zhang, J. Zhang, Y. Zhang, Y. Deng, *Chem. Rev.* 117 (2017) 6755–6833. <https://doi.org/10.1021/acs.chemrev.6b00509>.
- [11] S.K. Singh, *Int. J. Biol. Macromol.* 132 (2019) 265–277. <https://doi.org/10.1016/j.ijbiomac.2019.03.182>.
- [12] M. Freemantle, *Chem. Eng. News* 78 (2000) 37–50. <https://doi.org/10.1021/cen-v078n020.p037>.
- [13] A.H. Jalili, M. Safavi, C. Ghotbi, A. Mehdizadeh, M. Hosseini-Jenab, V. Taghikhani, *J. Phys. Chem. B* 116 (2012) 2758–2774. <https://doi.org/10.1021/jp2075572>.
- [14] M. Nematpour, A.H. Jalili, C. Ghotbi, D. Rashtchian, *J. Nat. Gas Sci. Eng.* 30 (2016) 583–591. <https://doi.org/10.1016/j.jngse.2016.02.006>.
- [15] A.K. Jana, *Process simulation and control using AspenTM*, PHI Learning Private Limited, (2009) p. 317. ISBN: 978-81-203-3659-9.
- [16] A.M. Law, W. D. Kelton, *Simulation modeling & analysis*, 2. ed., McGraw-Hill International editions, (1991) p. 672. ISBN-13: 978-0070366985.
- [17] A.I. Papadopoulos, I. Tsvintzelis, P. Linke, P. Seferlis, in *Elsevier Reference Module in Chemistry, Molecular Sciences and Chemical Engineering*, Elsevier (2018) <https://doi.org/10.1016/B978-0-12-409547-2.14342-2>.
- [18] L.F. Cardona, J.O. Valderrama, *J. Mol. Liq.* 317 (2020) 113926. <https://doi.org/10.1016/j.molliq.2020.113926>.
- [19] G. Soave, *Chem. Eng. Sci.* 27 (1972) 1197–1203. [https://doi.org/10.1016/0009-2509\(72\)80096-4](https://doi.org/10.1016/0009-2509(72)80096-4).
- [20] M.S. Graboski, T.E. Daubert, *Ind. Eng. Chem. Process Des. Dev.* 18 (1979) 300–306. <https://doi.org/10.1021/i260070a022>.
- [21] P.M. Mathias, *Ind. Eng. Chem. Process Des. Dev.* 22 (1983) 385–391. <https://doi.org/10.1021/i200022a008>.
- [22] G.M. Kontogeorgis, E.C. Voutsas, I. V. Yakoumis, D.P. Tassios, *Ind. Eng. Chem. Res.* 35 (1996) 4310–4318. <https://doi.org/10.1021/ie9600203>.
- [23] G.M. Kontogeorgis, M.L. Michelsen, G.K. Folas, S. Derawi, N. Von Solms, E.H. Stenby, *Ind. Eng. Chem. Res.* 45 (2006) 4855–4868. <https://doi.org/10.1021/ie051305v>.
- [24] S. Huang, M. Radosz, *Ind. Eng. Chem. Res.* 29 (1990) 2284–2294. <https://doi.org/10.1021/ie00107a014>.
- [25] J. Gross, G. Sadowski, *Ind. Eng. Chem. Res.* 40 (2001) 1244–1260. <https://doi.org/10.1021/ie0003887>.
- [26] S.F. Baygi, H. Pahlavanzadeh, *Chem. Eng. Res. Des.* 93 (2015) 789–799. <https://doi.org/10.1016/j.cherd.2014.07.017>.
- [27] J. Gross, G. Sadowski, *Ind. Eng. Chem. Res.* 41 (2002) 5510–5515. <https://doi.org/10.1021/ie010954d>.
- [28] W.G. Chapman, K.E. Gubbins, G. Jackson, M. Radosz, *Ind. Eng. Chem. Res.* 29 (1990) 1709–1721. <https://doi.org/10.1021/ie00104a021>.
- [29] J. Gross, O. Spuhl, F. Tumakaka, G. Sadowski, *Ind. Eng. Chem. Res.* 42 (2003) 1266–1274. <https://doi.org/10.1021/ie020509y>.
- [30] M. Lorenzo, R.A. Reis, S. Mattedi, M.L.L. Paredes, *Fluid Phase Equilib.* 479 (2019) 85–98. <https://doi.org/10.1016/j.fluid.2018.09.010>.
- [31] E. Vercher, A.V. Orçillés, P.J. Miguel, A. Martínez-

- Andreu, J. Chem. Eng. Data 52 (2007) 1468–1482. <https://doi.org/10.1021/je7001804>.
- [32] B-C. Lee, Korean J. Chem. Eng. 54 (2016) 213–222. <https://doi.org/10.9713/kcer.2016.54.2.213>.
- [33] E. Zorębski, M. Geppert-Rybczńska, M. Zorębski, J. Phys. Chem. B 117 (2013) 3867–3876. <https://doi.org/10.1021/jp400662w>.
- [34] J. Kennedy, R. Eberhart, Proc. ICNN'95 Int. Conf. N. Net. (1995) 1942–1948. <https://doi.org/10.1109/ICNN.1995.488968>.
- [35] J.A. Nelder, R. Mead, Comp. J. 7 (1965) 308–313. <https://doi.org/10.1093/comjnl/7.4.308>.
- [36] R.J. Topliss, D. Dimitrelis, J. M. Prausnitz, Comput. Chem. Eng. 12 (1988) 483–489. [https://doi.org/10.1016/0098-1354\(88\)85067-1](https://doi.org/10.1016/0098-1354(88)85067-1).
- [37] Aspen plus 2019 - Aspen Technology Inc. - USA.
- [38] I. Tsvintzelis, G.M. Kontogeorgis, M.L. Michelsen, E.H. Stenby, AIChE J. 56 (2010) 2965–2982. <https://doi.org/10.1002/aic.12207>.
- [39] L. Ruffine, P. Mougin, A. Barreau, Ind. Eng. Chem. Res. 45 (2006) 7688–7699. <https://doi.org/10.1021/ie0603417>.
- [40] X. Tang, J. Gross, Fluid Phase Equilib. 293 (2010) 11–21. <https://doi.org/10.1016/j.fluid.2010.02.004>.
- [41] Nist, NIST Livro de Química na Web, <https://webbook.nist.gov/chemistry/> [Accessed 09 august 2021].
- [42] G.M. Kontogeorgis, G.K. Folas, Thermodynamic Models for Industrial Applications, 1. Ed., John Wiley & Sons Inc(2010) p. 710. ISBN: 978-0-470-69726-9

LUCAS OLIVEIRA CARDOSO¹
BRUNO SANTOS
CONCEIÇÃO¹
MÁRCIO LUIS LYRA
PAREDES²
SILVANA MATTEDI¹

¹Chemical Engineering Graduate
Program (UFBA/UNIFACS),
Polytechnic School, Federal
University of Bahia, Salvador,
BA, Brazil

²Chemical Engineering Graduate
Program, Rio de Janeiro State
University, Rio de Janeiro, RJ,
Brazil

NAUČNI RAD

TERMODINAMIČKO MODELOVANJE RASTVORLJIVOSTI GASOVA U JONSKIM TEČNOSTIMA KORISTEĆI JEDNAČINE STANJA

Ovaj rad je usmeren na termodinamičko modelovanje rastvorljivosti gasova u jonskim tečnostima koristeći sledeće jednačine stanja: Soave-Redlich-Kwong (SRK), Cubic-Plus-Association (CPA) i Perturbed-Chain Statistical Associating Fluid Theory (PC-SAFT). Zbog toga su razvijene rutinske metode parametrizacije jonskih tečnosti. Zatim su jonske tečnosti implementirane u simulatoru Aspen plus da bi procenili jednačine stanja i istražili podatke za ravnotežu faza prediktivnim jednačinama i korelacijom parametra binarne interakcije. Tako je verifikovana korelacija gustine, dok su krive brzine zvuka imale ograničenja za ispravljanje nagiba krivih za čiste jonske tečnosti. Bez obzira na to, jednačina stanja PC-SAFT sa asocijativnom šemom 4C pokazala ee prikladnijom za termofizička svojstva. Što se tiče predviđanja ravnoteže faze za [EMIM] [TFO], jednačina stanja PC-SAFT sa 2B šemom pokazala se boljom za CO₂, dok je jednačina stanja CPA sa 2B šemom imala najbolji rezultat za H₂S. Za [OMIM] [NTF₂], jednačina stanja PC-SAFT sa 1A šemom pokazala je bolje rezultate za CO₂, a jednačina stanja CPA sa 2B šemom pokazala je najmanje odstupanje za H₂S.

Ključne reči: termodinamičko modelovanje, jonske tečnosti, jednačine stanja, povezivanje, Aspen plus.

PERIASAMY MANIKANDAN
SRINIVASAN
NESAKUMAR DHARMAKKAN
MAHA DEVA SRI VISHNU
HARI PRASATH
RAMARAJ GOKUL
GANESHAN THIYAGARAJAN
GOVINDASAMY
SIVASUBRAMANI
BALACHANDRAN
MOULIDHARAN

Department of Chemical
Engineering, Kongu Engineering
College, Erode, India

SCIENTIFIC PAPER

UDC 621.4:621.892:536.2

HEAT TRANSFER STUDIES IN A PLATE HEAT EXCHANGER USING Fe_2O_3 -WATER- ENGINE OIL NANOFLUID

Article Highlights

- Fe_2O_3 /engine oil/ Water mixed nanofluid were prepared using a high-pressure homogenizer
- The heat transfer performance of Fe_2O_3 suspended base fluid was studied in a plate heat exchanger
- Convective heat transfer coefficient, Reynolds, Prandtl, and Nusselt numbers were determined and analyzed

Abstract

Improving the heat transfer performance of conventional fluid creates significant energy savings in process Industries. In this aspect, an experimental study was performed to evaluate the heat transfer performance of Fe_2O_3 -water (W)-engine oil (EO) nanofluid at different concentrations and hot fluid inlet temperatures in a plate heat exchanger. Experiments were conducted by mixing Fe_2O_3 nanoparticles (45 nm) in a W-EO mixture base fluid with volume fractions of 5% EO + 95% W and 10% EO + 90% W. The main aim of the present study was to assess the impacts of nanoparticle volume fraction and hot fluid inlet temperature variations on the heat transfer performance of the prepared nanofluid. The convective heat transfer coefficient, Reynolds, Prandtl, and Nusselt numbers were determined based on the experimental results. The result shows that at the hot fluid inlet temperature of 75 °C, the increase in Nusselt number and convective heat transfer coefficient are optimum at 0.9 vol. % nanoparticle for both the base fluid mixtures. The increase in heat transfer coefficient is because of the Brownian motion (increasing thermal conductivity) effect, motion caused by the temperature gradient (Thermo-phoretic), and motion due to concentration gradient (Osmophoretic). If the volume fraction of the nanoparticle increases, then the Reynolds number increment is higher than the Prandtl number decrement, which augments the Nusselt number and convective heat transfer coefficient.

Keywords: engine oil, Fe_2O_3 , heat transfer, nanofluid, plate heat exchanger, water.

The most important manufacturing operations in process industries are heating and cooling [1]. Glycols, engine oil, and water are mostly used as base fluids in heat transfer applications. To improve the heat transfer

performance of these fluids, their thermal conductivity and heat transfer properties have to be enhanced [2]. Many research works are undergoing in this area by adding metal/metal oxide nanoparticles [3,4]. Recent advancement in energy reduction using nanofluid is noticed from a significant volume of research publications from the technical community. This nanofluid is also a new engineering fluid because of its unique application and capability for cost-cutting in heat transfer processes. Furthermore, researchers worked on developing nanoparticle-suspended heat transfer fluid in heat transfer equipment [5]. The following

Correspondence: P.M. Srinivasan, Department of Chemical Engineering, Kongu Engineering College, Erode-638 060, India.
E-mail: sriperiasamy@gmail.com
Paper received: 30 April, 2022
Paper revised: 22 November, 2022
Paper accepted: 23 November, 2022

<https://doi.org/10.2298/CICEQ220430029S>

section provides significant research performed with metal/ metal oxide and hybrid nanomaterials with different base fluids applied in heat exchangers.

To improve the thermal conductivity of heat transfer fluids, Choi *et al.* [6] proposed that adding small-size metals and metal oxide nanoparticles in a base fluid is a promising technique. The detailed review of challenges and applications of nanofluid in various sectors such as solar water heating, cooling of electronics, heat exchanging devices, engines, and cooling in machining, domestic refrigerator-freezers, diesel generators, chillers, and nuclear reactors were reported by Saidur *et al.* [7]. An experimental study in a heat exchanger with the addition of CuO nanoparticles in the water reported a notable enhancement in the heat transfer coefficient because of nanoparticle addition [8]. Furthermore, heat transfer studies with aluminum oxide/water nanofluid in a plate heat exchanger showed better heat transfer enhancement at a constant Reynolds number [9].

Mare *et al.* [10] prepared γ - Al_2O_3 and CNTs nanoparticles in a base fluid water and studied them in a plate heat exchanger. The study reports that the effect concerning the viscosity and pressure drop is significant at low pressure. Hence, this effect has to be considered while preparing nanofluid for heat transfer studies. The experimental study by Kwon *et al.* [11] in a plate heat exchanger showed a 30% increase in heat transfer coefficient at an Al_2O_3 nanoparticle concentration of 6 vol.%. Wang and Xu [12] used the steady-state parallel plate technique to measure the thermal conductivity with the Al_2O_3 and CuO nanoparticle suspension system in engine oil, vacuum pump fluid, distilled water, and ethylene glycol. The study concluded that the thermal conductivity of the nanoparticle-fluid mixtures increases significantly with nanoparticle addition, and more studies on heat transfer in the fluid flow are needed to extract its maximum benefit. The experimental thermal conductivity and heat transfer studies were done in a natural convection heat transfer apparatus [13,14] with a base fluid (ethylene glycol-water mixture). They observed a significant enhancement in heat transfer coefficient and thermal conductivity. The heat transfer effect of Al_2O_3 nanoparticles with volume fractions of 0.25 vol.%, 0.5 vol.%, 0.75 vol.%, and 1 vol.% was analyzed [15], and an increase in Nusselt number with respect to the Reynolds number and volume fraction was observed. Sarafraz *et al.* [16] used nanofluid consisting of biologically produced silver/coconut oil and assessed the effect on viscosity, thermal conductivity, and heat transfer coefficient in an annular heat exchanger and reported that this nanofluid could be applied as a lubricant as well as a coolant in engines

due to the enhancement in thermal conductivity and viscosity of the base fluid. Many similar studies with the addition of nanoparticles in a base fluid were shown to enhance the overall heat transfer (e.g., the addition of copper [17], TiO_2 and ZnO [18], MgO-TiO_2 , $\text{ZrO}_2\text{-CeO}_2$ [19,20], graphene [21,22] in a base fluid Ethylene Glycol-Water mixture). With Fe_2O_3 /water -The ethylene glycol mixture nanofluid studies were conducted in shell and tube heat exchangers and reported [23] with significant increment in heat transfer coefficient and thermal conductivity with the particle volume fractions (0.02%–0.06%). The hybrid nanofluid containing Fe_2O_3 and MWCNT nanoparticles significantly enhance electrical and thermal conductivities [24]. Also, it proposes a correlation equation to determine the thermal conductivity of a hybrid nanofluid. To extract the application of nanofluid in the building sectors, Sarafraz *et al.* [25] used therminol 66 oil as a heat transfer fluid with iron oxide (III) nanoparticle to perform heat transfer behavior of the prepared nanofluid and found better enhancement in the thermal performance of the therminol 66 oil (by the nanoparticle addition and obtained 19% increase in heat transfer coefficient at 0.3 wt. % of nanosuspension. Studies in an oscillating heat pipe (OHP) with a magnetic field show an increased heat transfer coefficient with the heat flux of Fe_2O_3 /kerosene nanofluid [26].

Studies with water- Fe_3O_4 nanofluid revealed that the thermal conductivity ratio increases proportionally with temperature and nanoparticle volume fraction [27]. The study showed a thermal conductivity enhancement of 48% (60°C and 2.0 vol.%) compared to the distilled water. Thermal performance of magnetite (Fe_3O_4) nanofluid in ethylene glycol (EG) and water (W) mixture shows 33%, 42%, and 46% thermal conductivity enhancements for 60:40% EG/W, 40:60% EG/W, and 20:80% EG/W based nanofluid, respectively [28]. Fe_3O_4 nanoparticles in paraffin show a 20% enhancement in thermal conductivity with the nanoparticle addition of 0.1 vol.% [29]. Kerosene-based Fe_3O_4 magnetic nanofluid showed a 34% thermal conductivity enhancement with a 1 vol% of nanoparticles [30].

A study on a shell and tube heat exchanger by the Fe_2O_3 /EG and Fe_2O_3 /water nanofluids reports an increase in the base fluid's thermal conductivity with the hot fluid's temperature [31]. A compact air-cooled heat exchanger with water-based iron oxide nanofluid under laminar flow conditions reports a 13% and 11.5% increase in the overall heat transfer coefficient and rate of heat transfer, respectively, at the concentration of 0.65 vol. % [32]. Studies on thermal conductivity analysis for the nanofluid consisting of $\text{Fe}_2\text{O}_3/\text{Al}_2\text{O}_3$ nanoparticle suspension in engine oil reported that

even a small amount of nanoparticle addition improved the thermal properties of the nano-lubricant and concluded a 33% improvement of the heat transfer coefficient at a mass fraction of 4% [33]. Mixing engine oil with different nanoparticles, such as diamond, copper oxide, and titanium oxide (TiO_2), showed that the nanoparticle addition to oil significantly contributes to the reduction of abrasion and friction and improves oil properties [34].

From the beginning of the nanofluid applications in different sectors, many works explored these novel fluids' distinctive properties and capabilities. Iron oxide (Fe_2O_3) is a non-toxic and cost-effective nanomaterial with good thermophysical and heat transfer properties. Many researchers on this topic are focusing only on thermal conductivity studies. However, it will be possible to explore its heat transfer properties in real-time heat exchangers. Nanofluid offers many advantages. However, certain disadvantages are found in real applications, such as fouling, surface erosion, and instability. Engine oil offers a solution to reduce fouling. Literature also supports that miniature plate heat exchangers are efficient with better performance for nanofluids. Hence, a compact plate heat exchanger was used in our study. Also, to the best of the author's knowledge, the heat transfer performance of a nanofluid mixture of Fe_2O_3 -W-EO has not been investigated in a plate heat Exchanger in the literature. In this work, experiments were conducted in a plate-type compact heat exchanger by mixing homogenized Fe_2O_3 nanoparticles in a base fluid of two different mixed base fluids, a W-EO mixture of volume fractions (5%EO + 95%W) and (10%EO + 90%W).

MATERIALS AND METHODS

Preparation of Fe_2O_3 -water-engine oil nanofluid

In this study, the Fe_2O_3 nanoparticles were suspended in a W-EO mixture with a two steps (sol-gel) method with a Fe_2O_3 nanoparticle size of 45 nm. Two types of mixed base fluids with volume fractions (5%EO + 95%W) and (10%EO + 90%W) were prepared by the amount calculated by Eq. (1).

$$\varphi = \frac{(m/\rho)_{\text{Fe}_2\text{O}_3}}{(m/\rho)_{\text{Fe}_2\text{O}_3} + (m/\rho)_{\text{W-EO}}} \quad (1)$$

To assure the stability of the prepared nanofluid, a high-pressure homogenizer was applied, and the prepared nanofluid was used in the plate heat exchanger as cold fluid. The SEM image of the Fe_2O_3 nanoparticle and the preparation method are shown in Figures 1 and 2, respectively. The prepared nanofluid was homogeneously suspended throughout the base fluid because of the high-pressure homogenizer.

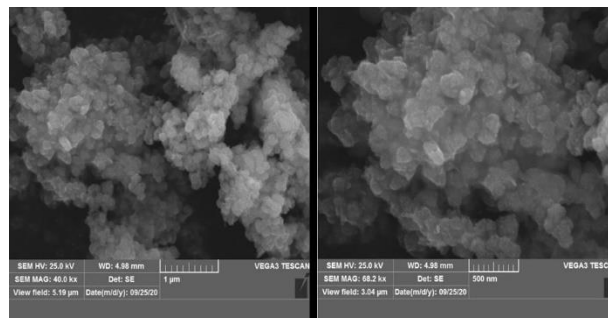


Figure 1. SEM image of Fe_2O_3 nanoparticle.



Figure 2. Preparation of the Fe_2O_3 -W-EO nanofluid.

Experimental set-up

Studies were conducted in a plate-type heat exchanger, where the hot and cold fluids flow in a counter-current pattern. Figure 3 presents the experimental set up with a plate heat exchanger and two containers (for cold and hot side fluid), a temperature controller, flow meters for flow measurement and control, and two fluid pumps. The plate heat exchanger consists of 13 stainless steel corrugated plates (Alfa Laval, India), providing seven and six flow channels for the hot and cold fluids, respectively. The plate length and thickness are 0.154 m and 0.25 mm, respectively.



Figure 3. Photographic view of the experimental set-up.

First, the cold fluid ($\text{Fe}_2\text{O}_3\text{-W-EO}$) was pumped to the heat exchanger through a rotameter and returned to the cold fluid reservoir. Next, the hot fluid (water) passed counter-currently through a control valve and entered the heat exchanger. The flow rate readings were measured and controlled by the flow meter. Finally, the hot and cold fluid's inlet and outlet temperature readings were altered with four K-type thermocouples inserted with the heat exchanger.

Determination of thermophysical properties of $\text{Fe}_2\text{O}_3\text{-W-EO}$ nanofluid

Thermal conductivity was measured using a thermal conductivity analyzer (Scientico, India), and viscosity was measured with a redwood viscometer for all the concentrations of the $\text{Fe}_2\text{O}_3\text{-W-EO}$ nanofluid, as shown in Figure 4.



Figure 4. Measurement of thermal conductivity and viscosity of the $\text{Fe}_2\text{O}_3\text{-W-EO}$ nanofluid.

The density and specific heat capacity of the nanofluid were calculated by Eqs. (2) and (3) [26,27]:

$$\rho_{nf} = (1 - \phi) \rho_f + \phi \rho_p \quad (2)$$

$$C_{p,nf} = ((1 - \phi) \rho_f C_{p,f} + \phi \rho_p C_{p,p}) / (\rho_{nf}) \quad (3)$$

The obtained results of the thermophysical

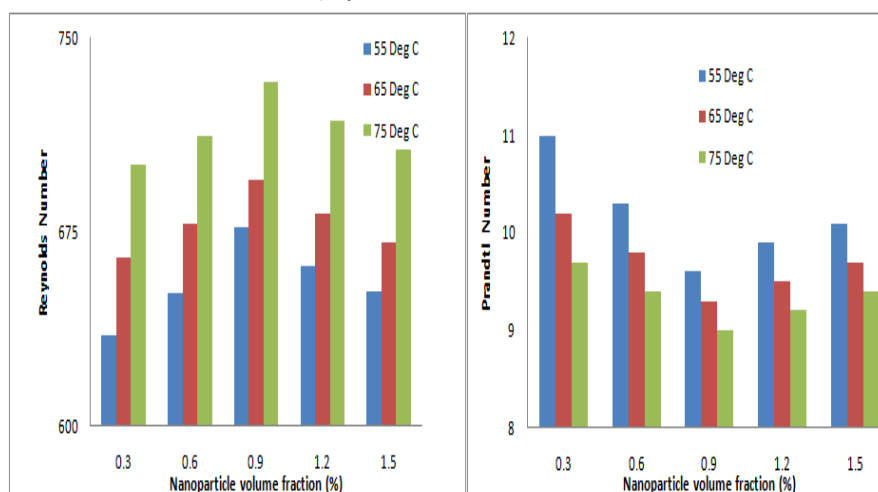


Figure 5. Effect of Fe_2O_3 nanoparticle volume fraction on the Reynolds and Prandtl numbers for a base fluid (5% EO + 95%W) at various hot fluid inlet temperatures.

properties were used for calculating different dimensionless numbers (Reynolds, Prandtl, and Nusselt numbers) applied in this study.

Determination of Nusselt number and heat transfer coefficient of $\text{Fe}_2\text{O}_3\text{-water-engine oil}$ nanofluid

Eqs. (4) and (5) were used to determine the Nusselt number [21] (Kim model) and the heat transfer coefficient of the nanofluid:

$$Nu = 0.295(NRe)^{0.64} (NPr)^{0.32} \left(\left(\frac{\Pi}{2} - \beta \right) \right) \quad (4)$$

$$h = \frac{Nu D_H}{K} \quad (5)$$

RESULTS AND DISCUSSION

To assess the heat transfer characteristics of Fe_2O_3 nanoparticle addition in the base W-EO fluid, the convective heat transfer coefficient (h) and dimensionless numbers, such as Reynolds, Prandtl, and Nusselt numbers, were calculated at different nanoparticle volume fractions (from 0.3% to 1.5%) and hot fluid temperatures (from 55 °C to 75 °C) for the EO-W base fluid volume fractions of (5:95 and 10:90).

Impact of Fe_2O_3 nanoparticle addition on Reynolds and Prandtl number for base fluid of (5% EO + 95%W) at various hot fluid inlet temperatures

The Reynolds number is the inertia and viscous force ratio, while the Prandtl number provides a relation between a flowing fluid's momentum and thermal transport. Figure 5 shows the effects of Fe_2O_3 nanoparticle volume fraction on the Reynolds and Prandtl numbers.

Figure 5 shows that the Reynolds number increases moderately with adding the nanoparticles. However, at a lower temperature, there is a significant increment in the Reynolds number because of the incremental effect in density concerning the viscosity of a nanofluid. Because of the Reynolds number increment and thermal capacity, the heat transfer rate increases significantly. Due to the incremental effect on the thermal conductivity of nanofluids, heat transport dominates over momentum transport. Hence, the Prandtl number decreases at all the volume fractions of nanofluid (Figure.5).

Impact of Fe₂O₃ nanoparticle addition on Nusselt number and heat transfer coefficient for a base fluid of (5 % EO + 95%W) at various hot fluid inlet temperatures

The Nusselt number and convective heat transfer coefficient were calculated to assess the heat transfer characteristics of the prepared nanofluid. Experimental results of Nusselt number and heat transfer coefficient was presented in Figure 6 by observing the impact on different hot fluid inlet temperature (55 °C, 65 °C, and

75 °C) and nanoparticle volume fraction (0.3–1.5%) of a base fluid volume fraction of 5:95.

Based on the experimental results at the hot fluid inlet temperature of 55° C, the Nusselt number and convective heat transfer coefficient increase with the nanoparticle volume fraction. However, the optimum enhancement was obtained at the nanoparticle volume fraction of 0.9%. After this concentration, the enhancement decreases due to the decrease in fluid thermal boundary layer thickness (viscosity decreases near the wall). Concerning the convective heat transfer coefficient, a similar pattern (heat transfer increases with nanoparticle volume fraction) was observed since, at the higher nanoparticle concentration, the thermal conductivity and Brownian motion play a significant role in enhancing the rate of heat transfer. It is also confirmed from Figure 6 that the Nusselt number enhancement is directly proportional to nanoparticle concentration and hot fluid temperature; however, the maximum enhancement was noted at 0.9 volume% of nanoparticle volume fraction.

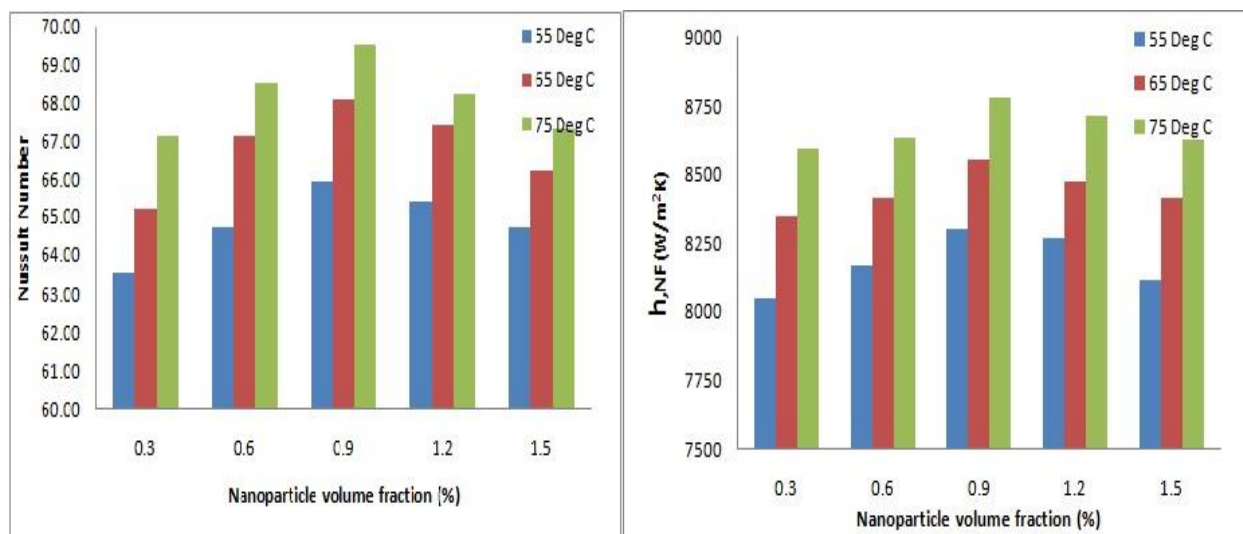


Figure 6. Effect of Fe₂O₃ nanoparticle volume fraction on the Nusselt number and the heat transfer coefficient for a base fluid (5 % EO + 95%W) at various hot fluid inlet temperatures.

Impact of Fe₂O₃ nanoparticle addition on Reynolds number and Prandtl number for a base fluid of (10 % EO + 90%W) at various hot fluid inlet temperatures

Figure 7 presents the effect of Fe₂O₃ nanoparticle addition on the Reynolds and Prandtl numbers for a base fluid of (10% EO + 90% W) for changes in the inlet temperature of the hot fluid.

Figure 7 shows a similar impact, i.e., the addition of nanoparticles increases the Reynolds number and observes the maximum Reynolds number of 647 for the nanoparticle concentration of 0.9 (volume%) and hot fluid temperatures. Figure 7 also depicts the variations in the Prandtl number under the same operating conditions. Again, it can be seen that the Prandtl

number decreases with an enhancement of the nanoparticle volume fractions, and the maximum decrease was observed at 0.9 (volume%) with a value of 10.2, 9.8, and 9.4. This effect on the Reynolds and Prandtl numbers can be related to the effect on the density and viscosity of the nanofluid compared with the base fluid (W-EO).

Impact of Fe₂O₃ nanoparticle addition on Nusselt number and heat transfer coefficient for a base fluid of (10 % EO + 90%W) at various hot fluid inlet temperatures

Figure 8 plots the changes in Nusselt number and heat transfer coefficient for the base fluid ratio of 5:95%

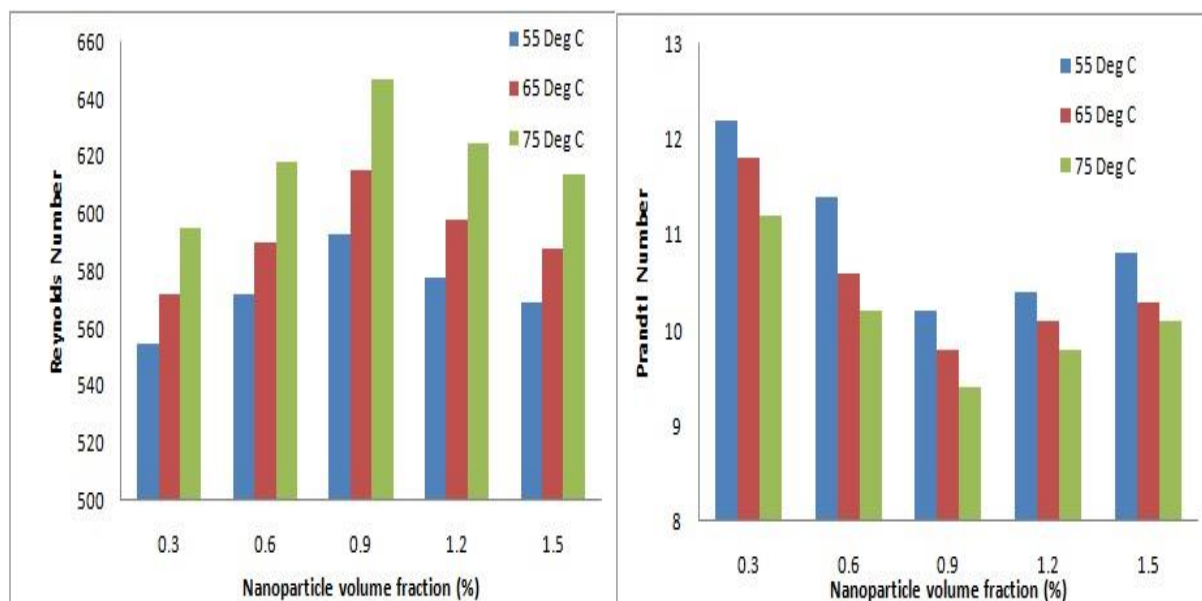


Figure 7. Effect of Fe_2O_3 nanoparticle volume fraction on the Reynolds and Prandtl numbers for a base fluid (10 % EO + 90%W) at various hot fluid inlet temperatures.

and 10:90% (EO: W) to show the impact of the nanoparticle addition of 0.3 vol.% to 1.5 vol.% at different hot fluid inlet temperatures. Increasing the nanoparticle volume fraction in all samples augments the Nusselt number and the heat transfer coefficient. These changes are linear at all the temperatures, however different ranges based on the temperature inlets. This Nusselt number improvement is due to the rate of increase of heat transfer by the Fe_2O_3 nanoparticle addition, which not only improves the thermal conductivity of the base fluid but also incurs a thermal dispersion in the flow, a novel way of improving

heat transfer processes. At a low nanoparticle volume fraction of (0.3%), as can be seen in Figure 7, the enhancement of the Nusselt number is low, and it increases slowly with increasing the nanoparticle volume fraction up to 0.9 vol.%; after that, the enhancement decreases, and the optimum enhancement is observed at the 0.9 vol.% Fe_2O_3 nanoparticle volume fraction. Figure 8 also shows that up to 0.9 vol.% of nanoparticles, the heat transfer coefficient increment was high; after that, it slowly decreases, and the heat transfer coefficient values are 7325 W/m²K at 55 °C and 7975 W/m²K at 75 °C.

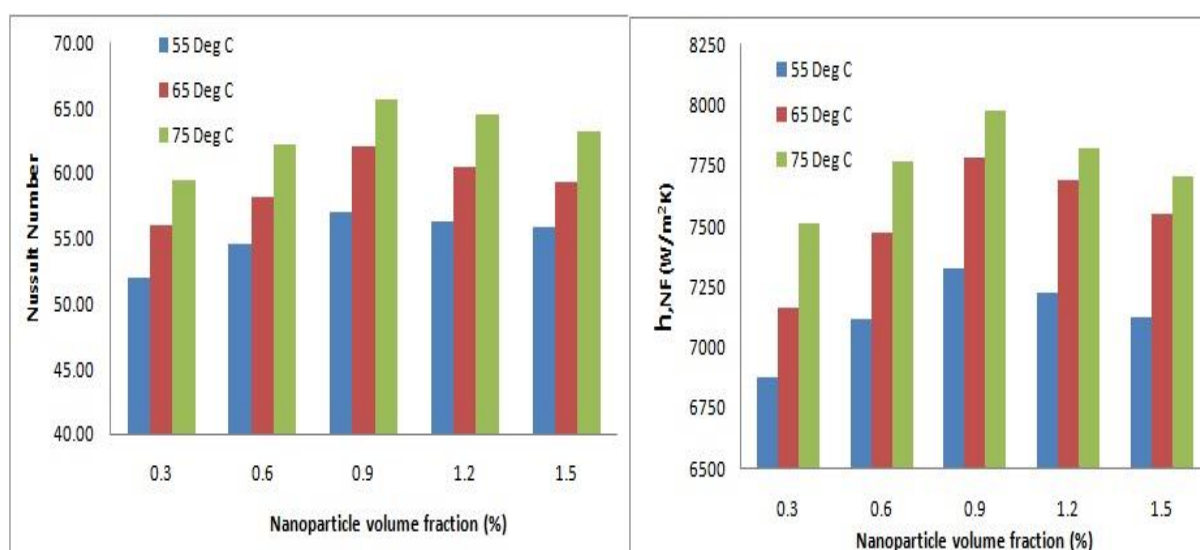


Figure 8. Effect of Fe_2O_3 nanoparticle volume fraction on the Nusselt number and the heat transfer coefficient for a base fluid (10 % EO + 90%W) at various hot fluid inlet temperatures.

CONCLUSION

A high-pressure homogenizer was used for the nanofluid preparation in the form of a uniform suspension throughout the study. The study shows that the heat transfer coefficient and Nusselt number of the W-EO mixture increase significantly by adding Fe₂O₃ nanoparticles. This addition not only improves the thermal conductivity of the base fluid but also incurs a thermal dispersion in the flow, which is a novel way of improving heat transfer processes. The results indicate that the Reynolds number increases moderately while the Prandtl number decreases proportionately at all the nanoparticle concentrations. However, the nanoparticle volume fraction significantly affects the Reynolds and Prandtl numbers at lower temperatures. For a given set of operating parameters, an optimum enhancement in heat transfer coefficient was observed at 0.9 vol.% of Fe₂O₃ nanoparticle for both base fluid fractions. The study reveals that heat transfer enhancement is high at all nanofluid concentrations at a higher hot fluid temperature (75 °C). Because of the heat transfer properties improvement, the Fe₂O₃-W-EO can be used as an alternate fluid in engines and other heat transfer applications.

It is suggested to study the heat transfer performance of the heat exchanger by considering the effect of experimental time on the results since the nanofluid properties are affected by the running time in the system (mainly stability). Furthermore, further heat transfer studies may be performed by combining different metal/metal oxide nanoparticle suspensions with different base fluids. In the future, studies with hybrid nanofluid (mixing different nanoparticles in the base fluid) can be explored and scaled up for industrial heat exchangers.

ACKNOWLEDGEMENT

The authors are grateful for the financial contribution of the Students Project Grand by TNSCST and SEED Grand provided by the management of the Kongu Engineering College and Department of Chemical Engineering for the facility.

NOMENCLATURE

W	Water
EO	Engine oil
D _H	Hydraulic diameter, m
ΔT _{LMTD}	Logarithmic mean temperature difference
ϕ	Nanoparticle volume fraction, dimensionless
m	Mass, kg
U	Overall heat transfer coefficient, W/m ² K
N _{Nu}	Nusselt number, dimensionless

N _{Pr}	Prandtl Number, dimensionless
N _{Re}	Reynolds number, dimensionless
V	Volumetric flow rate, liter/min
N	Number of channels, dimensionless
b	Plate depth, m
C _p	Specific heat capacity, J/(kg K)
L _w	Plate width, m
PHE	Plate heat exchanger
Pr	Prandtl number, dimensionless
h	Heat transfer coefficient, W/m ² K
vol. %	Volume %
Greek symbols	
β	corrugation angle, °
ρ	density, kg/m ³
μ	dynamic viscosity, Pa s
ϕ	nanoparticle volume fraction, dimensionless
k	thermal conductivity, W/(m K)
Subscripts	
T _{b,c}	cold fluid bulk temperature
T _h	temperature of hot fluid, °C
T _c	temperature of cold fluid, °C
H	hot fluid
C	cold fluid
in	inlet
out	outlet
nf	nanofluid
f	base fluid
p	Particle

REFERENCES

- [1] A. H. Elsheikh, H. N. Panchal, S. Sengottain, N. Alsaleh, M. Ahmadein, *Water*. 14 (2022) 1–13. <https://doi.org/10.3390/w14060852>.
- [2] B. Mehta, D. Subhedar, H. Panchal H, Z. Sai, *J. Mol. Liq.* 364 (2022) 120034. <https://doi.org/10.1016/j.molliq.2022.120034>.
- [3] M. Vaka, R. Walvekar, A.K. Rasheed, M. Khalid, H. Panchal, *IEEE Access*. 8 (2020) 58227–58247. <https://doi.org/10.1109/ACCESS.2019.2950384>.
- [4] R. Walvekar, Y. Y. Chen, R. Saputra, M. Khalid, H. Panchal, D. Chandran, N. M. Mubarak, K. K. Sadasivuni, *J. Taiwan Inst. Chem. Eng.* 128 (2021) 314–326. <https://doi.org/10.1016/j.jtice.2021.06.017>.
- [5] S. Chandrakant, H. Panchal, K. K. Sadasivuni, *Energy Sources, Part A*, 43 (2021) <https://doi.org/10.1080/15567036.2021.1900457>.
- [6] S.U.S. Choi, S. Lee, S. Li, J. A. Eastman, *J. Heat Transfer* 121 (1999) 280–289. <https://doi.org/10.1115/1.2825978>.
- [7] M. Sabiha, R. Saidur, S. Mekhilef, O. Mahian, *Renewable Sustainable Energy Rev.* 51 (2015) 1038–1054. <https://doi.org/10.1016/j.rser.2010.11.035>.
- [8] M.N. Pantzali, A.G. Kanaris, K.D. Antoniadis, A.A. Mouza, *Int. J. Heat Fluid Flow* 30 (2009) 691–699. <https://doi.org/10.1016/j.ijheatfluidflow.2009.02.005>.
- [9] D. Huang, Z. Wu, B. Sunden, *Int. J. Heat Mass Transfer* 89 (2015) 620–626. <https://doi.org/10.1016/j.ijheatmasstransfer.2015.05.082>.
- [10] T. Mare, S. Halelfadl, S. Duret, P. Estelle, *Exp. Therm. Fluid Sci.* 35 (2011) 1535–1543. <https://doi.org/10.1016/j.expthermflusci.2011.07.004>.
- [11] Y.H. Kwon, D. Kim, L. Chengguo, J.K. Lee, *J. Nanosci. Nanotechnol.* 11 (2011) 5769–5774. <https://doi.org/10.1166/jnn.2011.4399>.
- [12] X. Wang, X. Xu, *J. Thermophys. Heat Transfer* 13 (1999) 474–480. <https://doi.org/10.2514/2.6486>.

- [13] P.M. Srinivasan, N. Dharmakkan, M.D. Sri Vishnu, H. Prasath, R. Gokul, *Hem. Ind.* 75 (2021) 341–352. <https://doi.org/10.2298/HEMIND210520031S>.
- [14] S.P. Manikandan, N. Dharmakkan, S. Nagamani, *Chem. Ind. Chem. Eng. Q.* (2022) Article in Press <https://doi.org/10.2298/CICEQ210125021M>.
- [15] M. Unverdi, Y. Islamohlu, *Therm. Sci.* 21 (2017) 2379–2391. <https://doi.org/10.2298/TSCI151110097U>.
- [16] M.M. Sarafraz, *Chem. Biochem. Eng. Q.* 30 (2017) 489–500. <https://doi.org/10.15255/CABEQ.2015.2203>.
- [17] S.P. Manikandan, R. Baskar, *Chem. Ind. Chem. Eng. Q.* 27 (2021) 15–20. <https://doi.org/10.2298/CICEQ191220020P>.
- [18] S.P. Manikandan, R. Baskar, *Chem. Ind. Chem. Eng. Q.* 24 (2018) 309–318. <https://doi.org/10.2298/CICEQ170720003M>.
- [19] H. Panchal, R. Sathyamoorthy, A.E. Kabeel, A. El-Agouz, D. Rufus, T. Arunkumar, A. Muthu Manohar, D. Prince Winston, A. Sharma, N. Thakar, K. K. Sadasivuni, J. *Therm. Anal. Calorim.* 138 (2019) 3175–3182. <https://doi.org/10.1007/s10973-019-08346-x>.
- [20] R. Vidhya, T. Balakrishnan, B. Suresh Kumar, R. Palanisamy, H. Panchal, L. Angulo-Cabanillas, S. Shaik, B. Saleh, I. M. Alarifi, J. *Therm. Anal. Calorim.* (2022) 1–11. <https://doi.org/10.1155/2022/6596028>.
- [21] S.P. Manikandan, R. Baskar, *Chem. Ind. Chem. Eng. Q.* 27 (2021) 177–187. <https://doi.org/10.2298/CICEQ200504036P>.
- [22] S.P. Manikandan, R. Baskar, *Period. Polytech., Chem. Eng.* 62 (2018) 317–322. <https://doi.org/10.3311/PPch.11676>.
- [23] N. Kumar, S.S. Sonawane, S.H. Sonawane, *Int. Commun. Heat Mass Transfer* 90 (2018) 1–10. <https://doi.org/10.1016/j.icheatmasstransfer.2017.10.001>
- [24] A. Amir, S.A.A. Mirjalily, N. Nasirizadeh, H. Kargarsharifabad, *Int. Commun. Heat Mass Transfer* 117 (2020) 1–8. <https://doi.org/10.1016/j.icheatmasstransfer.2020.104603>.
- [25] M.M. Sarafraz, A.D. Baghi, M.R. Safaei, A.S. Leon, R. Ghomashchi, M. Goodarzi, C.X. Lin, *Energies* 12 (2019) 1–13. <https://doi.org/10.3390/en12224327>.
- [26] H.R. Goshayeshi, M. Goodarzi, M. Dahari, *Exp. Therm. Fluid Sci.* 68 (2015) 663–668. <https://doi.org/10.1016/j.expthermflusci.2015.07.014>.
- [27] L.S. Sundar, M.K. Singh, A. Sousa, *Int. Commun. Heat Mass Transfer* 44 (2013) 7–14. <https://doi.org/10.1016/j.icheatmasstransfer.2013.02.014>
- [28] L.S. Sundar, M.K. Singh, A. Sousa, *Int. Commun. Heat Mass Transfer* 49 (2013) 17–24. <https://doi.org/10.1016/j.icheatmasstransfer.2013.08.026>
- [29] R.S. Khedkar, A. Saikiram, S.S. Sonawane, K. Wasewar, S.S. Umre, *Procedia Eng.* 51 (2013) 342–346. <https://doi.org/10.1016/j.proeng.2013.01.047>.
- [30] W. Yu, H. Xie, L. Chen, Y. Li, *Colloids Surf., A* 355 (2010) 109–113. <https://doi.org/10.1016/j.colsurfa.2009.11.044>.
- [31] S.Z. Guo, Y. Li, J.S. Jiang, H.Q. Xie, *Nanoscale Res. Lett.* 5 (2010) 1222–1227. <https://doi.org/10.1007/s11671-010-9630-1>.
- [32] Y. Vermahmoudia, S.M. Peyghambarzadeh, S.H. Hashemabadi, M. Naraki, *J. Theor. Appl. Mech.* 44 (2014) 32–41. <https://doi.org/10.1016/j.euromechflu.2013.10.002>.
- [33] T.S. Mohsen, K. Arash, *J. Mol. Liq.* 283 (2019) 660–666. <https://doi.org/10.1016/j.molliq.2019.03.140>.
- [34] Y.Y. Wu, W.C. Tsui, T.C. Liu, *Wear* 262 (2007) 819–825. <https://doi.org/10.1016/j.wear.2006.08.021>.

PERIASAMY MANIKANDAN
SRINIVASAN
NESAKUMAR DHARMAKKAN
MAHA DEVA SRI VISHNU
HARI PRASATH
RAMARAJ GOKUL
GANESHAN THIYAGARAJAN
GOVINDASAMY
SIVASUBRAMANI
BALACHANDRAN
MOULIDHARAN

Department of Chemical
Engineering, Kongu Engineering
College, Erode, India

NAUČNI RAD

ISTRAŽIVANJA PRENOSA TOPLOTE U PLOČASTOM RAZMJENJUĆU TOPLOTE KORISTEĆI NANOFLUID Fe_2O_3 -VODA- MOTORNO ULJE

Poboljšanje performansi prenosa toplote konvencionalnog fluida stvara značajne uštede energije u procesnim industrijama. Sa ovog aspekta, sprovedena je eksperimentalna studija za procenu performansi prenosa toplote nanofluida Fe_2O_3 -voda-motorno ulje pri različitim koncentracijama i ulaznim temperaturama toplijeg fluida u pločasti razmenjivač toplote. Eksperimenti su sprovedeni mešanjem nanočestica Fe_2O_3 (45 nm) u baznom fluidu mešavine voda-motorno sa zapreminskim udelom od 5% motornog ulja + 95% vode i 10% motornog ulja +90% vode. Glavni cilj ove studije bio je da se procene uticaji zapreminskog udela nanočestica i varijacija temperature na ulazu toplijeg fluida na performanse prenosa toplote pripremljenog nanofluida. Na osnovu eksperimentalnih rezultata određeni su koeficijent konvektivnog prolaza toplote, Reynoldsov, Prandtl i Nusseltov broj. Rezultat pokazuje da su pri ulaznoj temperaturi toplijeg fluida od 75 °C, optimalno povećanje Nusseltovog broja i koeficijenta konvektivnog prenosa toplote pri 0,9 vol.% nanočestica za obe smeše baznih tečnosti. Povećanje koeficijenta prenosa toplote je zbog efekta Braunovog kretanja (povećanje toplotne provodljivosti), kretanja izazvanog temperaturnim gradijentom (termoforetski) i kretanja usled gradijenta koncentracije (osmoforetski). Ako se zapreminski udeo nanočestice poveća, onda je porast Reynoldsovog broja veći od promene Prandtl i Nusseltovog broja, što povećava Nusseltov broj i koeficijent konvektivnog prenosa toplote.

Ključne reči: motorno ulje, Fe_2O_3 , prenos toplote, nanofluid, pločasti razmenjivač toplote, voda.

SELMA KAYACAN-
CAKMAKOGLU¹
ILKER ATİK²
PERİHAN KUBRA AKMAN¹
IBRAHİM DOYMAZ³
OSMAN SAGDIC¹
SALİH KARASU¹

¹Department of Food
Engineering, Yıldız Technical
University, Esenler, Istanbul,
Turkey

²Food Technology, Afyon
Vocational School, Afyon
Kocatepe University,
Afyonkarahisar, Turkey

³Department of Chemical
Engineering, Yıldız Technical
University, Esenler, Istanbul,
Turkey

SCIENTIFIC PAPER

UDC 582.929.4:66.047:615.281

EFFECT OF THE DIFFERENT INFRARED LEVELS ON SOME PROPERTIES OF SAGE LEAVES

Article Highlights

- Five different infrared power were used to dry Sage leaves
- TPC and AA were protected better in dried at 88 W than the other IP powers
- Rosmarinic acid, caffeic acid, gallic acid, and luteolin were the major phenolics of Sage leaves
- All samples had antibacterial activity
- This study suggested 88 W for drying Sage leaves

Abstract

This study aims to investigate the effect of different infrared powers (IP) (38 W, 50 W, 62 W, 74 W, and 88 W) on drying kinetics, total phenolic content (TPC) and individual phenolics, antioxidant activity (AA) and antibacterial activity, and color quality of sage leaves. IP level significantly affected ($p < 0.05$) drying kinetics, bioactive contents, and color quality of sage leaves. Higher TPC and AA were obtained from the sample dried at 88 W. Rosmarinic acid, caffeic acid, gallic acid, and luteolin were found as major phenolic compounds, and their higher levels were obtained from the samples dried at an IP level of 88 W. All samples showed antibacterial activity on test pathogens. A higher correlation was observed between TPC, rosmarinic acid level, and antibacterial activity ($P > 0.80$). This study suggested that sage leaves should be dried at 88 W regarding lower drying times and color changes, lower phenolic degradation, and higher antibacterial activity.

Keywords: infrared drying, rosmarinic acid, phenolic profile, antibacterial activity, color.

Sage (*Salvia officinalis*) is a well-known aromatic herb from the mint family. It is an evergreen and fastest-growing plant. Its leaves have a strong aromatic smell. In the Latin name of sage, “*Salvia*” means to cure, and “*Officinalis*” means medicinal [1]. It is usually used for various purposes, such as antiheroic, carminative, expectorant, disinfectant, analgesic, and diuretic [2]. Sage also has been commonly used as filter tea [3].

In addition to medicinal properties, sage leaves

have strong antioxidant effects and are used for food preservation due to their antioxidant properties [4,5]. The antioxidant properties of sage have been investigated in many studies, and these studies, especially diterpenoids, triterpenoids, phenolic acids (exclusively caffeic acid derivatives), and flavonoids which form the majority of the phenolics in the *Salvia* species, have been emphasized [5–7]. The antioxidant property of *Salvia officinalis* originates from the abietane-type diterpenoids (carnosic acid and carnosol) and caffeic acid derivatives, particularly rosmarinic acid [8]. In addition to antioxidant activity, sage has antiproliferative [9], antimicrobial [10], and antitumor activities [11]. Besides, sage reduces or prevents lipid oxidation in some foods [12].

Like many other agricultural products, sage leaves have a high moisture content. In addition, it is a

Correspondence: S. Kayacan-Cakmakoglu, Department of Food Engineering, Yıldız Technical University, Esenler, 34210 Istanbul, Turkey.

E-mail: skayacan@yildiz.edu.tr

Paper received: 29 April, 2022

Paper revised: 1 November, 2022

Paper accepted: 28 November, 2022

<https://doi.org/10.2298/CICEQ220429030K>

seasonal and highly perishable plant herb. Therefore, postharvest technological processes, such as drying, should be applied to sage to provide all-year-round consumption and preservation [13]. Drying, as a preservation method, is a critical aspect of food processing. The purpose of drying is to reduce the product's water activity, thus preventing the growth of microorganisms, reducing chemical reactions, and extending the shelf life of food at room temperature [14]. Also, less space is required for storage, and dried product is lighter for easy transportation.

Because of its simple and easy application, hot air drying is the most used method for drying foodstuffs. However, hot air drying takes a long time due to low heat and mass transfer rates, and bioactive food components are damaged during the long drying process. Alternative drying methods with a higher drying rate and less damage to bioactive compounds should be applied to overcome these disadvantages [15]. High energy efficiency and short drying times are among the advantages of the infrared method. Water molecules absorb energy quickly. Therefore, quick water evaporation occurs, providing high food drying rates. Furthermore, using low-energy, better-quality dried foods can be obtained [16].

The effect of drying methods was investigated in many studies. The herbs' characteristics and the volatile components' concentrations depend on various factors, such as the drying method and the herb [2,13]. Some studies on hot-air drying have been reported in the literature [14,17,18] and microwave drying of the behavior of sage leaves [18]. These studies focused on drying kinetic different drying processes and their effect on some bioactive compound behavior of sage leaves. Hamrouni-Sellami *et al.* [14] conducted a comprehensive study focused on some drying methods for individual phenolics of sage leaves. Doymaz and Karasu [17] dried sage leaves using a cabinet dryer and found the highest TPC and AA at the lowest temperature (45 °C). Sadowska *et al.* [18] dried sage leaves under natural conditions, convective drying, and freeze-drying. They reported that drying conditions strongly affected drying duration and bioactive properties [19]. Jonas *et al.* [20] investigated the effect of oven-drying conditions on the key aroma content of sage leaves. However, there have been no studies on the effect of different infrared drying conditions on total bioactive content and individual phenolic components of sage leaves.

In the present study, the effects of different infrared levels on TPC, AA, phenolic profile, antibacterial activity, and color quality of sage leaves were investigated extensively. However, there is no comprehensive study of the effects of infrared drying on

the quality properties of sage leaves.

MATERIALS AND METHODS

Materials

Fresh sage (*Salvia officinalis* L.) leaves were collected in September 2021 from a house garden in Arsuz, Southern Turkey. The harvested leaves were stored in a refrigerator at 4 °C ± 1 °C, brought to the laboratory without breaking the cold chain, and stored in a refrigerator at 4 °C ± 1 °C until the drying experiments were started. The moisture content of fresh sage leaves was calculated as 70.58%, w. b. (2.399 kg water/kg dry matter, d. b.) in an oven at 105 °C for 24 h. Triplicate samples were used to calculate initial moisture content, and the average values were reported.

Experimental procedure

Drying experiments were carried out in a moisture analyzer with one 250 W halogen lamp (Snijders Moisture Balance, Snijders b.v., Tilburg, Holland). Sage leaves (33 g ± 0.5 g) were separated homogeneously over the drying chamber for the drying process. The drying process was conducted at the infrared power level varying from 38 W to 88 W. The IP level was adjusted in the control unit of equipment. Sample weight loss was recorded at 15 minute intervals during drying by a digital balance (model BB3000, Mettler-Toledo AG, Grefensee, Switzerland), which has a 0 g–3000 g measurement range with a reading accuracy of 0.1 g. Drying was ended when the moisture content of the sample reached 0.03 ± 0.01 kg water/kg dry matter (d.b.). The dried samples were cooled and packaged in low-density polyethylene bags and then heat-sealed (SMVK 126, Sonkaya Corporation, Istanbul, Turkey). The drying experiments were conducted in triplicate. Drying data were analyzed using a two-way analysis of variance at $p < 0.05$.

Extraction procedure

Fresh and dried sage samples were ground, and an aqueous methanol solution (20 vol.%) was added to grounded sage samples with the ratio 1:50. This mixture was shaken for 2 h in a shaking incubator (Mettmert WB-22) at room temperature [20]. After the extraction process, the solid/liquid mix was centrifuged (Hettich, Universal 320R, Tuttlingen, Germany) at 4,000 rpm for 10 min. Finally, samples were filtered by Whatman No. 1 and 0.45-µm microfilter. The extracts were kept at 4 °C for further analysis.

Total phenolic content (TPC)

The TPC of the sage samples was determined by the Folin-Ciocalteu method [21]. First, 2.5 mL of tenfold diluted Folin-Ciocalteu's phenol reagent was

added to tubes containing 0.5 mL of extract. Then, 2 mL of 7.5% Na₂CO₃ was added to the tubes. After 30 min incubation at room temperature in the dark, the absorbance at 760 nm was measured using a UV/VIS spectrophotometer (Shimadzu UV-1800, Kyoto, Japan). The calculations were made using Eq. (1) obtained from the created calibration curve for TPC:

$$A = 11.291C + 0.0442R^2 = 0.997 \quad (1)$$

where A and C indicate the absorbance and concentration values, respectively. TPC was expressed as mg gallic acid equivalent (GAE) per g dry samples.

Antioxidant activity (AA)

AA was determined using the DPPH method previously described by Si *et al.* [22]. 4.9 mL DPPH solution dissolved in 0.1 mM of methanol was added to the tubes containing 0.1 mL of extract. This mixture was incubated at room temperature for 40 min in a dark place. The absorbance of the mixture was read at 517 nm. The calculations were made using Eq. (2) obtained from the created calibration curve for DPPH:

$$A = 0.0018C + 0.017R^2 = 0.9961 \quad (2)$$

where A and C indicate the absorbance and concentration values, respectively. The results were expressed as $\mu\text{mol Trolox/g}$ samples.

Individual phenolic compounds

HPLC coupled to a diode array (HPLC-DAD, Shimadzu Corp., Kyoto, Japan) was used to analyze individual phenolic components in fresh and dried sage samples according to the method reported by Kayacan *et al.* [23]. The extracts for use in TPC analysis were filtered through a 0.45- μm membrane filter, and the samples were analyzed in an HPLC system (LC-20AD pump, SPD20A DAD detector, SIL-20A HT autosampler, CTO-10ASVP column oven, DGU-20A5R degasser, and CMB-20A communications bus module; (Shimadzu Corp., Kyoto, Japan).

Separations were performed at 40 °C on Intersil® ODS C-18 reversed-phase column (250 mm \times 4.6 mm length, 5 μm particle size). The mobile phases were solvent A (distilled water with 0.1% (v/v) acetic acid) and solvent B (acetonitrile with 0.1% (v/v) acetic acid). Gradient elution was 10% B (2 min), 10% to 30% B (2 min to 27 min), 30% to 90% B (27 min to 50 min), and 90% to 100% B (51 min to 60 min) and at 63 min returns to initial conditions. The flow rate was set to 1 mL/min. Chromatograms were recorded at 254 nm and 356 nm. Identification and quantitative analysis were carried out based on retention times and standard curves. The result of individual phenolics was expressed as mg/kg for fresh and dry sage samples.

Antimicrobial activity of sage extracts

The antimicrobial activity of sage extracts was determined using the disc diffusion method [24] against *Staphylococcus aureus* ATCC 29213, *Escherichia coli* ATCC 25922, *Salmonella* Typhimurium ATCC 14028, and *Listeria monocytogenes* ATCC 13932 pathogens. The pathogen cultures were cultivated overnight and spread onto Petri dishes containing nutrient agar. After waiting for bacterial penetration, sterile paper discs impregnated with sage extracts at 50 mg/mL concentration were placed on the agar. 20% methanol (v/v) was used as a negative control. Petri dishes were incubated at 37 °C for 24 h. Inhibition zones were measured and expressed as millimeters (mm).

Color

Fresh and dried sage leaves color values surface were measured by a chromameter (CR-13, Konica Minolta, Tokyo, Japan). The measurement was performed at four different edge spots on the surface of each sample [23]. The color values of the samples were expressed as L^* (whiteness/darkness), a^* (redness/greenness), and b^* (yellowness/blueness). The total color change (ΔE) was calculated using Eq. 3:

$$\Delta E = \sqrt{(\Delta L^*)^2 + (\Delta a^*)^2 + (\Delta b^*)^2} \quad (3)$$

Statistical analysis

Statistical evaluation was performed using the software program Statistica (StatSoft, Inc., Tulsa, OK). All analyzes were performed three times. First, the standard deviation and mean values were presented. Second, ANOVA was carried out to determine differences between samples. Third, Duncan, multiple comparison tests at a 95 % significance level was used to evaluate the effect of different infrared power on the TPC, AA, phenolic profile, antimicrobial activity, and color value of sage leaves. Finally, Pearson's coefficient of correlation was performed to determine the relation between TPC and antioxidant and antimicrobial activities.

RESULTS AND DISCUSSION

Analysis of infrared drying curves

Figure 1 shows the effect of IR power on the drying characteristics of the sage leaves during infrared drying. As seen in the figure, the drying curves are similar to the characteristic drying behavior of agricultural products [25]. As expected, the product's moisture content decreased exponentially with the drying time, and the moisture removal rate was higher at higher IR power.

As can be seen, an increase in the time required

for the samples to reach the targeted moisture content was 120 min, 80 min, 60 min, 50 min, and 40 min at the infrared power levels of 38 W, 50 W, 62 W, 74 W, and 88 W, respectively. In addition, the average drying rate of samples increased 3.0 times when the infrared power level increased from 38 W to 88 W. The faster drying rate and lesser drying time at higher IR power could be explained by the higher heat absorption resulting in higher product temperature and higher mass transfer driving force [26,27].

Change in TPC and AA

Table 1 shows the change in TPC and AA depending on the applied infrared power. The TPC values were significantly affected by applied infrared power. The TPC value of the fresh samples was found to be 24.5 mg GAE per g of dry samples. The TPC value of the dried samples ranged from 10.74 mg to 18.99 mg GAE per g dry samples. A significant loss of phenolic compounds was observed during the drying process ($P < 0.05$), and this loss was higher at low infrared power (56.16 %). The high reduction in TPC in sage leaves during the drying process was reported in previously published studies [19,28]. Sadowska *et al.* [28] reported that fresh sage leaves had the highest polyphenols (1,773.20 mg/100 fresh weight–chlorogenic acid equivalent). Also, the highest amount of polyphenolic compounds was significantly in freeze-dried sage samples compared to other dried sage (naturally dry, dried at 35 °C and 45 °C) and thyme samples. In contrast, the lowest amount of these compounds was recorded in sage leaves dried at 35 °C. This high reduction might be due to heat-sensitive phenolic

compounds such as carnosic acid and rosmarinic acid [28]. The change in phenolic compounds and b^* value showed a positive correlation (>90%), indicating that low infrared power cause higher degradation in TPC and pigments. The long drying process could explain the higher degradation during low power infrared drying. The higher retention of TPC at higher infrared power might be due to the disruption effect of the high temperature on the cell wall and releasing the phenolic compound from the insoluble part of the plant [29,30].

AA value was 19.76 $\mu\text{mol Trolox/g}$ for fresh samples and 12.32 $\mu\text{mol Trolox/g}$ –18.06 $\mu\text{mol Trolox/g}$. As shown, AA significantly decreased during the drying process. The change in AA showed a similar trend with TPC during drying. A higher AA value was observed from the sample dried at high infrared power. Bioactive substances' degradation could explain the AA reduction during the drying process.

An increase in TPC and AA with increasing infrared power was also reported in the study. Adak *et al.* [31] reported that increasing infrared power from 100 W to 300 W increased AA from 2.88 g/g DPPH to 5.81 g/g DPPH and TPC from 35171 mg/kg GAE to 44993 mg/kg GAE. This study suggests that sage leaves must be dried at 88 W to maintain TPC and AA.

Effect of IP on phenolic profile of sage leaves

Table 2 shows the individual phenolic distribution of the fresh and dried samples. Rosmarinic acid and luteolin were found as major phenolic compounds, and their levels were 1.92 mg/kg–13.60 mg/kg and 2.61 mg/kg–5.01 mg/kg, respectively. Gallic acid and

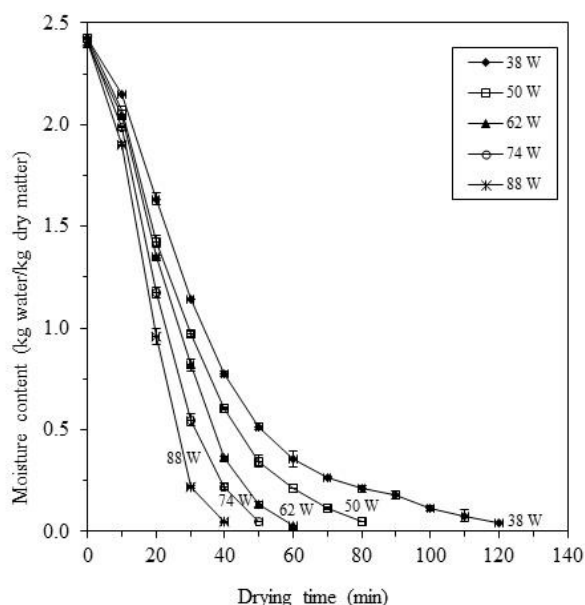


Figure 5. Variations of moisture content with drying time of sage leaves at different infrared powers.

Table 1. Effect of infrared power on the TPC and AA value of the sage leaves.

Infrared power (W)	TPC* (mg GAE /g dry samples)	AA* (μmol Trolox/g)
Fresh	24.50±0.52 ^a	19.76±0.01 ^a
38	10.74±0.19 ^f	12.32±0.20 ^c
50	17.34±0.10 ^c	12.92±0.76 ^c
62	14.35±0.05 ^e	13.18±0.84 ^c
74	15.20±0.57 ^d	16.34±2.85 ^{bc}

The different lowercase letters in the same column show statistical differences ($p < 0.05$). *TPC: Total phenolic content, AA: antioxidant activity.

caffeic acid were other abundant phenolic components with lower levels than rosmarinic acid and luteolin. The IP level significantly affected both the numbers of the phenolic compounds and their concentrations ($p < 0.05$). IP levels of 38 W and 50 W showed a high number of phenolic compounds. The degradation of heat sensitive phenolic compounds benzoic acid and vanillin could explain these results. However, benzoic acid was not detected for the samples dried by high IP (62 W, 74 W, and 88 W), and vanillin was not found for the IP level of 88 W.

Rosmarinic acid and luteolin levels were higher for the IP levels of 50 W and 88 W. The higher level of rosmarinic acid and luteolin values for high IP values

can be explained by two reasons. First, infrared radiation dramatically increased the phenolic compound accumulation. The other reason is the short drying time due to the high drying rate [32,33]. Phenolic compounds were less damaged because samples dried at 88 W had the lowest drying time. Exposure to prolonged heating leads to irreversible changes in temperature-sensitive phenolic substances [33]. Caffeic acid showed similar trends with rosmarinic acid and luteolin. Gallic acid levels increased with increased IP levels. A high correlation was observed with rosmarinic acid, luteolin, and caffeic acid. This study concluded that high infrared power should be conducted to preserve the major phenolic compounds.

Table 2. Phenolic profiles of the sage leaves.

Phenolic compounds (mg/kg)	Infrared Power (W)					
	Fresh	38	50	62	74	88
Gallic acid	2.22 ^b	1.32 ^e	1.51 ^d	1.90 ^c	1.67 ^d	2.90 ^a
Protocatechic acid	1.10 ^a	0.45 ^c	0.31 ^c	0.55 ^b	0.33 ^c	0.30 ^c
Caffeic acid	3.94 ^a	1.75 ^d	3.10 ^b	2.27 ^c	3.03 ^b	3.74 ^a
Vanillin	0.74 ^a	0.33 ^c	0.51 ^b	0.33 ^c	0.53 ^b	nd
p-Coumaric acid	0.31 ^a	0.13 ^c	0.40 ^a	0.33 ^a	0.25 ^b	0.37 ^a
Ferulic acid	1.00 ^a	0.27 ^c	0.81 ^b	1.37 ^a	0.90 ^b	1.10 ^a
Benzoic acid	3.00 ^a	1.53 ^c	2.37 ^b	nd	nd	nd
o-Coumaric acid	1.20 ^a	0.57 ^c	0.75 ^b	0.77 ^b	0.80 ^b	0.50 ^c
Rosmarinic acid	13.60 ^a	1.90 ^e	5.87 ^c	2.10 ^d	5.44 ^c	10.10 ^b
Luteolin	5.01 ^a	3.31 ^c	4.00 ^b	3.01 ^c	2.62 ^d	3.95 ^b

The different lowercase letters in the same row show statistical differences ($p < 0.05$). *nd: not detected.

Antibacterial effect of dried sage

The antimicrobial activity of sage extracts is given in Table 3. In general, all extracts inhibited the test pathogens. The inhibition zone diameters of extracts ranged from 12.33 mm to 23.50 mm. Phenolic compounds were less damaged because the IP of 88 W ensured the lowest drying time. Also, sage extracts were more effective on Gram-positive bacteria than Gram-negative bacteria. Similar results were reported previously [34,35]. The IP level significantly affected ($p < 0.05$) the antibacterial activity of dried sage leaves. The highest antibacterial effect on the tested pathogens was found for the fresh sample, and the lowest was at the IP of 62 W. The antibacterial activity of the sage leaves is due to phenolic substances, such as rosmarinic acid, caffeic acid, gallic acid, and ferulic acid, which are major phenolic components of sage [36].

The Pearson correlation was applied to explain the relationship between TPC and antimicrobial activity. A high correlation was observed between TPC (> 0.80), rosmarinic acid level (> 0.85), and antibacterial activity. As reported, rosmarinic acid is responsible for the strong antimicrobial activity of sage [37]. Also, Klančnik *et al.* [38] found that plant extracts with carnosic and rosmarinic acid as major components were more effective on Gram-positive than Gram-negative bacteria.

Color evaluation

Color is one of the most determinative quality parameters affecting consumers' choices. The L^* , a^* , and b^* values of the fresh sage leaves were recorded to be 52.08, -8.21, and 12.55. The negative a^* and positive b^* value of the sage leaves is related to green and yellow pigments, respectively. Table 4 shows the

Table 3. Antimicrobial activity of sage extracts against common foodborne pathogens (inhibition zone, mm).

Infrared Power (W)	<i>S. aureus</i> ATCC 29213	<i>E. coli</i> ATCC 25922	<i>S. Typhimurium</i> ATCC 14028	<i>L. monocytogenes</i> ATCC 13932
Fresh	24.6±1.8 ^a	22.7±2.4 ^a	24.3±1.2 ^a	29.7±1.4 ^a
38	15.7±2.1 ^{bc}	13.8±1.3 ^d	16.2±1 ^c	17.8±1.0 ^d
50	18.8±1.3 ^b	17±1.3 ^b	18±1b ^c	21.7±1.5 ^{bc}
62	12.3±2.5 ^c	12.3±1.5 ^d	14.5±0.5 ^d	15±1.0 ^e
74	17.7±1.5 ^b	15±2.0 ^b	17.5±0.9 ^{bc}	19.3±0.6 ^{cd}
88	19.5±1.5 ^b	18±1.0 ^b	19.2±1.3 ^b	23.5±1.3 ^b

*The different lowercase letters in the same column show statistical differences ($p < 0.05$).

Table 4. Results of color values for sage leaves.

Infrared power (W)	L^*	a^*	b^*	ΔE
38	42.88±0.30 ^b	0.95±0.03 ^a	8.41±0.27 ^a	13.63±0.03 ^c
50	43.81±0.51 ^b	1.13±0.01 ^a	8.19±0.02 ^a	13.22±0.26 ^d
62	44.92±0.46 ^a	1.73±0.06 ^a	8.02±0.04 ^b	13.06±0.21 ^d
74	41.34±0.14 ^c	2.32±0.14 ^b	7.87±0.02 ^c	15.75±0.17 ^b
88	40.93±0.16 ^d	2.51±0.03 ^c	5.86±0.01 ^d	16.33±0.12 ^a

*The different lowercase letters in the same column show statistical differences ($p < 0.05$).

L^* , a^* , b^* , and ΔE values of sage leaves dried at different IPs. As is seen in the Table, infrared power significantly affected color values ($p < 0.05$). The L^* decreased with increased infrared power; the lowest L^* value was obtained from the sample dried at 88 W. The lower L^* and higher a^* values could be explained by an increase in the formation of brown pigment with increasing power levels due to a non-enzymatic browning reaction [39]. a^* and b^* values of the dried sage leaves significantly differed ($p < 0.05$). The highest change in the a^* and b^* values was obtained from the sample dried at the highest infrared power. The reduction of the b^* value might be due to the degradation of the color pigments such as carotenoids and chlorophyll [39,40]. Therefore, the high infrared power could result in the degradation of the pigments. For this reason, ΔE was calculated to describe the total color change in *S. officinalis* leaves. ΔE value shows total color differences and gives information about the perceptible color change. ΔE value of all samples was higher than 3, indicating that perceptible change was observed after drying [41]. The highest result was obtained from the sample dried at 88 W, indicating that the formation of brown pigment could be considered the main factor determining color change during infrared drying. Similar results have already been reported [31,42].

CONCLUSION

In this study, the infrared drying technique was applied to drying sage leaves as an alternative drying method. The effects of various IP values on the sage leaves' drying time and bioactivity properties were studied. As the IP value increased, the drying time decreased significantly. The effect of the IP value on total phenolic compounds, phenolic profile, antioxidant,

antimicrobial properties, and color quality was found to be significant ($p < 0.05$). Therefore, the IP of 88 W was recommended as the most suitable IP value in this study due to the resulting low drying time and color change, high phenolic content, and antioxidant and antimicrobial properties. Further analysis, such as SEM images and volatile profile, should be conducted to understand the effect of IP on the quality of sage leaves in more detail.

REFERENCES

- [1] N.E. Durling, O.J. Catchpole, J.B. Grey, R.F. Webby, K.A. Mitchell, L. Yeap Foo, N.B. Perry, Food Chem. 101 (2007) 1417–1424. <https://doi.org/10.1016/j.foodchem.2006.03.050>.
- [2] A.A. Hassanain, Res. Agric. Eng. 57 (2011) 19–29. <https://doi.org/10.17221/14/2010-RAE>.
- [3] B. Pavlic, N. Teslic, A. Vidaković, S. Vidović, A. Velićanski, A. Versari, R. Radosavljević, Z. Zeković, Ind. Crops Prod. 107 (2017) 81–89. <https://doi.org/10.1016/j.indcrop.2017.05.031>.
- [4] G. Topcu, J. Nat. Prod. 69 (2006) 482–487. <https://doi.org/10.1021/np0600402>.
- [5] M. Bianchin, D. Pereira, J.F. Almeida, C. Moura, R.S. Pinheiro, L.F.S. Heldt, C.W.I. Haminiuk, S.T. Carpes, Molecules 25 (2020) 1–10. <https://doi.org/10.3390/molecules25215160>.
- [6] K. Sehnal, B. Hosnedlova, M. Docekalova, M. Stankova, D. Uhlirova, Z. Tothova, M. Kepin-ska, H. Milnerowicz, C. Fernandez, B. Ruttkay-Nedecky, H.V. Nguyen, A. Ofomaja, J. Sochor, R. Kizek, Nanomaterials 9 (2019) 1–26. <https://doi.org/10.3390/nano9111550>.
- [7] S. Francik, R. Francik, U. Sadowska, B. Bystrowska, A. Zawislak, A. Knapczyk, A. Nzeyimana, Materials 13 (2020) 1–15. <https://doi.org/10.3390/ma13245811>.
- [8] M. Ben Farhat, R. Chaouch-Hamada, J.A. Sotomayor, A. Landoulsi, M.J. Jordán, Ind. Crops Prod. 54 (2014) 78–85. <http://dx.doi.org/10.1016/j.indcrop.2014.01.001>.
- [9] Y.Y. Jiang, L. Zhang, H.P. Vasantha Rupasinghe, Biomed. Pharmacother. 85 (2017) 57–67. <https://doi.org/10.1016/j.biopha.2016.11.113>.

- [10] A. Salević, C. Prieto, L. Cabedo, V. Nedović, J.M. Lagaron, *Nanomaterials* 9 (2019) 1–17. <https://doi.org/10.3390/nano9020270>.
- [11] M. Keshavarz, A. Bidmeshkipour, A. Mostafaie, K. Mansouri, H. Mohammadi-Motlagh, *Cell J.* 12 (2011) 477–482. <https://www.sid.ir/FileServer/JE/82320110407.pdf>.
- [12] D. Altindal, N. Altindal, in *Essential Oils in Food Preservation, Flavor and Safety*, V.R Preedy Ed., Academic Press, San Diego, (2016) 715–721. <https://doi.org/10.1016/B978-0-12-416641-7.00081-X>.
- [13] M.A.M. Kandil, R.M. Sabry, S.S. Ahmed, *RJPBCS.* 7(4) (2016) 1112–1123. ISSN: 0975-8585.
- [14] I. Hamrouni-Sellami, F.Z. Rahali, I.B. Rebey, S. Bourgou, F. Limam, I. Marzouk, *Food Bioprocess. Technol.* 6 (2013) 806–817. <https://doi.org/10.1007/s11947-012-0877-7>.
- [15] A. Wojdyło, A. Figiel, P. Legua, K. Lech, Á.A. Carbonell-Barrachina, F. Hernández, *Food Chem.* 207 (2016) 170–179. <https://doi.org/10.1016/j.foodchem.2016.03.099>.
- [16] I. Doymaz, A.S. Kipcak, S. Piskin, *Czech J. Food Sci.* 33 (2015) 83–90. <https://doi.org/10.17221/423/2014-CJFS>.
- [17] İ. Doymaz, S. Karasu, *Qual. Assur. Saf. Crops Foods* 10 (2018) 269–276. <https://doi.org/10.3920/QAS2017.1257>.
- [18] U. Sadowska, A. Kopec, L. Kourimska, L. Zarubova, P. Kloucek, *J. Food Process. Preserv.* 41 (2017) 1–11. <https://doi.org/10.1111/jfpp.13286>.
- [19] M. Jebri, H. Desmorieux, A. Maaloul, E. Saadaoui, M. Romdhane, *Heat Mass Transfer* 55 (2019) 1143–1153. <https://doi.org/10.1007/s00231-018-2498-9>.
- [20] K.Ç. Selvi, A. Kabutey, G.A.K. Gürdil, D. Herak, S. Kurhan, P. Kloucek, *Plants* 9 (2020) 1–13. <https://doi.org/10.3390/plants9020236>.
- [21] V.L. Singleton, J.A. Rossi, *Am. J. Enol. Vitic.* 16 (1965) 144–158. <http://www.ajevonline.org/content/16/3/144.full.pdf+html>.
- [22] X. Si, Q. Chen, J. Bi, J. Yi, L. Zhou, X. Wu, *J. Food Process Eng.* 16 (2016) 157–164. <https://doi.org/10.1111/jfpe.12230>.
- [23] S. Kayacan, S. Karasu, P.K. Akman, H. Goktas, I. Doymaz, O. Sagdic, *LWT-Food Sci. Technol.* 118 (2020) 108830. <https://doi.org/10.1016/j.lwt.2019.108830>.
- [24] E.F. De Andrade, D. Carpiné, J.L.A. Dagostin, A. Barison, A.L. Rüdiger, G.I.B. de Muñiz, M.L. Masson, *Eur. Food Res. Technol.* 243 (2017) 2155–2161. <https://doi.org/10.1007/s00217-017-2918-y>.
- [25] J. Waewsak, S. Chindaruksa, C. Punlek, *Sci. Technol.* 11 (2006) 14–20. <https://ph02.tci-thaijo.org/index.php/SciTechAsia/article/view/41556/34343>.
- [26] A. Sarimeseli, M. Yuceer, *Chem. Process Eng.* 36 (2015) 425–436. DOI:10.1515/cpe-2015-0030
- [27] E. Aidani, M. Hadadkhodaparast, M. Kashaninejad, *Food Sci. Nutr.* 5 (2016) 596–601. <https://doi.org/10.1002/fsn3.435>.
- [28] J. López, K.S. Ah-Hen, A. Vega- Gálvez, A. Morales, P. García -Segovia, E. Uribe, (2017). *J. Food Process Eng.* 40 (2017) 1–11. <https://doi.org/10.1111/jfpe.12511>.
- [29] V.V. Milevskaya, Z.A. Temerdashev, T.S. Butyl'skaya, N.V. Kiseleva, *J. Anal. Chem.* 72 (2017) 342–348. <https://doi.org/10.1134/S1061934817030091>.
- [30] V. Dewanto, X. Wu, K.K. Adom, R.H. Liu, *J. Agric. Food Chem.* 50 (2002) 3010–3014. <https://doi.org/10.1021/jf0115589>.
- [31] Y. Choi, S.M. Lee, J. Chun, H.B. Lee, J. Lee, *Food Chem.* 99 (2006) 381–387. <https://doi.org/10.1016/j.foodchem.2005.08.004>.
- [32] N. Adak, N. Heybeli, C. Ertekin, *C. Food Chem.* 219 (2017) 109–116. <https://doi.org/10.1016/j.foodchem.2016.09.103>.
- [33] H. Xu, M. Wu, Y. Wang, W. Wei, D. Sun, D. Li, Z. Zheng, F. Gao, *Foods.* 11 (2022) 1–27. <https://doi.org/10.3390/foods11152240>.
- [34] X. Wu, M. Zhang, Z. Li, *LWT-Food Sci. Technol.* 111 (2019) 790–798. <https://doi.org/10.1016/j.lwt.2019.05.108>.
- [35] M. Marino, C. Bersani, G. Comi, *Int. J. Food Microbiol.* 67 (2001) 187–195. [https://doi.org/10.1016/S0168-1605\(01\)00447-0](https://doi.org/10.1016/S0168-1605(01)00447-0).
- [36] E.A. Palombo, S.J. Semple, *J. Ethnopharmacol.* 77 (2001) 151–157. [https://doi.org/10.1016/S0378-8741\(01\)00290-2](https://doi.org/10.1016/S0378-8741(01)00290-2).
- [37] I. Generalić Mekinić, I. Ljubenkov, S.S. Možina, H. Abramović, V. Šimat, A. Katalinić, T. Novak, D. Skroza, *Ind. Crop. Prod.* 141 (2019) 111741. <https://doi.org/10.1016/j.indcrop.2019.111741>.
- [38] A. Matkowski, *Biotechnol. Adv.* 26 (2008) 548–560. <https://doi.org/10.1016/j.biotechadv.2008.07.001>.
- [39] A. Klančnik, S. Piskernik, B. Jersek, S.S. Mozina, J. Microbiol. Methods. 81 (2010) 121–126. <https://doi.org/10.1016/j.mimet.2010.02.004>.
- [40] A. Mohammadi, S. Rafiee, Z. Emam-djomeh, A. Keyhani, *World J. Agric. Sci.* 4 (2008) 376–383. [http://www.idosi.org/wjas/wjas4\(3\)/15.pdf](http://www.idosi.org/wjas/wjas4(3)/15.pdf).
- [41] V. Lavelli, B. Zanoni, A. Zaniboni, *Food Chem.* 104 (2007) 1705–1711. <https://doi.org/10.1016/j.foodchem.2007.03.033>.
- [42] Z.S. Cserhalmi, Á. Sass-Kiss, M. Tóth-Markus, N. Lechner, *Innovative Food Sci. Emerging Technol.* 7(2006) 49–54. <https://doi.org/10.1016/j.ifset.2005.07.001>.
- [43] S.H. Ghaboos, S.M. Ardabili, M. Kashaninejad, G. Asadi, M. Aalami, *J. Food Sci. Technol.* 53 (2016) 2380–2388. <https://doi.org/10.1007/s13197-016-2212-1>.

SELMA KAYACAN-
CAKMAKOGLU¹
ILKER ATIK²
PERİHAN KUBRA AKMAN¹
IBRAHİM DOYMAZ³
OSMAN SAGDIC¹
SALİH KARASU¹

¹Department of Food
Engineering, Yıldız Technical
University, Esenler, Istanbul,
Turkey

²Food Technology, Afyon
Vocational School, Afyon
Kocatepe University,
Afyonkarahisar, Turkey

³Department of Chemical
Engineering, Yıldız Technical
University, Esenler, Istanbul,
Turkey

NAUČNI RAD

UTICAJ RAZLIČITOG INTENZITETA INFRACRVENOG ZRAČENJA NIVOA NA NEKA SVOJSTVA LISTA ŽALFIJE

Ova studija ima za cilj da istraži uticaj različite snage infracrvenog zračenja (38-88 W) na kinetiku sušenja, ukupni sadržaj fenola i pojedinačnih fenola, antioksidativnu aktivnost i antibakterijsku aktivnost, i kvalitet boje listova žalfije. Nivo snage infracrvenog zračenja je značajno uticao ($p < 0,05$) na kinetiku sušenja, bioaktivni sadržaj i kvalitet boje listova žalfije. Viši ukupni sadržaj fenola i antioksidativne aktivnost su dobijeni iz uzorka osušenog na 88 W. Glavna fenolna jedinjenja su rozmarinska, kafeinska i galna kiselina i luteolin, a njihovi viši nivoi su dobijeni iz uzoraka osušenih pri snazi infracrvenog zračenja od 88 W. Svi uzorci su pokazali antibakterijsku aktivnost na patogene mikroorganizme. Uočena je veća korelacija između ukupnog sadržaja fenola, koncentracije rozmarinske kiseline i antibakterijske aktivnosti ($p > 0,80$). Ova studija je sugerisala da listove žalfije treba sušiti rpi snazi od 88 W radi kraćeg vremena sušenja i manje promene boje, manje degradacije fenola i veće antibakterijske aktivnosti.

Ključne reči: infracrveno sušenje, rozmarinska kiselina, fenolni profil, antibakterijska aktivnost, boja.

ALANNA SILVEIRA DE MORAES¹
 GABRIELA OLIVEIRA CASTRO PONCINELLI¹
 ARON SEIXAS TERRA RODRIGUES¹
 LAISE FAZOL DO COUTO¹
 SILVIA LUCIANA FÁVARO²
 RITA DE CÁSSIA COLMAN¹

¹Universidade Federal Fluminense, Chemical Engineering and Petroleum Department, RJ, Brazil

²Universidade Estadual de Maringá - Mechanical Engineering Department, Maringá, PR, Brazil

SCIENTIFIC PAPER

UDC 544.47:66:547

STUDY OF CATALYTIC OXIDATION OF TOLUENE USING Cu-Mn, Co-Mn, AND Ni-Mn MIXED OXIDES CATALYSTS

Article Highlights

- Nanocrystalline AMn_2O_4 ($A = Co, Ni, Cu$) spinel-type mixed oxides were tested for VOC removal
- Spinel oxides are important due to their high thermal resistance, selectivity, and electronic properties
- The higher activity of NiMn oxide than CoMn and CuMn is due to a higher Mn^{3+} content
- The activity is also attributed to the synergistic effect of manganese on spinel and Ni^{2+} cations

Abstract

The successful synthesis of AMn_2O_4 ($A = Co, Cu, and Ni$) spinels via solution combustion was achieved in less time than other methods. All catalysts with the same fuel/nitrate ratio were used to oxidize toluene, and the relationship between their properties and activities was investigated. Among all, nickel manganite exhibited the most promising activity, and by changing the fuel/nitrate ratio, it was sought to obtain the most appropriate structure for the reaction studied. Physico-chemical analysis was used to define the characteristics of the synthesized catalysts. The results showed the successful synthesis of spinels and indicated that other materials peaks (single oxide phases) exist in the catalyst structure. BET-BJH analyses reveal the mesoporous structures and, given the limitations of the equipment, were all classified as less than $10 \text{ m}^2/\text{g}$. The SEM images evidence the influence of the urea content used. The particle size increases at higher fuel/nitrate ratios. Samples of NiMn1.67 and NiMn2.08 showed larger and denser, sparsely dispersed clusters. Simultaneously considering reactor analysis and test results, it was found that the synthesized catalyst with a fuel/nitrate ratio of 0.5 has the best performance on toluene oxidation.

Keywords: solution combustion synthesis, fuel-to-nitrates ratio, manganite spinels, toluene oxidation.

Due to concerns of medical and scientific communities about the increase of volatile organic compounds (VOCs) in the atmosphere and the cost of reducing anthropogenic emissions, the development of appropriate forms of disposal or transformation has

received a lot of attention. [1,2].

The U.S. Environmental Protection Agency (EPA) describes VOCs as a relevant group of many carbon compounds, excluding monoxide carbon, carbon dioxide carbon, acid carbon, metallic carbide or carbonate, and ammonium carbonate, which presents high atmospheric photochemical activities. VOCs are harmful to human health and the environment because of their toxicity, and they are a precursor of smog photochemical and ozone formation in the atmosphere [3,4]. Thus, the need to control and treat air pollution has become urgent. It is clearly evident in the numerous global, national, and regional environmental pollution control regulations developed to maintain healthy air

243

Correspondence: R. De Cássia Colman, Universidade Federal Fluminense, Chemical Engineering and Petroleum Department, Passo da Pátria Street, 156/bl E/102-A, CEP: 24210-240, Niterói, RJ, Brazil.

E-mail: ritacolman@id.uff.br

Paper received: 19 April, 2022

Paper revised: 22 August, 2022

Paper accepted: 14 December, 2022

<https://doi.org/10.2298/CICEQ220419031M>

quality. These strict standards have led the industrial and commercial sectors to rely on carbon adsorption, incineration, or purification technologies to reduce the environmental damage caused by technological advances [5,6].

Different techniques for controlling VOC emissions are divided into process and equipment modification and treatment techniques. The first one, also known as indirect measures, is characterized by the changes in the process, the raw material change, and equipment maintenance. The second group of direct measurements is characterized by destruction techniques (oxidation and biofiltration, for example) and recovery (such as membrane separation, absorption, adsorption, and condensation) [7,8].

In this context, catalytic oxidation is an interesting technology because it eliminates or transforms VOCs at relatively low temperatures (200 °C–450 °C), minimizes the formation of by-products, such as NO_x, and can be effectively applied over a wide range of VOC concentrations (up to 10,000 ppm) and highly recommended when highly diluted (about 1,000 ppm) [9–11]. Moreover, from an economic point of view, catalytic oxidation is also an attractive alternative due to the low energy consumption and lower cost of by-product treatments that are not practically formed [12,13].

Mixed transition metal oxides exhibit greater activities and stabilities than simple oxides because these metals can have more than one valence state, a property determined by the electronic configuration of the metal d level [14,16]. Compared to supported noble metal catalysts, mixed oxides have lower costs and higher resistance to impurities. Among the oxides of the present invention, the spinel-like structure has also been highlighted due to its high thermal resistance, selectivity, and electronic properties, which improve oxide reducibility [17–19].

The synthesis by solution combustion (SCS), also known as self-combustion or self-propagating, has gained prominence since it combines the advantages of the sol-gel technique with a good stoichiometry control, making it possible to synthesize homogeneous oxides and high purity [20–21]. In addition, the method combines good textural properties and excellent dispersion and distribution of the active phase obtained in short synthetic times compared to other methods [22]. This method involves the autoignition of an aqueous solution containing oxidizing reagents, such as nitrates, sulfates, and metal carbonates, and reducing reagents (also called fuels), such as urea, citric acid, and glycine. The heat required to conduct the reaction is provided by the process and not from an external source. It is due to the exothermic and self-

catalytic reactions that occur when the reactants reach the ignition temperature. The formation of a large amount of gases is a characteristic of the reactions. For example, 1 mol of the synthesized catalyst generates 22 moles of gases. The powder obtained after cessation of combustion may be a single phase or a combination of various metal oxides [22,24].

The characteristics of the powders synthesized by the SCS are mainly governed by the temperature reached when combustion occurs effectively. In turn, it depends exclusively on the type and amount of fuel used, so the fuel/nitrate ratio is considered one of the important parameters. In a more detailed study, careful analysis can be made of its influence on synthesized materials' phase formation and crystallite size.

The present work aims to obtain by SCS the mixed oxides type AMn₂O₄ (A = Co, Cu, and Ni), to evaluate its catalytic activities on toluene oxidation, and to evaluate the effect of different fuel/nitrate ratios on the physicochemical characteristics and catalytic activity of the NiMn₂O₄ catalyst.

EXPERIMENTAL

Catalysts preparation

For the synthesis of catalysts using the solution combustion method, the following nitrates (Sigma Aldrich®, 99.999%): Mn(NO₃)₂·4H₂O, Co(NO₃)₂·6H₂O, Cu(NO₃)₂·6H₂O, and Ni(NO₃)₂·6H₂O, and urea (NH₂CONH₂; Quimibrás, 99.5%) were used without any purification. The steps of combustion synthesis of catalysts are shown in Supplementary Information.

The reagents (nitrates and urea) were dissolved in 20 mL of deionized water and placed in a porcelain beaker. The solution obtained was placed under constant heating and stirring, and as the temperature increased and the water evaporated, the solution became viscous. The color of the solution also changed with increasing temperature, becoming progressively darker until it became completely black (Supplementary Information).

Near the ignition point, the solution's temperature drops rapidly away from the set point. However, combustion occurred, and the gaseous products were released as yellow smoke, forming a fine black powder (catalyst). The material obtained was weighed and calcined at 700 °C for 6 h to ensure spinel phase formation and to eliminate any presence of carbonaceous residues.

The abbreviated names were chosen to name the synthesized catalysts: Mn₃O₄, CoMn0.5, CuMn0.5, NiMn0.5, NiMn1.25, NiMn1.67, and NiMn2.08. In this nomenclature system, AMn (A=Co, Cu, or Ni) stands for AMn₂O₄, and the number indicates the fuel-to-

nitrate fuel/nitrate ratios of 0.5, 1.25, 1.67, or 2.08.

Catalysts characterization

The textural properties of the catalysts were determined using N₂ isotherms measured at -196 °C by a Micromeritics® ASAP 2420 instrument. The specific surface area (S_{BET}) was determined by the Brunauer-Emmett-Teller (BET) [25], and the pore volume and pore size distribution were calculated by the Barret-Joyner-Halenda (BJH) method [26].

The composition of the phases present in the samples was determined by the XRD technique in a Rigaku® Miniflex diffractometer using CuK α radiation ($\lambda = 1.54056 \text{ \AA}$). Diffraction patterns were collected over the 2θ range of 15°–70° with a step size of 0.02°. From the obtained diffractograms, it was possible to determine the crystalline phases present by comparison with peaks of known and tabulated materials and the average size of the lens of the metallic species by the Scherrer equation.

Fourier-transform infrared (FTIR) spectra were recorded on a Perkin Elmer spectrometer (System 2000). The samples were pressed into self-supported wafers and placed into a glass cell sealed by KBr windows in 3% (w/w) proportions; 32 successive scans were performed for each spectrum obtained.

The morphology of the oxides was analyzed by scanning electron microscopy using a high vacuum mode DEI QUANTA 250 apparatus with a voltage of 30 kV.

The analysis of temperature-programmed reduction with H₂ (TPR) was conducted with a Micromeritics® AutoChem 2920 under atmospheric pressure. Catalyst samples (0.3 g) were subjected to reduction using 10 vol.% H₂ in N₂ at 30 cm³/min and a linear heating rate of 10 °C/min from room temperature to 1000 °C.

Evaluation of catalytic performance

The samples were evaluated for catalytic oxidation of toluene. The reactions were carried out at atmospheric pressure in a continuous fixed bed U-shaped tubular reactor. The total flow rate of the reactant mixture (20% O₂ in He + 1000 ppm toluene) was 150 ml/min. The catalyst (0.1 g) was mixed with silicon carbide (SiC, 0.4 g) to avoid the effect of hot spots and deposited on a quartz wool plug. A tied thermocouple continuously monitored the temperature. First, the catalysts were reduced in an H₂ stream at their respective reduction temperature for 1 h. Then, the catalysts were evaluated at 100 °C, 200 °C, 300 °C, and 400 °C, under a mixture of O₂, toluene, and He (20% O₂, 1000 ppm toluene, and He to complete the balance), with a total flow of 150 mL/min After

remaining at each test temperature for 24 hours, the catalysts were heated under a helium flow to the next test temperature. In this way, it was also possible to evaluate the stability of the catalyst.

The products and reagents were analyzed by gas chromatography (Agilent® 7890A) equipped with a thermal conductive detector (TCD) and a flame ionization detector (FID) using a Porapak N column.

The products and reagents were analyzed by an Agilent® 7890A gas chromatograph with a flame ionization detector (FID) and thermal conductivity detector (TCD). The conversion of toluene (X%) was calculated according to Eq. (1):

$$X\% = \frac{[Tol]_{in} - [Tol]_{out}}{[Tol]_{in}} \times 100 \quad (1)$$

where $[Tol]_{in}$ and $[Tol]_{out}$ denote the inlet and outlet concentrations of toluene, respectively.

RESULTS AND DISCUSSION

According to the results obtained for N₂ adsorption (Figure 1), the isotherms used for all samples are classified in category type IV (of the IUPAC classification) and reveal the adsorption characteristics in multilayer related to weak interactions in mesoporous-containing materials (pore diameter between 2 and 50 nm). Isotherms of this type have defined levels and indicate capillary condensation [27].

It is also observed that the desorption curve does not coincide with the adsorption curve, a phenomenon known as hysteresis, due to the saturation pressure of N₂ being different in the condensation and evaporation from inside the pores. In all isotherms, the present hysteresis is of type H1, characterized by two branches of almost parallel isotherms. This hysteresis loop was observed at high relative pressures ($P/P_0 \approx 0.7$ to 0.9) and is generally associated with materials of mesoporous structures and a representative of an adsorbent consisting of rigid agglomerates of spherical particles and relatively uniform pore distribution [28,29].

It is also observed that the practically parallel branches of the adsorption and desorption isotherms of the CuMn0.5 sample are more vertical when compared to the other isotherms, indicating that the mesoporous size distribution is narrower. The lower values of relative pressure in the capillary condensation (around 0.2) in the Mn0.5 catalyst isotherm compared to the other synthesized catalysts, with a fuel/nitrate ratio of 0.5 to about 0.4, indicate a decrease in mesoporous size [27].

Although all surface areas were classified as less than 10, due to the limitation of the equipment used, the

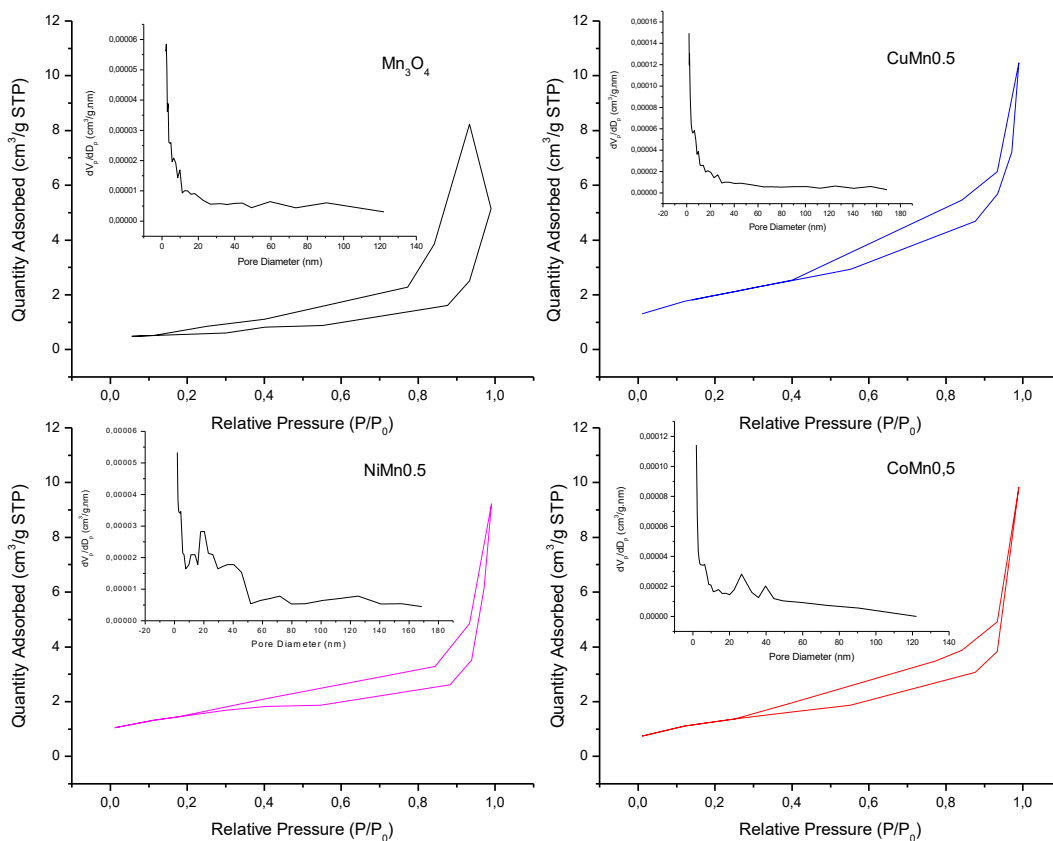


Figure 1. Adsorption/Desorption isotherms and BJH pore size distribution of the catalysts with a fuel/nitrate ratio of 0.5.

average pore diameter obtained by BJH was above 2 nm for all samples, the NiMn0.5 catalyst being with the largest distribution of mesoporous diameter (between 2 nm and 50 nm). Therefore, the surface area (S_{MESO}) and the volume (V_{MESO}) of the mesoporous are listed in Table 1.

The synthesized catalysts with different fuel/nitrate ratios, such as NiMn1.25 and NiMn1.67, present type IV isotherms indicating mesoporous formation (Supplementary Information). It can also be observed that there is a region ($P/P \approx 0.85$) where the adsorbed volume increases sharply while the relative pressure varies little. The present hysteresis of the

isotherms is of type H1 with two branches of parallel isotherms, indicating complete mesoporous filling at a relative pressure of less than 1. This hysteresis also represents an adsorbent with a narrow distribution of relatively uniform pores [27].

The isotherm of the NiMn2.08 sample is of type V, characteristic of low adsorbent-adsorbate interaction. However, there is pore filling and hysteresis type H2. This hysteresis also characterizes mesoporous structure materials but is associated with a more complex structure with poorly defined pore size and shape distribution [28,29].

Table 1. The textural properties of the catalysts.

Catalyst	S_{MESO} (m ² /g)	V_{MESO} (cm ³ /g)
Mn0.5	1.28	0.0018
CoMn0.5	3.82	0.0142
CuMn0.5	5.68	0.0159
NiMn0.5	4.32	0.0143
NiMn1.25	0.94	0.0012
NiMn1.67	0.71	0.0008
NiMn2.08	0.02	0.0004

The data obtained from the adsorption/desorption analysis of N₂ allowed one to determine the surface areas of the samples. Still, given the limitations of the equipment, they were all classified as less than 10 m²/g.

The average pore diameter obtained by BJH is greater than 2 nm for all samples; the sample with a fuel rate of 0.5 has the largest pore distribution diameter (between 2 and 50 nm). These specifications are probably due to

the implementation of the proper fuel/nitrate ratio resulting in necessary and sufficient heat generation for combustion. Consequently, the proper gas volume was created during combustion. It is also possible to observe that the synthesized catalysts with a fuel/nitrate ratio of 1.25 and 1.67 have a very similar pore distribution diameter (between 2 nm and 40 nm), probably due to sufficient fuel availability during the synthesis process. But with a further increasing fuel/nitrate ratio to 2.08, larger crystals were formed due to increasing burning heat, reducing pore distribution diameter (between 2 nm and 30 nm).

Figure 2a presents the XRD results for the synthesized catalysts with a fuel/nitrate ratio equal to 0.5.

Through a comparative study between crystallographic reference chips of pure materials and the diffractograms obtained, it was possible to identify the diffraction lines characteristic of the structure Mn_3O_4 (*) with basic orthorhombic geometric structure in all samples, being more present in CoMn0.5. Furthermore, the CoMn0.5 sample also shows characteristics of $MnCo_2O_4$ (*), cubic and face-centered spinel.

The CuMn0.5 catalyst showed little similarity with the characteristic peaks of the less intense Mn_3O_4 structure, suggesting a loss of crystallinity. In addition, peaks related to the $CuMn_2O_4$ spinel structure (°), with cubic and face-centered structure, were also identified.

In the diffractogram of the NiMn0.5 sample, the characteristic $NiMn_2O_4$ spinel peaks (*) and cubic face-centered structure. The $NiMnO_3$ and NiO secondary phases, with diffraction peaks coinciding with those of the main phase, were possibly identified.

Figure 2b shows the X-ray diffraction (XRD) results for $NiMn_2O_4$ prepared by the combustion method with four different fuel/nitrate ratios. The formation of a spinel structure and some impurities of metal oxide (NiO and Mn_3O_4) were confirmed in all catalysts. In addition, the peaks in $2\theta = 23.1, 32.9, 55.1,$ and 65.9 were ascribed to the presence of Mn_3O_4 (PCPDFWIN 750765).

The diffraction lines corresponding to the Mn_3O_4 (♦) structure were observed in all samples. In addition, the peaks related to $NiMn_2O_4$ (●), $2\theta = 23.9, 34.1, 36.9, 41.7, 50.2,$ and 64.0 (PCPDFWIN 011110), cubic face-centered structure, and possibly $NiMnO_3$, $2\theta = 35.7, 39.3,$ and 49.1 (PCPDFWIN 120269), and NiO, $2\theta = 37.2, 43.2,$ and 62.9 (PCPDFWIN 780643); secondary phases were also identified. The intensity of these peaks generated in most $NiMn_2O_4$ phases was inversely proportional to the fuel/nitrate ratio; the increased fuel amount used decreased the catalyst crystallinity. The average crystallite size calculated based on the peak around 36° for the NiMn1.25, NiMn1.67, and NiMn2.08 catalysts were 21, 18.2, and 16.7 nm, respectively.

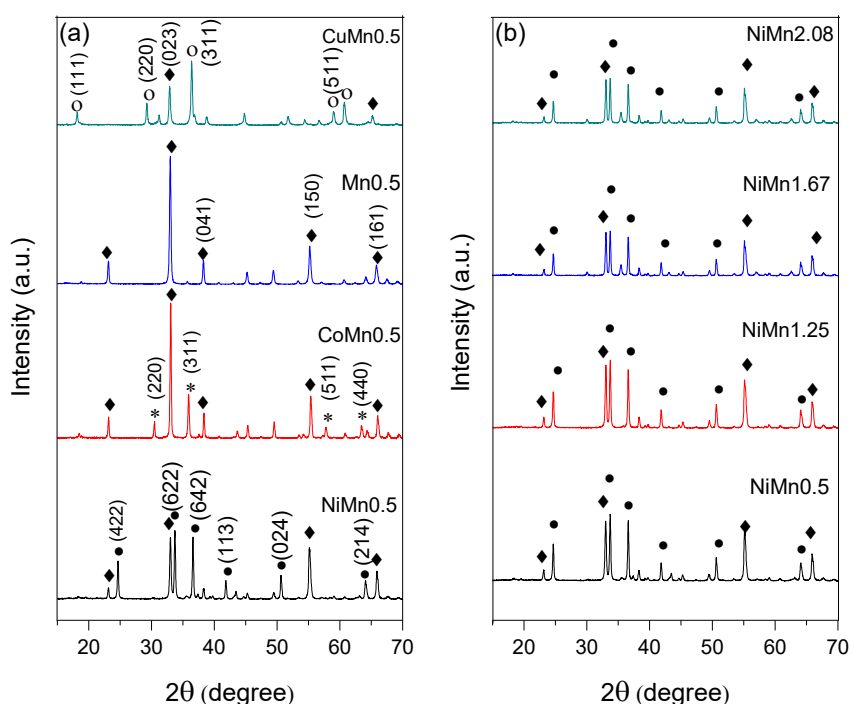


Figure 2. XRD patterns of (a) the catalysts with a fuel/nitrate ratio of 0.5 and (b) the $NiMn_2O_4$ catalysts with various fuel ratios.

FTIR analysis of the synthesized samples with a fuel/nitrate ratio of 0.5 was done in the 500 cm^{-1} – 4000 cm^{-1} wavelength range and shown in Figure 3a. The urea peak was not detected in any sample, generally indicated by a peak around 1700 cm^{-1} , due to the stretching of the double bond between C atoms. In this case, it was assumed that all the fuel was consumed in synthesizing the catalysts with a fuel/nitrate ratio of 0.5 [30,31]. The vibration peak of NO_3 groups appearing at 900 cm^{-1} , 1360 cm^{-1} , and 1560 cm^{-1} was also not detected, indicating a total consumption of nitrate compounds in the samples [32,33]. Strong peaks formed at 400 cm^{-1} – 700 cm^{-1} may be related to the formation of spinel structure [12;34].

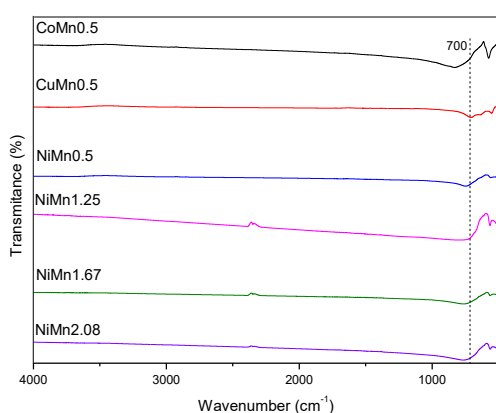


Figure 3. FTIR spectra of the catalysts with a fuel/nitrate ratio of 0.5 and the NiMn_2O_4 catalysts with various fuel/nitrate ratios.

The spinel structure in these samples was confirmed by the FTIR results (Figure 3b). According to the FTIR spectrum of the Ni catalysts with various fuel/nitrate ratios, the formation of the spinel structure in all mixed oxides can be confirmed. The bands formed below 1000 cm^{-1} are attributed to the metal-oxygen bonds (MOM), and in the range between 700 cm^{-1} and 400 cm^{-1} are characteristics of the AB_2O_4 structure [34]. The band near 700 cm^{-1} is attributed to the stretching vibrations of the Mn-O group coordinated in a tetrahedron. The vibrations corresponding to the stretching of the M-O group of octahedral coordination are observed around 517 cm^{-1} in all catalysts [12,34].

As the urea content in the synthesis of the Ni and Mn catalysts increases, the intensity of the vibrations, characteristic of the spinel structure (between 700 and 400 cm^{-1}), decreases. It can be explained by the dependence of the band intensity on the number of responsible bonds; that is, the oxides obtained with the lowest fuel/nitrate ratios show more bands attributed as spinel structures [35].

The H_2 -TPR experiments of synthesized catalysts with a fuel/nitrate ratio of 0.5 and the maximum

consumption temperatures are shown in Figure 4a. The Mn_3O_4 sample has two peaks, one starting at approximately $270\text{ }^\circ\text{C}$ and another between $400\text{ }^\circ\text{C}$ and $510\text{ }^\circ\text{C}$. According to the literature, the first one possibly refers to the reduction of Mn_2O_3 to Mn_3O_4 ($\text{Mn}^{3+} \rightarrow \text{Mn}^{3+}/\text{Mn}^{2+}$), and the second to the reduction of Mn_3O_4 to MnO ($\text{Mn}^{3+}/\text{Mn}^{2+} \rightarrow \text{Mn}^{2+}$) [36].

The sample reduced at lower temperatures is $\text{CoMn}_0.5$, with two reduction peaks. The first one is between $100\text{ }^\circ\text{C}$ and $250\text{ }^\circ\text{C}$, corresponding to the reduction of Co_3O_4 to Co^0 ($\text{Co}^{2+}/\text{Co}^{3+} \rightarrow \text{Co}^{2+} \rightarrow \text{Co}^0$), and the second one between $300\text{ }^\circ\text{C}$ and $450\text{ }^\circ\text{C}$, related to the reduction of CoMn_2O_4 ($\text{Co}^{2+} \rightarrow \text{Co}^0$) [12]. The $\text{CuMn}_0.5$ catalyst showed only a reduction peak between $200\text{ }^\circ\text{C}$ and $400\text{ }^\circ\text{C}$, related to the CuMn_2O_4 reduction ($\text{Cu}^{2+}/\text{Cu}^{1+} \rightarrow \text{Cu}^0$) [12].

The $\text{NiMn}_0.5$ catalyst showed the highest peaks near the peak range presented by the $\text{Mn}_0.5$ sample. For example, a peak between $250\text{ }^\circ\text{C}$ and $430\text{ }^\circ\text{C}$ refers to the reduction of NiMn_2O_4 and NiMnO_3 to NiO ($\text{Ni}^{3+} \rightarrow \text{Ni}^{2+}$), and another between $400\text{ }^\circ\text{C}$ and $600\text{ }^\circ\text{C}$ refers to the reduction of NiO to Ni^0 [23].

The H_2 -TPR experiments of NiMn_2O_4 synthesized with a different fuel/nitrate ratio and the maximum consumption temperatures are shown in Figure 4b. It can be observed that all NiMn samples showed similarities in the reduction profiles, with two characteristic peaks attributed to the decomposition of surface species NiMn_2O_4 and $\text{NiMnO}_3/\text{NiO} \rightarrow \text{MnO}/\text{Ni} \rightarrow \text{MnO}$. The $\text{NiMn}_1.25$ catalyst has the peak of the first major reduction, indicating the presence of more NiMn_2O_4 structures [23]. For this catalyst, a shift of the peaks towards the lowest temperature is observed. In the case of $\text{NiMn}_1.67$ and $\text{NiMn}_2.08$, a possible stronger interaction between manganese and nickel made the reduction more difficult. This effect can also be attributed to the increased partial water pressure in the catalyst pores as the particle diameter increases [22].

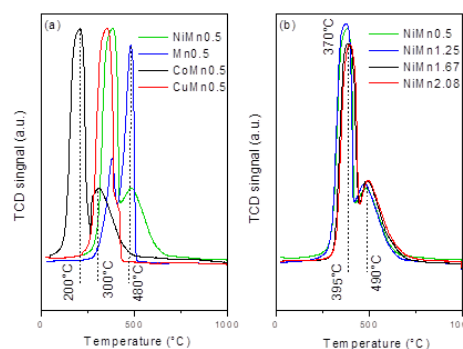


Figure 4. TPR curves for (a) the catalysts with a fuel/nitrate ratio of 0.5 and (b) the NiMn_2O_4 catalysts with various fuel/nitrate ratios.

Figure 5 shows the surface morphology of the samples with the same fuel/nitrate ratio (0.5). From the analysis of micrographs, we can observe the formation of aggregate particles in the form of grains, which tend to aggregate and grow due to the high temperatures reached during the synthesis. The addition of a second metal made these grains smaller.

Among the synthesized oxides with a fuel/nitrate ratio of 0.5, the CoMn0.5 was with the largest agglomerates, and the NiMn0.5 was with the smallest ones. The surfaces of the CoMn0.5 and Mn₃O₄ samples have voids in their structure, attributed to the evolution of larger quantities of gases during combustion [37].

The morphology and the particle size distribution of the Ni catalysts with various fuel/nitrate ratios (Supplementary Information) also indicated that the

influence of the urea content used is evidenced by observing that the structure of the obtained powders changes with increasing particles as the fuel/nitrate ratio is increased. It is also observed that the NiMn0.5 and NiMn1.25 samples have the most homogeneous surface, while the NiMn1.67 and NiMn2.08 samples have bigger and denser, occasionally dispersed clusters.

Figure 6 shows the catalytic performances of the catalysts in toluene combustion. The evaluation of the catalytic performance of all catalysts synthesized with a fuel/nitrate ratio equal to 0.5 showed conversion of 100% of toluene at 300 °C, while this conversion to Mn₃O₄ was only observed at 400 °C; this increase in catalytic activity is attributed to the addition of the second metal (Co, Cu, and Ni).

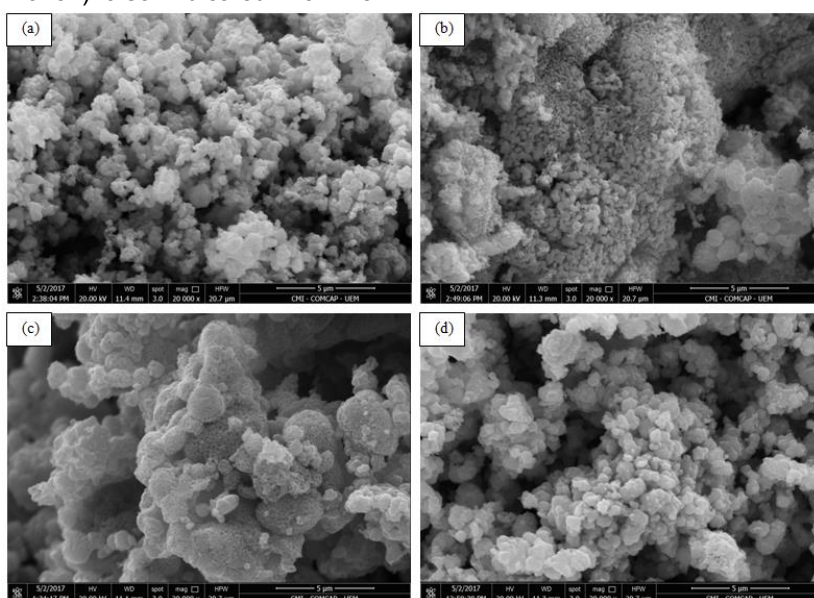


Figure 5. SEM images of the catalysts with a fuel/nitrate ratio of 0.5: (a) CoMn0.5, (b) CuMn0.5, (c) NiMn0.5, and (d) Mn₃O₄.

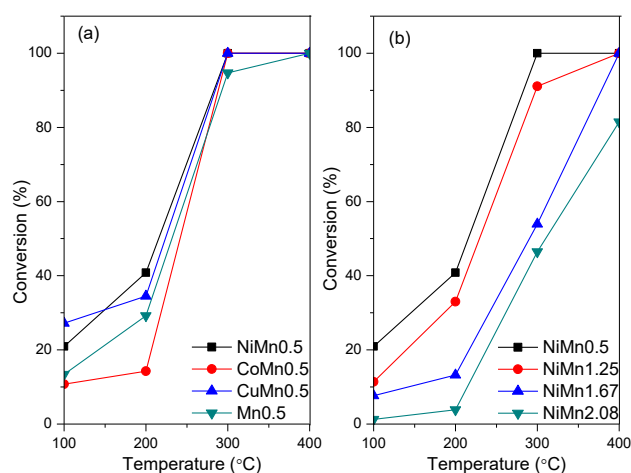


Figure 6. Curves for converting toluene over (a) the catalysts with a fuel/nitrate ratio of 0.5 and (b) the NiMn₂O₄ catalysts with various fuel ratios.

At the lowest temperature (100 °C), the catalyst CuMn0.5 showed the best conversion (27%), but NiMn0.5 was more active for toluene oxidation at higher temperatures. Although the synergistic interactions between Mn³⁺ and Ni²⁺ cations by oxygen bonds increase the catalytic activity at higher temperatures (>200 °C), the increase of the Ni²⁺ ions in the synthesized powders improves the reducibility of mixed oxides.

CoMn0.5 was less active at temperatures below 300 °C. This performance, combined with the XRD, FTIR, and TPR results, may indicate that CoMn0.5 presents a lower number of active Mn³⁺ and Co²⁺ sites than the other synthesized samples with a fuel/nitrate ratio of 0.5. Likewise, the highest activity of the NiMn oxide is attributed to the high content of Mn³⁺ and the synergistic effect between manganese in the spinel and Ni²⁺ cations.

NiMn0.5 showed the highest activity than others. It can be observed that the synergistic effect, together with the smaller synthesized NiMn catalysts, showed better catalytic activity (NiMn0.5 > NiMn1.25 > NiMn1.67 > NiMn2.08). Only the NiMn0.5 catalyst converted 100% toluene at 300 °C, while the maximum conversion obtained with NiMn2.08 was 81% at 400 °C.

Upon analyzing the results of the catalytic tests and the analysis of XRD, TPR, and FTIR, higher activities for the NiMn₂O₄ and CuMn₂O₄ catalysts can be observed compared to the CoMn₂O₄ catalyst. It can be attributed to the presence of active sites of Mn³⁺, Ni²⁺, and Cu²⁺. Likewise, the largest activity of NiMn₂O₄ is attributed to the highest content of Mn³⁺ and the synergistic effect of manganese on spinel and Ni²⁺ cations [38]. The catalytic performance of NiMn0.5 for toluene oxidation was compared with the literature that reported mixed oxides and noble metal catalysts, as shown in Table 2.

Table 2. Comparison of the catalytic performance between NiMn0.5 and other literature reported catalysts.

Catalyst	Catalyst mass (g)	Toluene concentration (ppmV)	T ₉₀ ^a (°C)	Ref.
Co ₂ AlO _x	0.4	530	284	[39]
5%Co/Al ₂ O ₃	0.2	1000	368	[40]
5%Cu/Al ₂ O ₃			363	
Cu ₄ FeO _x	0.1	800	294	[41]
Au/CeO ₂ -Al ₂ O ₃			280	
Ag/CeO ₂ -Al ₂ O ₃	0.05	1000	350	[42]
Pd/CeO ₂ -Al ₂ O ₃			220	
Pt/CeO ₂ -Al ₂ O ₃	0.1	1000	190	This work
NiMn0.5			282	

^aT₉₀ is the temperature at the time of conversion of 90% toluene.

VOC oxidation occurs according to a Mars-van Krevelen-type redox cycle, which involves the

adsorption of VOC and its subsequent oxidation by lattice oxygen and adsorbed oxygen atoms [43]. Since the mechanism involves the exchange of oxygen between the lattice and gas phase and oxidation of CO, oxygen mobility in the redox cycle and the surface acidity for breaking carbon-carbon bonds are important in hydrocarbon oxidation [44]. Although the correlation of acidity with the activity in oxidation reactions is still a subject of debate, it can be stated that the acid-base properties of mixed oxides may have a key role in controlling the kinetics of adsorption-desorption of the reactants and intermediate species [45]. In this case, metallic couples must be in different oxidation states for the reaction to occur. The more active sites, the greater the activity of the catalysts for the reaction. If more active Mn³⁺ and Ni²⁺ sites are present in the NiMn₂O₄ sample, this will justify its higher catalytic activity [12,38].

CONCLUSION

The spinel structure in all catalysts has gained prominence due to its high thermal resistance, selectivity, and electronic properties, which improve oxide reducibility.

The higher activity of NiMn oxide is attributed to the higher Mn³⁺ content and the synergistic effect of manganese on spinel and Ni²⁺ cations. This effect, added to the larger areas of the synthesized NiMn catalysts with lower fuel/nitrate ratios, gives the lower urea catalysts better catalytic activity. The synergistic effect added to the larger areas of smaller synthesized NiMn catalysts gave the lowest urea catalyst the best catalytic activity (NiMn0.5 > NiMn1.25 > NiMn1.67 > NiMn2.08). Furthermore, the catalyst toluene conversion temperature of 100% studied in the present work is compatible with commercially used Au-based catalysts, which are more expensive and susceptible to poisoning.

ACKNOWLEDGEMENTS

This study was financed in part by the Coordenação de Aperfeiçoamento de Pessoal de Nível Superior - Brasil (CAPES) - Finance Code 001. The authors also gratefully acknowledge Federal Fluminense University for complementary support.

REFERENCES

- [1] L. Pei, W. Yin, J. Wang, J. Chen, C. Fan, Q. Zhang, Mater. Res. 13 (2010) 339–343. <https://doi.org/10.1590/S1516-1439201000030001>.
- [2] C. He, J. Cheng, X. Zhang, M. Douthwaite, Z. Hao, Chem.

- Rev. 119 (2019) 4471–4568.
<https://doi.org/10.1021/acs.chemrev.8b00408>.
- [3] S. Hosseini, *Adv. Ceram. Sci. Eng.* 5 (2016) 1–10.
<https://doi.org/10.14355/acse.2016.05.001>.
- [4] R. Fang, J. Huang, X. Huang, X. Luo, Y. Sun, F. Dong, H. Huang, *Chemosphere* 289 (2022) 2–10.
<https://doi.org/10.1016/j.chemosphere.2021.133081>.
- [5] M. Castaño, R. Molina, S. Moreno, *Appl. Catal., A* 492 (2015) 48–59.
<https://doi.org/10.1016/j.apcata.2014.12.009>.
- [6] J. Li, W. Cui, P. Chen, X. Dong, Y. Chu, J. Sheng, Y. Zhang, Z. Wang, F. Dong, *Appl. Catal. B Environ.* 260 (2020) 118130–118136.
<https://doi.org/10.1016/j.apcatb.2019.118130>.
- [7] E. Genty, S. Siffert, R. Cousin, *Catal. Today* 333 (2019) 28–35. <https://doi.org/10.1016/j.cattod.2018.03.018>.
- [8] A. Kostyniuk, D. Bajec, B. Likozar, *J. of Ind. Eng. Chem.* 96 (2021) 130–143. <http://dx.doi.org/10.1016/j.proci.2006.07.052>.
- [9] C. Gennequin, S. Siffert, R. Cousin, A. Aboukais, *Top. Catal.* 52 (2009) 482–491. <https://doi.org/10.1007/s11244-009-9183-7>.
- [10] F. Agüero, B. Barbero, L. Gambaro, L. Cadús, *Appl. Catal., B* 91(2009) 108–112.
<http://dx.doi.org/10.1016/j.apcatb.2009.05.012>.
- [11] B. Silva, H. Figueiredo, V. Santos, M. Pereirab, J. Figueiredo, A. Lewandowskac, M. Bañares, I. Neves, T. Tavares, *J. Hazard. Mater.* 192 (2011) 545–553.
<https://doi.org/10.1016/j.jhazmat.2011.05.056>.
- [12] S. Hosseini, A. Niaei, D. Salari, S. Nabavi, *Ceram. Int.* 38 (2012) 1655–1661.
<https://doi.org/10.1016/j.ceramint.2011.09.057>.
- [13] B. Langford, *Atmos. Chem. Phys.* 10 (2010) 8391–8412.
<https://doi.org/10.5194/acp-10-8391-2010>.
- [14] C. Bozo, N. Guilhaume, E. Garbowski, M. Primet, *Catal. Today* 59 (2000) 33–45. [https://doi.org/10.1016/S0920-5861\(00\)00270-4](https://doi.org/10.1016/S0920-5861(00)00270-4).
- [15] N. Kumar, K. Jothimurugesan, G. Stanley, V. Schwartz, J. Spivey, *J. Phys. Chem. C* 115 (2011) 990–998.
<https://doi.org/10.1021/jp104878e>.
- [16] W. Wen, J. Wu, *RSC Adv.* 4 (2014) 58090–58100.
<https://doi.org/10.1039/C4RA10145F>.
- [17] J. Védrine, *Met. Oxides Heterog. Catal.*, Elsevier B.V. (2018) 551–569. <https://doi.org/10.1016/B978-0-12-811631-9.00009-0>.
- [18] S. Saqer, D. Kondarides, X. Verykios, *Appl. Catal., B* 103 (2011) 275–286.
<https://doi.org/10.1016/j.apcatb.2011.01.001>.
- [19] V. Radonjić, J. Krstić, D. Lončarević, N. Vukelić, D. Jovanović, *Chem. Ind. Chem. Eng. Q.* 25 (2019) 193–206. <https://doi.org/10.2298/CICEQ181001032R>.
- [20] S. Aruna, A. Mukasyan, *Solid State Mater. Sci.* 12 (2008) 44–50. <https://doi.org/10.1016/j.cossms.2008.12.002>.
- [21] J. Baneshi, M. Haghighi, N. Jodeiri, M. Abdollahifar, H. Ajamein, *Ceram. Int.* 40 (2014) 14177–14184.
<https://doi.org/10.1016/j.ceramint.2014.06.005>.
- [22] A. Varma, A. Mukasyan, A. Rogachev, K. Manukyan, *Chem. Rev.* 116 (2016) 14493–14586.
<https://doi.org/10.1021/acs.chemrev.6b00279>.
- [23] M. Ouaguenouni, A. Benadda, A. Kiennemann, A. Barama, *C. R. Chim.* 12 (2009) 740–747.
<https://doi.org/10.1016/j.crci.2008.12.002>.
- [24] D. Jeong, W. Jang, J. Shim, H. Roh, *Int. J. Hydrogen Energy* 41 (2016) 3870–3876.
<https://doi.org/10.1016/j.ijhydene.2016.01.024>.
- [25] S. Brunauer, P. Emmett, E. Teller, *J. Am. Chem. Soc.* 60 (1938) 309–319. <https://doi.org/10.1021/ja01269a023>.
- [26] L. Joyner, E. Barret, R. Skold, *J. Am. Chem. Soc.* 73 (1951) 3155–3158. <https://doi.org/10.1021/ja01151a046>.
- [27] T. Horikawa, D. Do, D. Nicholson, *Adv. Colloid Interface Sci.* 169 (2011) 40–58.
<https://doi.org/10.1016/j.cis.2011.08.003>.
- [28] G. Ertl, H. Knözinger, J. Weitkamp, *Handb. Heterog. Catal.* (2nd Ed.), Germany: VCH Verlagsgesellschaft mdH, (1997), 49–138.
<https://doi.org/10.1002/9783527619474>.
- [29] K. Sing, *Pure & Appl. Chem.* 57 (1985) 603–619.
<https://doi.org/10.1351/pac198557040603>.
- [30] L. Bach, B. Quynh, V. Thuan, C. Thang, K. Lim, J. *Nanosci. Nanotechnol.* 16 (2016) 8482–8485.
<https://doi.org/10.1166/jnn.2016.12511>.
- [31] A. Saberi, F. Golestani-Fard, H. Sarpoolaky, M. Willert-Porada, T. Gerdes, R. Simon, *J. Alloys Compd.* 462 (2008) 142–146.
<https://doi.org/10.1016/j.jallcom.2007.07.101>.
- [32] Y. Huang, Y. Tang, J. Wang, Q. Chen, *Mater. Chem. Phys.* 97 (2006) 394–397.
<https://doi.org/10.1016/j.matchemphys.2005.08.035>.
- [33] M. Taibi, S. Ammar, N. Jouini, F. Fievet, P. Molinie, M. Drillon, *J. Mater. Chem.* 12 (2002) 3238–3244.
<https://doi.org/10.1039/B204087E>.
- [34] A. Salker, S. Gurav, *J. Mater. Sci.* 35 (2000) 4713–4719.
<https://doi.org/10.1023/A:1004803123577>.
- [35] R. Zampiva, C. Junior, A. Alves, C. Bergmann, *FME Transactions.* 46 (2018) 157–164.
<https://doi.org/10.5937/fmet1802157Z>.
- [36] D. Aguilera, A. Perez, R. Molina, S. Moreno, *Appl. Catal., B* 104 (2011) 144–150.
<https://doi.org/10.1016/j.apcatb.2011.02.019>.
- [37] J. Toniolo, A. Takimi, C. Bergmann, *Mater. Res. Bull.* 45 (2010) 672–676.
<https://doi.org/10.1016/j.materresbull.2010.03.001>.
- [38] Q. Tang, C. Wu, R. Qiao, Y. Chen, Y. Yang, *Appl. Catal., A* 403 (2011) 136–141.
<https://doi.org/10.1016/j.apcata.2011.06.023>.
- [39] F. Kovanda, K. Jiráťová, *Applied Clay Science*, 53 (2011) 305–316. <https://doi.org/10.1016/j.clay.2010.12.030>.
- [40] S. Kim, Y. Park, J. Nah, *Powder Technology*, 266 (2014) 292–298. <https://doi.org/10.1016/j.powtec.2014.06.049>.
- [41] T. Xue, R. Li, W. Goa, Y. Goa, Q. Wang, A. Umar, J. *Nanosci. Nanotechnol.* 18 (2018) 3381–3386.
<https://doi.org/10.1166/jnn.2018.14627>.
- [42] H. Yang, J. Deng, Y. Liu, S. Xie, Z. Wu, H. Dai, *Journal of Molecular Catalysis A: Chemical* 414 (2016) 9–18.
<https://doi.org/10.1016/j.molcata.2015.12.010>.
- [43] L. Liu, Y. Song, Z. Fu, Q. Ye, S. Cheng, T. Kang, H. Dai, *Appl. Surf. Sci.* 396 (2017) 599–608.
<https://doi.org/10.1016/j.apsusc.2016.10.202>.
- [44] S. Carabineiro, X. Chen, M. Konsolakis, A. Psarras, P. Tavares, J. Órfão, M. Pereira, J. Figueiredo, *Catalysis Today* 244 (2015) 161–171.
<https://doi.org/10.1016/j.cattod.2014.06.018>.
- [45] G. Soylu, Z. Özçelik, I. Boz, *Chem. Eng. J.* 162 (2010) 380–387. <https://doi.org/10.1016/j.cej.2010.05.020>.

ALANNA SILVEIRA DE
MORAES¹
GABRIELA OLIVEIRA CASTRO
PONCINELLI¹
ARON SEIXAS TERRA
RODRIGUES¹
LAISE FAZOL DO COUTO¹
SILVIA LUCIANA FÁVARO²
RITA DE CÁSSIA COLMAN¹

¹Universidade Federal
Fluminense, Chemical
Engineering and Petroleum
Department, RJ, Brazil

²Universidade Estadual de
Maringá - Mechanical
Engineering Department,
Maringá, PR, Brazil

NAUČNI RAD

PROUČAVANJE KATALITIČKE OKSIDACIJE TOLUENA KORIŠĆENJEM KATALIZATORA MEŠOVITIH OKSIDA Cu-Mn, Co-Mn I Ni-Mn

Uspešna sinteza AMn_2O_4 ($A = Co, Cu, i Ni$) spinela sagorevanjem rastvora postignuta je za manje vremena nego drugim metodama. Za oksidaciju toluena korišćeni su svi katalizatori sa istim odnosom gorivo/nitrat i istražen je odnos između njihovih svojstava i aktivnosti. Među njima, nikel manganit je pokazao najveću aktivnost, a promenom odnosa gorivo/nitrat se tražilo da se dobije najprikladnija struktura za proučavanu reakciju. Fizičko-hemijska analiza je korišćena za definisanje karakteristika sintetizovanih katalizatora. Rezultati su pokazali uspešnu sintezu spinela i da u strukturi katalizatora postoje pikovi drugih materijala (pojedinačne oksidne faze). BET-BJH analize otkrile su mezoporozne strukture i, s obzirom na ograničenja opreme, sve su klasifikovane kao manje od $10 \text{ m}^2/\text{g}$. SEM slike dokazuju uticaj korišćenog sadržaja uree. Veličina čestica se povećava pri višim odnosima gorivo/nitrat. Uzorci NiMn1.67 i NiMn2.08 pokazali su veće i gušće, retko dispergovane klustere. Istovremeno, s obzirom na analizu reaktora i rezultate ispraživanja, utvrđeno je da sintetizovani katalizator sa odnosom gorivo/nitrat od 0,5 ima najbolje performanse u pogledu oksidacije toluena.

Ključne reči: sinteza sagorevanjem rastvora, odnos goriva i nitrata, manganit spineli, oksidacija toluena.